FOREARC UPLIFT IN NORTHERN CHILE: NEW PALEOALTIMETRIC

METHODS, CONSTRAINTS, AND NUMERICAL EXPERIMENTS ON THE

ROLE OF SUBDUCTION CHANNEL FLOW

A Dissertation

Presented to the Faculty of the Graduate School

of Cornell University

In Partial Fulfillment of the Requirements for the Degree of

Doctor of Philosophy

by

Nicolás Juan Cosentino

January 2017

FOREARC UPLIFT IN NORTHERN CHILE: NEW PALEOALTIMETRIC
METHODS, CONSTRAINTS, AND NUMERICAL EXPERIMENTS ON THE
ROLE OF SUBDUCTION CHANNEL FLOW

Nicolás Juan Cosentino, Ph. D.

Cornell University 2017

The lithosphere-scale geodynamic mechanisms that control forearc topography are still contentious. In northern Chile, this is in part due to a lack of paleoelevation constraints. In order to rectify this lack of data, this thesis carries out a series of studies.

First, a new paleoaltimetry proxy for the hyperarid Atacama Desert was developed, based on the elevation-dependent relationship of the $^{87}Sr/^{86}Sr$ ratio of Holocene surface accumulations of salts. Here, an important source of calcium sulfate comes from stratocumulus clouds that generate fog on the continent, transferring water droplets to the ground surface which, upon evaporation, precipitate calcium sulfate. The seawater ratio of $^{87}Sr/^{86}Sr$ (0.70917) is distinctly higher than that of weathered mean Andean rock (<0.70750). Sites below 1075 m.a.s.l. and above 225 m.a.s.l. display Holocene calcium sulfate $^{87}Sr/^{86}Sr$ of mean value 0.70807 ± 0.00004, while the ratio outside this altitudinal domain is 0.70746 ± 0.00010.

Based on these results for Holocene materials, Pliocene-Pleistocene paleoelevations of the forearc surface were inferred. We measured $^{87}Sr/^{86}Sr$ of dated ancient gypsic soils and applied appropriate corrections to the paleo-fog zone top and bottom. The results show that the magnitudes of paleo-elevation changes are small

compared to the elevation of the study area: more than 45% of the ~1000 m.a.s.l. average elevation of the Central Depression and more than 70% of the ~900 m.a.s.l. average elevation of the westernmost Coastal Cordillera were achieved by pre-early Pliocene regional scale tectonic processes.

Finally, the response of the forearc surface to 2D viscoelastic flow in a subduction channel was characterized numerically. 800-1100-m-thick subduction channels with viscosities of 5-10 $x10^{18}$ Pa s best fit the elevations of the Central Depression after steady-state topography is reached in less than 6 myr. The onset of hyperaridity at ~ 25 Ma starved the trench and subduction channel of sediments, raising shear stresses at the plate interface and uplifting the forearc. Short-lived phases of less aridity may have affected forearc topography transiently. The models predict that in order to accord with available Central Depression paleoelevation constraints, these phases translated to pulses of "weaker" subduction channels with viscosities between 2-7 $x10^{18}$ Pa s.

BIOGRAPHICAL SKETCH

Nicolás J. Cosentino was born the 7th of December of 1983 in San Isidro, Argentina, to Cecilia S. Soriano and Jorge H. J. Cosentino. Nico's childhood in the neighbourhood of Beccar could be accurately described as quite an average one amidst his friends in the "barrio": football in the streets, videogames at home, and school most of the day. Quite an ordinary bourgeois early life, perharps too ordinary to merit a bio sketch. Ever since his early years Nico showed a very competitive attitude towards school: he had to be the best and get the highest grades. Most of the times he did, sometimes he did not. Enter his second year of high school and things got really exciting. He started questioning himself whether it was any fun at all playing the game he had become so good at: know what Professor X want from you, deliver that, get the high grade. Classes all of a sudden became obvious for what they really were: long, boring speeches where knowledge was passed down encyclopedically, demanding the boys answers to questions they had never posed themselves. Biology Professor Andrés Lemoine changed all of that. All of a sudden Nico started to have classes with a guy that did not pretend to have all the answers, and that would get him excited enough about molecular and cell biology so as to start to ask himself his own questions. Prof. Lemoine was definitely one of the two main reasons why Nico became a scientist, although he did not know that at the moment. The other reason was his grandfather, a nuclear engineer who was in charge of the national nuclear agency. He always felt admiration for that secluded old man who talked about protons and neutrons during the traditional Sunday family lunches, amidst my brother and uncle who would shout out loud after each time Independiente scored a goal. Nico did not pay any attention to that. He wanted to know more about neutrons and protons. It so happens that many years after grandpa died, Nico discovered another facet of old Jorge that would

intrigue him even more, even to these very days: science policy, and the desire to have a country that could dream of having its own sovereign scientific project.

Nico entered college in the year 2002 searching for a major in Earth Sciences and a minor in Physics. He became interested in playing jigsaws with tectonic plates, and joined Dr. Francisco Vilas and Dr. Alejandro Tassone who were trying to elucidate how and when did western Anctartica split from South America. That took him to the White Continent in 2009, an experience he will not forget easily. Paleomagnetism was a lot of fun, and in the process he learned a lot about magnetic properties of rocks, demagnetization techniques, and how not to try to fit jigsaw pieces that clearly were not meant to fit.

In 2008, Nico met Prof. Sue Kay from Cornell University, who kindly invited him to join her to a trip to Puna in northwestern Argentina to dig holes in the ground. He was told that the hole-digging he would be in charge of would serve bigger purposes: seismic stations would be placed in them to record natural earthquakes. Hopefully that would help learn about the structure of the crust and lithosphere there. After a couple dusty trips to Puna on board of the Flying Machine, Nico dug up his way to Cornell University. There he met Prof. Terry Jordan and Prof. Jason Phipps Morgan, and this is how his adventures in the Atacama Desert started: it was time to ask how on Earth did the forearc uplift in northern Chile to its present elevation.

ACKNOWLEDGMENTS

First and foremost, I thank my advisor Teresa Jordan. Terry has been an amazing guide through my years as her PhD student. Almost all I have learned in my academic life so far I owe it to her. She has instilled in me that I should approach science critically, and not be driven by my desire to fit the data to my comfort zone. She knew exactly when to press me forward, and when to give me space. It has been a pleasure to share this project with you. I would also like to thank the members of my committee Jason Phipps Morgan and Natalie Mahowald for their collaboration in making my research better. In particular, I would like to thank Jason for trying to make me think out of the box, and for making me his guest at his house in my research travels to London. Your support has been critical to me coming this far.

I would also like to thank many people at EAS. Sue Kay introduced me to the wonders of the Puna during two geology field trips, and believed I was good enough to recommend me to EAS as a PhD student. Other faculty members Lou Derry, Bill White, Muawia Barazangi, Rick Allmendinger, Larry Brown and Chris Andronicos have enriched me academically. Special thanks go to graduate students Chao Shi, Naomi Kirk-Lawlor, Tianxiang Zheng, Gregg McElwee, John Mason and Kyle Torstle. Also, I could not have survived through these years without staff members Savannah Williams, Steve Gallow, Amy Colvin and Judy Starr.

Field discussions with colleagues Arturo Jensen, Felipe Andrés Lobos Roco, Marcelo García, Paulina Vázquez, Fernando Sepúlveda and Andrés Quezada were very important to my work. Also, special thanks go to Antonio Díaz Tapia for logistic services during field work in Atacama.

And of course, family and friends made all of this purposeful. Thanks Cecilia Soriano, Jorge Cosentino and Agustín Cosentino for supporting me in every single

instance of my life. I came all this way because of you. Thanks to my life-long friends Fernando Calviño, Mercedes Avila, Carla Descalzi, and Javier Cabanela for your friendship (thanks Mer for many a figure you perfected with your designing skills!). Thanks to the friends that life gave to me in Ithaca, and to all who made Ithaca the greatest place ever: Felipe Aron, Alejandra Escandón, Silvia Arrillaga, Eliana Monteverde, Enrique Mallada, Josefina Iannello, Julieta Gallego, Mauricio Bucca, Rosario Donoso, Diego Quiros, Marta del Campo, Francisco Arrillaga, Timothy Reber, Veronica Prush, Erin Meyer-Gutbrod, Josh Meyer-Gutbrod, Elaina Shope, José Muñoz, Francisco Delgado, Alida Pérez, Antonio Di Fenza, Viviana Stitz, Lucía Borlle, Robert Wijma, Matías Stangaferro, Marcelo Aguiar, Roberto Lozano, María Gabriela Brito, Diego Gómez, Tim Shenk, Dustin Madison, Megan Comins, David Jaume, Emmanuel and Kat Vissio, Marcela Villarreal, Nicky Greene and Dustin Walsh.

TABLE OF CONTENTS

CHAPTER 1

INTRODUCTION

The set of studies presented in this dissertation focuses on the forearc of the Central Andes in northern Chile. Along an east-west cross-section, the forearc is a wedge-shaped 250-300-km-wide area of crust whose upper surface forms both the seafloor and subaerial land extending from the trench located 85-160 km offshore to the west to the western reaches of the Western Cordillera volcanic arc to the east (Fig. 1-1). The forearc is located west of the Andean highlands, which in the Central Andes includes from west to east the Western Cordillera volcanic arc, the Altiplano-Puna plateau which is the highest plateau formed on a noncollisional convergent plate margin on the planet, and the highly deformed, horizontally shortened foreland ranges and basins of the Eastern Cordillera and Subandean belt (Fig. 1-1). That dynamic mixture of magmatic and tectonic activity within the Andean orogenic belt may provoke some broad deformation of the forearc that is expressed by a history of elevation change. Yet additional factors that determine the elevation and history of elevation change in the forearc are likely due to mechanisms that are specific to the forearc (Fig. 1-1). In northern Chile, where the relationship of the subducted plate to the forearc is erosive in nature, such proposed mechanisms include: (a) plate convergence-driven interseismic compression in the upper plate [González et al., 2003], (b) coseismic deformation during earthquakes originating at the plate interface below the Moho [Melnick, 2016], (c) subduction erosion of the westernmost submarine upper plate [von Huene and Ranero, 2003], (d) underplating of subducted sediments to the continental lithosphere [Clift and Hartley, 2007], and (e) hyperaridity-induced reduction in sediment delivery to the trench, which is associated

1

to a rise in shear stresses along the plate interface [Lamb and Davis, 2003]. Some of these mechanisms have been called upon to explain either coastal zone uplift (*b* and *d*), submarine forearc subsidence (*c*), coupled coastal zone uplift and submarine forearc subsidence (*a*), or full-scale Andean uplift (*e*). The last three mechanisms imply the existence of a subduction channel [e.g. Shreve and Cloos, 1986; Vannucchi et al., 2012] along at least part of the plate interface (Fig. 1-1).

      The surface elevation chronology of the Andean forearc is a crucial test of validity to models that intend to establish the relative contribution of these proposed geodynamic mechanisms to surface elevation change. East of the Central Andean forearc, a wide range of Cenozoic paleoaltimetry constraints have been extracted from marine facies distribution [e.g. Sempere et al., 1997], crustal shortening analysis [e.g. Isacks, 1988], oxygen isotope composition of paleo-precipitation water preserved in soil or lake carbonates [e.g. Leier et al., 2013] and hydrated volcanic glass [Canavan et al., 2014], leaf physiognomy [e.g. Gregory-Wodzicki, 2002] and clumped-isotope paleothermometry of paleosol carbonates [e.g. Ghosh et al., 2006]. However, many of these paleoelevation proxies are unavailable on the forearc, particularly on the inland forearc basin whose surface is the Central Depression, which is the main reason why there is a relative scarcity of Cenozoic surface paleoelevation constraints here when compared to the Altiplano Plateau and Eastern Cordillera to the east. Previous studies in the forearc used longitudinal river profiles [e.g. Hoke et al., 2007] and seismic interpretations of stratigraphic markers [Jordan et al., 2010] to look at post-11 Ma surface uplift of the easternmost Central Depression and Precordillera with respect to the western forearc. Only a few studies have provided absolute (i.e. with respect to sea level) Neogene surface paleoelevation constraints in northern Chile. On the westernmost inland forearc, dating of low-relief coastal surfaces has allowed inferences to be made of coastal zone uplift [Regard et al., 2010; Melnick, 2016].

Sparse outcrops of marine strata place constraints on minimum surface uplift in southwestern Peru since ~25 Ma [Thouret et al., 2007]. Finally, Evenstar et al. [2015] exploited the altitude control on the production rate of in situ cosmogenic nuclides to constrain the uplift history of the eastern margin of the forearc basin.

To employ the paleoaltimetric proxies that have been developed and applied elsewhere, the paleo-environment of the time span of interest needed to include vegetation, or to involve little evaporation of rainwater before its oxygen becomes mineralized, or to include volcanic deposits whose glass might have taken in hydrogen from meteoric water. The northern Chile western forearc fails to meet these criteria. Here, mean annual precipitation is lower than 40 mm yr^{-1} below 3000 m.a.s.l. [Houston and Hartley, 2003], and lower than 2 mm yr^{-1} in the driest parts of the desert [Hartley and Chong, 2002] and evaporation dominates over precipitation. The great majority of the landscape has no vascular plants. Volcanic deposits are restricted to the eastern part of the forearc. Consequently, a paleoaltimetric proxy was needed that took advantage of the unique natural environment of the Atacama Desert. We have developed a novel absolute paleoaltimetry method that is pertinent to the hyperarid Atacama Desert [Chapter 2; i.e. Cosentino et al., 2015] and apply it to the western forearc of the Central Andes [Chapter 3; i.e. Cosentino and Jordan, 2017], where constraints on Neogene surface paleoelevation are scarcest.

Hyperaridity has been the mean climate state in the study area since at least 11 Ma [Jordan et al., 2014], which has been conducive to extensive abandonment of alluvial depositional surfaces and their pedogenenetic transformation into widespread gypsic relict soils [e.g. Ericksen, 1981]. Soil formation in such arid areas is mainly by long term accumulation of atmospheric dust [e.g. Ewing et al., 2006], as is also believed to be the case in Martian surfaces [Amundson et al., 2008]. Atacama ancient soils are rich in calcium sulfates, which derive from dry and wet deposition of primary

marine aerosols' sea salts [e.g. Ericksen, 1981], among other sources. Fog events are widespread in northern Chile, taking place when South Pacific stratocumulus clouds advect inland by southwesterly winds, and topography is a first-order control on the vertical structure and inland spatial distribution of fog [Cereceda et al., 2002] (Fig. 1-2). Rech et al. (2003) had shown that the $^{87}Sr/^{86}Sr$ and $\delta^{34}S$ of gypsic soils of generally young age changed with distance from the Pacific shoreline and with increasing elevation. Consequently, this dissertation explores the potential to utilize the $^{87}Sr/^{86}Sr$ of Holocene calcium sulfates as a proxy for altitude and as a tool for paleoaltimetry.

Chapter 2 develops evidence that $^{87}Sr/^{86}Sr$ of Holocene calcium sulfates of marine origin is distinctively higher than $^{87}Sr/^{86}Sr$ of Holocene calcium sulfates of non-marine origin [Cosentino et al., 2015] (Fig. 1-2). The new paleoelevation proxy is based on the fact that the distribution of $^{87}Sr/^{86}Sr$ of Holocene salts in the landscape is bi-modal, with high values within the altitudinal bounds of the Holocene-averaged fog zone, and with low values outside [Cosentino et al., 2015] (Fig. 1-2). Chapter 3 applies the ability of $^{87}Sr/^{86}Sr$ to identify the altitude of formation of ancient gypsic soils as a paleoaltimetric method [Cosentino and Jordan, 2017]. By deriving appropriate corrections to the paleo-fog zone top and bottom based on the evolution of eustatic sea level, marine $^{87}Sr/^{86}Sr$ and sea surface temperatures, it has been possible to extract paleoaltitudinal constraints from dated ancient gypsic soils capping certain surfaces of the Coastal Cordillera and Central Depression [Chapter 3; i.e. Cosentino and Jordan, 2017]. We conclude from our paleoelevation results that more than 45% of the ~1000 m.a.s.l. average elevation of the Central Depression and that more than 70% of the ~900 m.a.s.l. average elevation of the westernmost Coastal Cordillera were accrued before the earliest Pliocene [Chapter 3; i.e. Cosentino and Jordan, 2017].

With better constraints on the history of elevation of the northern Chile forearc during the last 6 myr, the hypothetical mechanisms for tectonically driven elevation

change are then investigated (Chapter 4). East of the forearc, two competing hypotheses have been put forward to explain the Neogene surface elevation evolution of the adjacent Altiplano Plateau: (i) slow uplift since the early Miocene or before [e.g. Hartley et al., 2007; Barnes and Ehlers, 2009], and (ii) rapid ~2.5 km uplift between 11 and 6 Ma [e.g. Garzione et al., 2006; Ghosh et al., 2006]. Other studies that looked at the relief growth of the easternmost Central Depression and Precordillera in the eastern forearc are more consistent with the slow Altiplano Plateau uplift hypothesis [Victor et al., 2004; Farías et al., 2005; Hoke et al., 2007; Jordan et al., 2010]. It is important to note that our paleoaltimetric results constrain surface elevation change west of both the Altiplano Plateau and the eastern forearc, and thus are likely associated with geodynamic processes that build the main Andes only as far-field effects or not at all. Therefore, this research focuses on phenomena that are more intrinsic to the forearc geodynamics.

Two mechanisms have been proposed to explain coupled long-term subsidence of the marine forearc and uplift of the near-coastal nonmarine forearc: (a) buckle folding of the margin [González et al., 2003], and (b) coupled frontal subduction erosion near the trench and underplating of sediments below the coast [von Huene and Ranero, 2003; Clift and Hartley, 2007]. Whether either of these mechanisms can explain the long-term history of elevations within the Central Depression has not been investigated. Here, I hypothesize that viscous flow in a subduction channel is the main driver of uplift of the Central Depression, as well as a contributing factor to uplift of the Coastal Cordillera and subsidence of the marine forearc (Chapter 4). The mechanical role of the subduction channel is as a buffer to the stress applied by the subducting slab to the upper plate, since a fraction of this energy is consumed in straining the subduction channel fill. Lamb and Davis [2003] put forward an interesting hypothesis that climate and climate change might be responsible for

variations along strike in the height of the Andes. A derivative hypothesis is considered in this study, that possible variations in climate through time might be coupled to variations through time in the height of the Andes, with a narrow focus on the forearc. The hypothesis stems from the history of hyperaridity in the Atacama Desert: if the onset of hyperaridity in the region has triggered sediment starvation of the trench and a rise in shear stress at the plate interface, then surface elevation may have changed in response. Under this conceptual framework, we hypothesize that environmental conditions that are less arid (or hyperarid) promote conditions under which more sediment (or less sediment) is transported to the trench, and then advected downdip along the plate interface. When hyperarid conditions prevail, the subduction channel buffer effect is reduced and shear stresses on the base of the upper plate rise. We model 2D viscoelastic flow in a finite element mesh of the subduction channel with variable thickness and viscosity, and we follow the response of the submarine and subaerial free surfaces (Chapter 4). We find that 800-1100-m-thick subduction channels with viscosities of 5-10 x10^{18} Pa s best fit the elevations of the Central Depression after steady-state topography is reached in less than 6 myr. The onset of hyperaridity at ~ 25 Ma starved the trench and subduction channel of sediments, raising shear stresses at the plate interface and uplifting the forearc. Short-lived phases of less aridity may have affected forearc topography transiently. The models predict that in order to accord with available Central Depression paleoelevation constraints, these phases translated to pulses of "weaker" subduction channels with viscosities between 2-7 x10^{18} Pa s.

1.1 Figures

Figure 1-1. Cross section of the western flank of the Central Andes in northern Chile. Subsurface based on seismological interpretations of line ANCORP'96 and receiver function data [Victor et al., 2004]. Also shown are 1:1 topography and bathymetry, and 1:20 vertically exaggerated topography, which consist of average 19.53ºS, 20.00ºS, 20.50ºS, 21.00ºS and 21.44ºS DEM data (SRTM-90). The start (i.e. 0 km) of each of these five transects corresponds to the deepest seafloor location at their latitude.
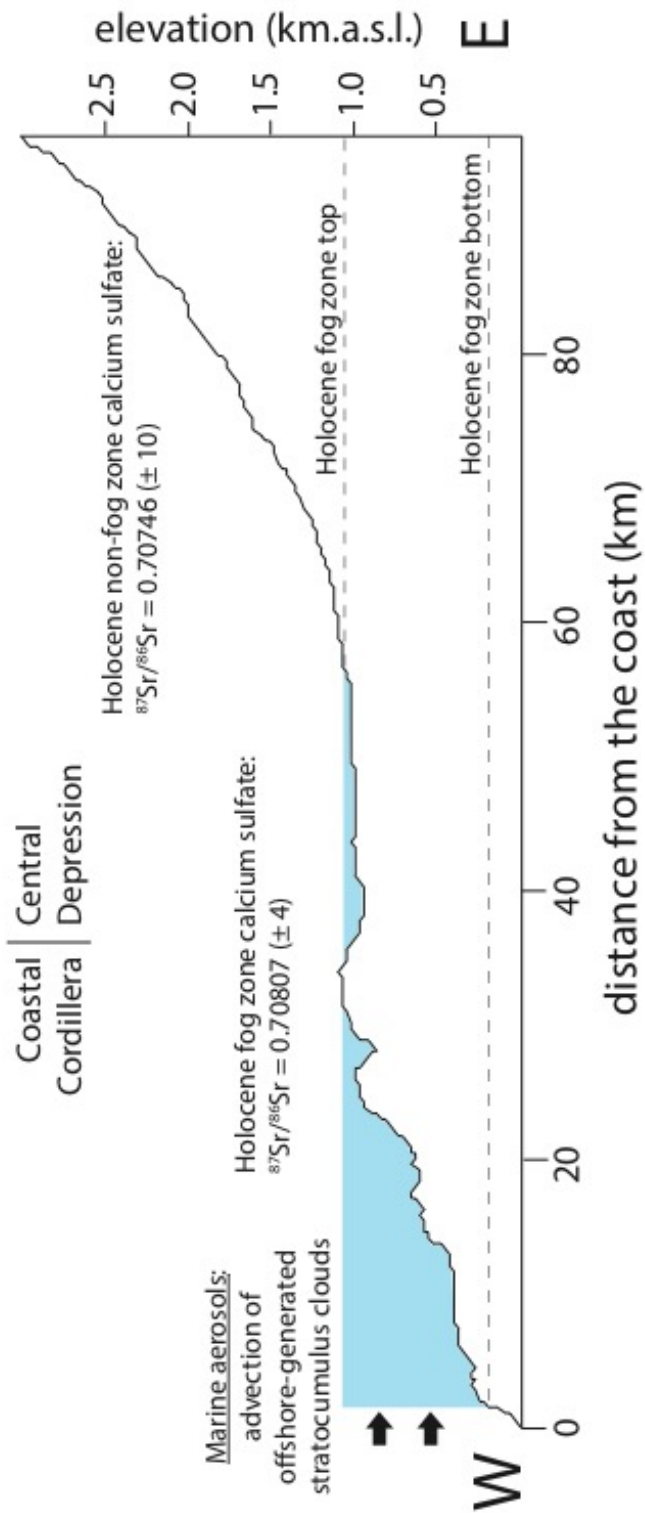
Figure 1-2. Cross section of the western inland forearc of the Central Andes in northern Chile. Topography consists of average 19.53ºS, 20.00ºS, 20.50ºS, 21.00ºS and 21.44ºS DEM data (SRTM-90).

8

REFERENCES

Amundson, R., Ewing, S., Dietrich, W., Sutter, B., Owen, J., Chadwick, O., Nishiizumi, K., Walvoord, M., and C. McKay (2008), On the in situ aqueous alteration of soils in Mars. *Geochimica Cosmochimica Acta* **72**, 3845-3864.

Barnes, J. B., and T. A. Ehlers (2009), End member models for Andean Plateau uplift. *Earth Sience Reviews* **97 (1-4)**, 105-132.

Canavan, R. R., B. Carrapa, M. T. Clementz, J. Quade, P. G. DeCelles, and L. M. Schoenbohm (2014), Early Cenozoic uplift of the Puna Plateau, Central Andes, based on stable isotope paleoaltimetry of hydrated volcanic glass. *Geology* **42 (5)**.

Cereceda P., P. Osses, H. Larrain, M. Farías, M. Lagos, R. Pinto, and R. S. Schemenauer (2002), Advective, orographic and radiation fog in the Tarapacá region, Chile, Atmospheric Research, 64, 261-271.

Clift, P. D., and A. J. Hartley (2007), Slow rates of subduction erosion and coastal underplating along the Andean margin of Chile and Peru. *Geology* **35**, 503-506.

Cosentino, N. J., and T. E. Jordan (2017), $^{87}Sr/^{86}Sr$ of calcium sulfate in ancient soils of hyperarid settings as a paleoaltitude proxy: Pliocene to Quaternary constraints for northern Chile (19.5-21.7°S). *Tectonics* **35**, doi:10.1002/2016TC004185.

Cosentino, N. J., T. E. Jordan, L. A. Derry, and J. P. Morgan (2015), $^{87}Sr/^{86}Sr$ in recent accumulations of calcium sulfate on landscapes of hyperarid settings: A bimodal altitudinal dependence for northern Chile (19.5°S–21.5°S). Geochem. Geophys. Geosyst. **16**, 4311-4328.

Ericksen, G. E. (1981), Geology and the origin of the Chilean nitrate deposits. *Geol. Soc. Amer. Spec. Paper*, 1188, 37.

Evenstar, L. A., F. M. Stuart, A. J. Hartley, and B. Tattich (2015), Slow Cenozoic

uplift of the western Andean Cordillera indicated by cosmogenic ^{3}He in alluvial

boulders from the Pacific Planation Surface. *Geophys. Res. Lett.* **42**, 8448-8455.

Ewing, S. A., B. Sutter, J. Owen, K. Nishiizumi, W. Sharp, S. S. Cliff, K. Perry, W.

Dietrich, C. P. McKay, and R. Amundson (2006), A threshold in soil formation at

Earth's arid-hyperarid transition. Geochimica et Cosmochimica Acta 70, 5293-

5322.

Farías, M., R. Charrier, D. Comte, J. Martinod, and G. Hérail (2005), Late Cenozoic

deformation and uplift of the western flank of the Altiplano: Evidence from the

depositional, tectonic, and geomorphologic evolution and shallow seismic activity

(northern Chile at 19°30'S). *Tectonics* **24**, TC4001.

Garzione, C. N., P. Molnar, J. C. Libarkin, and B. J. MacFadden (2006), Rapid late

Miocene rise of the Bolivian Altiplano: Evidence for removal of mantle

lithosphere. *Earth and Planetary Science Letters* **241 (3–4)**, 543–556.

Ghosh, P., C. N. Garzione, and J. M. Eiler (2006), Rapid uplift of the Altiplano

revealed through 13C-18O bonds in paleosol carbonates. Science 311, 511-515.

González, G., J. Cembrano, D. Carrizo, A. Macci, and H. Schneider (2003), The link

between forearc tectonics and Pliocene-Quaternary deformation of the Coastal

Cordillera, northern Chile. *Journal of South American Earth Sciences* **16**, 321-342.

Gregory-Wodzicki, K. M. (2002), A late Miocene subtropical-dry flora from the

northern Altiplano, Bolivia. *Palaeogeography, Palaeoclimatology, Palaeoecology*

180, 331-348.

Hartley, A., and G. Chong (2002), Late Pliocene age for the Atacama Desert:

implications for the desertification of western South America. *Geology* **30**, 43-46.

Hartley, A. J., T. Sempere, and G. Wörner (2007), A comment on "Rapid late

Miocene rise of the Bolivian Altiplano: Evidence for removal of mantle

lithosphere" by C. N. Garzione et al. [Earth and Planetary Science Letters 241 (2006) 543-556]. *Earth and Planetary Science Letters* **259 (3-4)**, 625-629.

Hoke, G. D., B. L. Isacks, T. E. Jordan, N. Blanco, A. J. Tomlinson, and J. Ramezani (2007), Geomorphic evidence for post-10 Ma uplift of the western flank of the central Andes, 18º30' – 22ºS. *Tectonics* **26**.

Houston, J. and A. J. Hartley (2003), The Central Andean west-slope rainshadow and its potential contribution to the origin of hyper-aridity in the Atacama Desert, Inter- national Journal of Climatology, 23, 1453–1464.

Isacks, B. L. (1988), Uplift of the central Andean plateau and bending of the Bolivian orocline. *Journal of Geophysical Research* **93**, 3211-3231.

Jordan, T. E., P. L. Nester, N. Blanco, G. D. Hoke, F. Dávila, and A. J. Tomlinson (2010), Uplift of the Altiplano-Puna plateau: A view from the west. *Tectonics* **29**, TC5007.

Jordan, T. E., N. E. Kirk-Lawlor, N. Blanco, J. A. Rech., and N. J. Cosentino (2014), Landscape modification in response to repeated onset of hyperarid paleoclimate states since 14 Ma, Atacama Desert, Chile. *Geological Society of America Bulletin* **126 (7-8)**, 1016-1046.

Lamb, S., and P. Davis (2003), Cenozoic climate change as a possible cause for the rise of the Andes. *Nature* **425**, 792-797.

Leier, A., N. McQuarrie, C. Garzione, and J. Eiler (2013), Stable isotope evidence for multiple pulses of rapid surface uplift in the Central Andes, Bolivia. *Earth and Planetary Science Letters* **371**, 49-58.

Melnick, D. (2016), Rise of the central Andean coast by earthquakes straddling the Moho. *Nature Geoscience* **9**, 401-407.

Rech, J. A., J. Quade, and W. S. Hart (2003), Isotopic evidence for the source of Ca and S in soil gypsum, anhydrite and calcite in the Atacama Desert, Chile. *Geochimica et Cosmochimica Acta* **67(4)**, 575-586.

Regard, V., M. Saillard, J. Martinod, L. Audin, S. Carretier, K. Pedoja, R. Riquelme, P. Paredes, and G. Hérail (2010), Renewed uplift of the Central Andes Forearc revealed by coastal evolution during the Quaternary. *Earth and Planetary Science Letters* **297**, issues 1-2, 199-210.

Sempere, T., R. F. Butler, D. R. Richards, L. G. Marshall, W. Sharp, and C. C. Swisher (1997), Stratigraphy and chronology of Upper Cretaceous-lower Paleogene strata in Bolivia and northwest Argentina. *Geological Society of America Bulletin* **109**, 709-727.

Shreve, R. L., and M. Cloos (1986), Dynamics of sediment subduction, melange formation, and prism accretion. Journal of Geophysical Research 91 (B10), 10229-10245.

Thouret, J. C., G. Wörner, Y. Gunnell, B. Singer, X. Zhang, and T. Souriot (2007), Geochronologic and stratigraphic constraints on canyon incision and Miocene uplift of the Central Andes in Peru. *Earth and Planetary Science Letters* **263**, 151-166.

Vannucchi, P., F. Sage, J. Phipps Morgan, F. Remitti, and J.-Y. Collot (2012), Toward a dynamic concept of the subduction channel at erosive convergent margins with implications for interplate material transfer. *Geochemistry Geophysics Geosystems* **13**, Q02003, doi:10.1029/2011GC003846.

Victor, P., O. Oncken, and J. Glodny (2004), Uplift of the western Altiplano plateau: Evidence from the Precordillera between 20 and 21° S (northern Chile). *Tectonics* **23**, no. 4.

von Huene, R., and C. R. Ranero (2003), Subduction erosion and basal friction along the sediment-starved convergent margin of Antofagasta, Chile. *Journal of Geophysical Research* **108**, 2079.

CHAPTER 2

^{87}SR/^{86}SR IN RECENT ACCUMULATIONS OF CALCIUM SULFATE ON

LANDSCAPES OF HYPERARID SETTINGS: A BIMODAL ALTITUDINAL

DEPENDENCE FOR NORTHERN CHILE (19.5-21.5°S)[*]

2.1 Abstract

An elevation-dependent relationship of the ^{87}Sr/^{86}Sr ratio of Holocene surface accumulations of sulfate salts is demonstrated for a continental margin hyperarid setting. In the Atacama Desert of northern Chile, gypsum and anhydrite of multiple origins exist widely on superficial materials that originated during the last 10,000 years. An important source of calcium sulfate is from offshore-generated stratocumulus clouds that are advected onto the continent, where they generate fog that transfers water droplets to the ground surface which, upon evaporation, leaves calcium sulfate crystals. Meteorological measurements of the cloud base and top altitudes average ~400 meters and ~1100 meters above sea level (m.a.s.l.), respectively. The seawater ratio of ^{87}Sr/^{86}Sr (0.70917) is distinctively higher than that reported for weathered mean Andean rock (less than 0.70750). Samples of 28 modern surface salt accumulations for locations between 200–2950 m.a.s.l. and between ~19°30' and ~21°30' S verify that ^{87}Sr/^{86}Sr varies as a function of site altitude. Sites below 1075 m.a.s.l. and above 225 m.a.s.l. display calcium sulfate ^{87}Sr/^{86}Sr of mean value 0.70807 ± 0.00004, while the ratio outside this altitudinal domain is 0.70746 ±

0.00010. Thus, the $^{87}Sr/^{86}Sr$ ratio of Holocene salt accumulations differentiates two altitudinal domains.

2.2 Introduction

Quantification of uplift of a continental surface relative to sea level is challenging [Rowley and Garzione, 2007], and is a topic of active research in the Andes [Gregory-Wodzicki, 2000; Schlunegger et al., 2006; Garzione et al., 2008; Farías et al., 2008; Jordan et al., 2010; Insel et al., 2012]. Quantified studies of topographic uplift of the continental part of a forearc system have been generally limited to documenting the temporal history of shoreline positions, such as along western South America [Saillard et al., 2009, 2011; Bourgois, 2010], in Costa Rica and Panama [Sak et al., 2008; Morell et al., 2011] and in southern Italy [Ferranti et al., 2007].

The South America – Nazca plate forearc system in northern Chile hosts the hyperarid Atacama Desert. In a hyperarid setting, traditional $\delta^{13}C$ and $\delta^{18}O$ stable isotope paleoaltimetric methods are generally not suitable due to the impacts of evaporation on isotopic ratios. Instead, saline surface materials are widely available. Rech et al. [2003] examined soil-forming processes in the Atacama Desert and revealed an apparent relationship between Sr isotopic composition of calcium sulfate soils and altitude, whose potential utility for paleoaltimetry has not been probed.

Before any paleoaltitude investigation would be justified, a much more extensive analysis is needed of the relationships between $^{87}Sr/^{86}Sr$ of surficial materials, the elevations of the sites in the the landscape at which those saline materials occur, and other factors that may influence the $^{87}Sr/^{86}Sr$ of these materials.

Here we document and analyze the relationship between the Sr isotope signature of geologically recent salt accumulations and their altitude of formation or deposition within the modern forearc system of the Atacama Desert, between 19.5–21.5°S.

2.3 Physical and chemical bases for the proxy

2.3.1 Controls on climate of the Atacama Desert

The Atacama Desert is among the driest places on Earth. Located in northern Chile and southernmost Peru between 17° and 27°S, it is bounded to the east by the western front ranges of the Andes Mountains (western Precordillera) and to the west by the Pacific Ocean (Fig. 2-1). In this region the potential evapotranspiration (PET) is between 1-2 mm d^{-1} [Mintz and Walker, 1992]. According to UNEP [1991], for this PET the climate is classified as "hyperarid" wherever the mean annual precipitation is below 20-40 mm yr^{-1}, a condition met widely below 3000 m.a.s.l. altitude [Houston and Hartley, 2003]. Three atmospheric and oceanic phenomena contribute to the arid conditions: the large-scale atmospheric subtropical subsidence due to the presence of the South Pacific High [e.g. Rodwell and Hoskins, 2001], the local atmospheric subsidence related to easterly flow over the Andes [e.g. Houston and Hartley, 2003], and the cold sea surface temperatures (SST) near the land, which are maintained by upwelling of cold Pacific deep waters near the coast [Takahashi and Battisti, 2007]. This upwelling is a response to offshore Ekman transport of oceanic water associated with equator-ward alongshore surface winds, which drive the eastern boundary current along the coasts of Chile and Peru. These conditions combine to greatly reduce precipitation over the area [Wang et al., 2004; Takahashi and Battisti, 2007]: southeast

Pacific westerly moist air masses are blocked by the high-pressure zone offshore; the Andes create a rain shadow; atmospheric convection is suppressed by the cold SST and the subtropical subsidence, producing a persistent temperature inversion. A result of these conditions is a persistent stratocumulus cloud deck produced offshore and advected inland by southwesterly winds, where they produce fog [Cereceda et al., 2002]. Due to the low altitude atmospheric temperature inversion, the stratocumuli clouds are trapped at low altitudes. It is this combination of an extreme lack of precipitation and the widespread presence of stratocumulus cloud decks and fog that make the Atacama such a unique desert.

2.3.2 Chilean forearc physiography and geology

The major landforms of the study area (Fig. 2-1) are a narrow, 0-3.5 km wide coastal platform, an angle-of-repose escarpment (Coastal Escarpment) facing the Pacific Ocean, across which altitudes rise to 500-1200 m.a.s.l., a 30–60 km wide mountain belt (Coastal Cordillera) with elevations generally <2000 m.a.s.l., and a 50–75 km wide valley inland of the coastal range (Central Depression) at ~1000–2500 m.a.s.l.. The study area is bounded to the east by the western foothills of the Andes (Western Andean Slope and Precordillera). Geologically, the Coastal Cordillera is composed predominantly of Jurassic volcanic rocks and Jurassic-Early Cretaceous dioritic to granodioritic plutonic rocks [SERNAGEOMIN, 2003; Vásquez and Sepúlveda, 2013]. A series of forearc sedimentary basins comprise the Central Depression, filled with strata of Oligocene to recent age [Hoke et al., 2007]. In the study area the basin is known as the Pampa del Tamarugal. In general the Coastal Cordillera and Central Depression constitute a gently rolling series of hills and a plain. Between 19.53°S and 21.43°S the Pampa del Tamarugal is internally drained, but to

the north a series of deep canyons traverse the forearc to reach the Pacific Ocean, of which the southernmost is the Tana valley. Farther south, the Loa River flows parallel to the Central Depression and then drains to the Pacific through a deep canyon (Fig. 2-1). Locally, salars (salt pans) cover broad areas near the boundary between the Pampa del Tamarugal and the Coastal Cordillera and occur within the Coastal Cordillera.

2.3.3 Superficial sulfate deposits of the Atacama Desert

Macroscopic superficial salt minerals occur widely in the Atacama, in landscape positions as variable as the Coastal Escarpment, the Coastal Cordillera mountains and valleys, the salt pans of both the Coastal Cordillera and the Central Depression, alluvial fans and piedmont slopes of the Central Depression, and within incised abandoned channels and valleys that traverse the Central Depression. Although many Atacama surfaces are formed of a composite of materials of uncertain antiquity [Jordan et al., 2014], we focus on parts of the landscape that formed since 10,000 years ago. That time range is selected because it is the time span since the last regionally documented extended period of wetter climate within the Central Depression [Nester et al., 2007; Quade et al., 2008; Gayó et al., 2012]. Within the Coastal Cordillera, Vargas and Ortlieb [1998] described a series of landscape stages corresponding to climate variations of the Late Pleistocene and Holocene. Marquet et al. [2012] argued that archeological remains in the Coastal Cordillera are suggestive of an additional time of wetter environmental conditions ~7000 to ~4200 years ago. Herrera and Custodio [2014] presented evidence of sufficient precipitation along the western flank of the Coastal Cordillera ~5000 to 3000 years ago to recharge local aquifers. Together, these results imply that for some landscape positions the maximum

age for persistent hyperarid conditions and for what we treat as "superficial" gypsum is less than ~4000 years.

The materials that host the superficial gypsum and anhydrite include gravel on the beds of fluvial channels, eolian sands, human relicts and, on the Coastal Escarpment only, bedrock and colluvium. A high rate of development of gypsum and anhydrite under modern conditions is clearly demonstrated by two reported cases of entombment in calcium sulfates of newspapers from the early 20th century within anthropogenically disturbed parts of the landscape surface, both in locations subjected often to fog [Searl and Rankin, 1993; D. Burr and R. Jacobsen, pers. comm. 2014].

Superficial gypsum and anhydrite crystals that are intermixed with fine-grained siliciclastics are commonly white to tan powdery materials, and occur in several morphologies [Jordan et al, 2014]. One variety forms crusts <2 mm thick on the base of pebbles, cobbles and boulders that lie on the landscape surface. These gypsum/anhydrite crusts are not laterally continuous, but rather are isolated under single clasts (Fig. 2-2a). Nevertheless, these crystals act as incipient cement among grains of sand that comprise the fine-grained matrix surrounding the bases of those cobbles, over a distance from the cobbles of <10 mm. Azúa-Bustos et al. [2011] showed that the efficiency of capture of water from fog increases with clast particle size, a fact consistent with the occurrence of gypsum/anhydrite crystals mostly under clasts with diameter > 5 cm.

A second variety of superficial sulfates is also powdery but occurs as a laterally continuous layer overlying alluvium or salt pan accumulations, where formation of the underlying material is attributed to the Holocene [e.g. Vásquez and Sepúlveda, 2013]. These superficial dust accumulations are commonly several centimeters to tens of centimeters thick (Fig. 2-2c). In some parts of the landscape

they form continuous horizons over many square kilometer areas, but they also are heavily pock-marked by many-meter-wide deflation pits.

A third type of superficial sulfate occurs as mm-scale laterally continuous calcium sulfate-rich soft crusts (Fig. 2-2d), which weakly cement siliciclastic detritus. These crusts lie at the surface-air interface and follow the relief of the underlying rock surface or soil surface. They can be found on surfaces of the Coastal Escarpment, the Coastal Cordillera and the Central Depression.

A fourth class of superficial sulfate occurs also along the Coastal Escarpment, where the near-surface geological materials are a mixture of bedrock, talus, eolian sand dunes and sheets, debris flows and colluvium [Orellana Cortés, 2010]. The sulfate cover material consists of a widespread crust typically 10-20 cm thick, tan to rusty brown in color, and composed mostly of salts with a low clast density (Fig. 2-2b). This thick gypsum/anhydrite crust is usually developed over a bedrock parent material. The steep coastal scarps are subjected to mega-earthquakes on a millennial time scale, and strong earthquakes on a century time scale [e.g. Comte and Pardo, 1991]. Moderate-sized earthquakes in modern times have provoked widespread downslope movement of both bedrock and surficial material [Marquardt et al., 2006], which would lead to disaggregation of a surficial gypsic crust. Thus we interpret the third and fourth categories of superficial sulfate crusts of the Coastal Escarpment to be less than 10,000 years in age.

The salts comprising these cobble-bottom powders, thick dust accumulations, and superficial crusts, are likely polygenetic. Some of the calcium sulfate crystals are recently formed (e.g. by recent wet deposition from marine aerosols or from evaporation of water at the edge of an ephemeral pond), but some of the crystals may have formed long ago and then later were physically translated by wind or water. For example, the modern winds may first erode the gypsum deposits of a Pleistocene-age

salar, and then transfer it to a new landscape location. Another likely example is that wind and water erode gypsum and anhydrite from Miocene and Pliocene gypsic relict soils and integrate those pre-Holocene materials into the Holocene superficial calcium sulfate population. Although it may be polygenetic, the gypsum and anhydrite dust is a part of the Holocene surface system.

For this study the target samples are calcium sulfates that are representative of salt accumulations that were created or re-worked within the Holocene climate regime. It may appear that it would be challenging to distinguish a polygenetic Holocene salt deposit from a more ancient gypsum-rich soil, since they are compositionally the same. However, the pre-Holocene soils have a moderately to well developed set of diagnostic pedogenic features (reviewed recently by Jordan et al., [2014]). If a soil cross section is well exposed, the pre-Holocene soils can be readily distinguished from the Holocene powders and crusts described above. Materials sampled initially from locations where differentiation between Holocene and pre-Holocene sulfates was ambiguous were excluded from the final analysis.

2.3.4 Incursions of marine-sourced fog into the continental interior

Fog is a characteristic phenomenon in the northern Chile forearc, especially during the austral winter season. By using GOES satellite images to study the spatial and temporal behavior of stratocumulus clouds and their associated fog events, Cereceda et al. [2002] and Farías et al. [2005] show that two main types of fog impact the continental surface and can be distinguished by their formation process. Advective fog events are the most widespread and result from advection of South Pacific stratocumulus clouds onto the continent by southwesterly winds. Orographic fogs are more localized phenomena and form on the first windward slope facing the sea when

incoming air masses ascend due to topographic obstacles and cool adiabatically, condensing water vapor [Cereceda et al., 2002].

Topography is a first-order control on the vertical structure and spatial distribution of advective fog, which contacts the Coastal Escarpment within an altitudinal band whose base and top are higher and lower than 400 and 1100 m.a.s.l., respectively [Cereceda et al., 2002]. Both in Peru and Chile, fog thickness on any given day is between 300 and 400 m [Espejo, 2001; Cereceda et al., 1997, 1998]. Farías et al. [2005] studied the spatial and temporal evolution of an advective event that took place August 4-5, 2001, also using GOES satellite images. This advective fog event lasted ~21 hours and had a latitudinal reach of approximately 200 km. Over a time span of a month (August 2001) the fog coverage was maximum on the Coastal Escarpment, intermediate along lowland topographic corridors connecting the escarpment with the Central Depression, and least within the Central Depression [Farías et al., 2005]. The most eastward penetration of the fog is strongly correlated with the 1100 m.a.s.l. contour line. Based on that body of work, for the following discussion the *observational fog zone* is treated as the continental area with altitudes between 400 and 1100 m.a.s.l..

2.3.5 Fog water chemistry

The water quality of coastal fog in northern Chile has been examined by Schemenauer and Cereceda [1992] for sites near 29°27'S and Sträter et al. [2010] at the Alto Patache fog oasis near 20º49'S. These studies reported chemistry of advective fog captured in traps, which are plastic strips through which persistent strong winds blow the water-laden air. The wind may also transport dust from nearby ground surfaces. Fog samples of events originating over the Pacific had pH value means of

4.99 (standard deviation 0.86) and 4.65 (standard deviation 0.89) [Schemenauer and Cerecedda, 1992] and between 2.9–3.5 [Sträter et al., 2010]. Both studies report high ionic concentrations coming from sea salt. Sträter et al. [2010] further concluded that anthropogenic activity was to blame for the high concentrations of heavy metals and contributed to the low pH, specifically mineral processing facilities, ship traffic, and power plants. For Holocene fog water predating anthropogenic contributions, the pH was likely more similar to the ~4.5-5 conditions reported by Schemenauer and Cereceda [1992].

2.3.6 ^{87}Sr/^{86}Sr in surficial salt deposits

Sr is known to substitute for Ca in many mineral phases, and since calcium sulfate minerals are abundant in our surficial deposits, Sr isotopes are ideal for investigating the primary source of Atacama salts and soils. Rech et al. [2003] pioneered this approach, documenting ^{87}Sr/^{86}Sr and δ^{34}S of soil gypsum/anhydrite along three ~E-W transects. They took advantage of the very different Sr isotope ratios of seawater and salts derived from the weathering of Andean rocks, or derived by weathering but recycled through salars, to identify the degree to which marine aerosol contributes to soil salt.

Modern seawater has a well-known ^{87}Sr/^{86}Sr value of 0.70916 ± 0.00002 [Farrell et al., 1995]. Rech et al. [2003] estimated the Sr isotopic ratio of typical Andean weathering products east of the Coastal Cordillera, using aquatic mollusks and tufa from streams in the western Andean slope, Andean lake salts, and salar salts both at the base of the Andes and in the Central Depression (see Rech et al. [2003] for in-depth descriptions of these samples and their isotopic ratios). Combining all these results, they defined a typical Andean weathering products' ^{87}Sr/^{86}Sr signature of

0.70749 ± 0.00046 [Rech et al., 2003]. Vivallo and Henriquez [1998] summarized $^{87}Sr/^{86}Sr$ for several major rock units in the Coastal Cordillera immediately south of our study area. They report that the widespread La Negra Formation and localized plutons have values limited to 0.703–0.704, whereas stratiform ore bodies are dominated by values of 0.704–0.706. These are whole-rock rather than weathered products' Sr isotopic values, so that their comparison with the Andean average calculated by Rech et al. [2003] is not straightforward.

On the one hand, unconsolidated gravel sediments in dry stream beds below which we collected many of the calcium sulfate samples derive from Andean erosional source areas. On the other hand, for most of the cases of calcium sulfate sampled in association with eolian sediments, the sand was transported from the coastal region. Therefore the parent rock for the stream bed gravel likely had a $^{87}Sr/^{86}Sr$ signature typical of the Andean average while eolian sand parents were more likely typical of the Coastal Cordillera.

Under the assumption that marine aerosols and Andean weathering products are the two main inputs of calcium sulfate salts to the Atacama Desert soils, an accumulation of salts that is a mixture of those inputs should develop an intermediate Sr isotopic ratio. The actual Sr isotopic value might be given by a linear mixing model between the two end-members:

$$x(^{87}Sr/^{86}Sr)_{marine} + (1-x)(^{87}Sr/^{86}Sr)_{Andes} = (^{87}Sr/^{86}Sr)_{salt} \qquad (1)$$

where x is the contribution of marine aerosols to the Sr ratio of the salts, $(^{87}Sr/^{86}Sr)_{marine} = 0.70916$ and $(^{87}Sr/^{86}Sr)_{Andes} = 0.70749$ [Rech et al., 2003]. However, as we have seen in the previous paragraph, Coastal Cordillera weathering products also constitute an input of calcium sulfate salts to Atacama Desert soils. An alternative

way to look at this problem, one that does not require the definition of an Andean rock Sr isotopic ratio average, will be presented in a later section.

Presented below are Sr isotopic composition and variations for a suite of samples of Holocene salts that accumulated across the Atacama Desert landscape over a wide area. Analysis of the $^{87}Sr/^{86}Sr$ data allows a comprehensive understanding of the effects of topography on the Sr isotopic ratio of Holocene surface salt accumulations at a regional scale. Knowledge of the dependence of Holocene Sr isotopic ratio on modern altitude is a foundation for interpretation of long time scale relationships of paleo-fog distribution to paleo-altitude across the continental surface.

2.4 Methods

2.4.1 Sampling of landscape salt accumulations

In order to study the spatial variability of the $^{87}Sr/^{86}Sr$ signature of modern accumulations of salts precipitated on or reworked across the study area landscape, superficial unconsolidated materials were sampled at 38 sites (one sample per site) across two east-trending transects and at other specific sites (Fig. 2-1). A published data set by Rech et al. [2003] is relevant for comparison, but their sampling strategy was notably different from the design of the current project, which limits the degree of inter-comparison. Their 12 soil samples from south of the area sampled in this study were taken along two E-W transects and at other specific sites (Fig. 2-1).

The four transects cover the Andean forearc from the western Coastal Escarpment to the Andean foothills in the east, crossing the Coastal Cordillera and

inner forearc basin. Altitudes range between ~200 and ~3000 m.a.s.l., although most sample sites (45 out of 50) are located between ~200 and ~1900 m.a.s.l..

The northernmost transect, Pisagua, is located at ~19.5°S (Fig. 2-1). This ~40 km long transect samples the plain between the deeply incised Tana and Tiliviche canyons, from the junction of those two canyons on the west (at ~950 m.a.s.l.) to an altitude of ~1850 m.a.s.l. on the east. The ~70 km long Huara transect is located at ~20°S (Fig. 2-1) and consists of samples of the Coastal Escarpment, Coastal Cordillera, forearc basin and Andean foothills, with elevations varying between ~200 and ~2750 m.a.s.l.. The Tocopilla transect at ~ 22°S of Rech et al.'s [2003] extends ~65 km from the Pacific Ocean into high-grade nitrate deposits in the Central Depression, covering elevations between ~900 and ~1450 m.a.s.l. (Fig. 2-1). The Antofagasta transect at ~24°S extends more than 200 km from the Coastal Escarpment to Cordillera Domeyko, with elevations between ~650 and ~3000 m.a.s.l. (Fig. 2-1). In addition to these transects, 21 samples test other individual locations of interest, many of them at an elevation near 1100–1200 m.a.s.l. (Fig. 2-1).

For collection of the superficial gypsum and anhydrite at the 38 new sites, the primary sample selection challenge was to distinguish between Holocene gypsum/anhydrite superficial materials and relict gypsic soils, and to avoid samples that might be contaminated by pre-Holocene gypsic soil. Given that relict gypsic soils are widespread on old landscape surfaces in the study area [Jordan et al., 2014], our strategy was to target the following landscape positions: 1) channels incised below the ancient landscape surfaces in which there were at least 10 cm thickness of post-incision fluvial deposits overlying any relict soils, 2) wind-deflated pits that are eroded into the regional relict landscape surface, specifically seeking a part of a deflation pit with a layer of eolian sand overlying the pre-deflation soils or sediments and underlying the potential gypsum/anhydrite sample, and 3) the angle-of-repose slope of

the Coastal Escarpment. In those small-scale landscape settings, we sought accumulations of gypsum or anhydrite. For the thin soft crust of the Coastal Escarpment or the tens-of-centimeter thick dust accumulations of some parts of the Coastal Cordillera and Central Depression, we collected samples from the most superficial 5 cm. For the incised fluvial channels and surfaces covered by eolian sand sheets, we turned over tens of cobbles and boulders to locate individual clasts under which gypsum crystals formed a soft crust. The samples were commonly collected with a spoon or a steel knife blade and placed in plastic sample bags. The occurrence category at each sample is reported in Table A1 (Appendix A). Expertise in recognition of pre-Holocene gypsic soils improved over the three years of sampling, with the outcome that more of the 2011 samples are categorized as of low probability of being restricted to Holocene materials than for 2012 and 2013 sample years. Based on the sample and geomorphic context characteristics, we classified each sample by the probability that it consists of a recently (i.e. Holocene) deposited intermixture of salts and fine-grained siliciclastics (Table A1 in Appendix A).

The Rech et al. [2003] samples from the southern two transects were not collected specifically to capture the Holocene conditions. Those samples were obtained at depths of 20–30 cm below the top of the local soil, often from the upper part of a moderately cemented horizon. These samples represent longer time-averaged conditions. Along the Rech et al. [2003] southernmost profile, Ewing et al. [2008] sampled a vertical sequence inclusive of depths as shallow as 1 cm and 2.5 cm below the top of the local soil. Plausibly those shallowest horizons sample Holocene materials of a type similar to our third category of surface materials (Fig. 2-2c). However, Ewing et al.'s [2006] criteria for selection of that site, i.e., that the landform position was morphologically higher than local stream beds and thus older than the

modern depositional system, places it by our criteria in a category somewhat older than the materials on which we focus in this paper.

2.4.2 Fog sampling

Three samples of fog water were collected at 'fog-catcher' nets at Alto Patache (70.15º W, 20.83º S, see site TJ-103, 104 and 106 on Fig. 2-1). The nets consist of plastic webbing mounted vertically on a wooden frame, through which the wind drives the fog. Water droplets drain off the web. Particulate contaminants, apparently of deteriorated plastic net, were found in two of the samples that were collected from a PVC tube at the base of the net (TJ-104 and TJ-106). Fog sample TJ-103 was obtained on 3 September 2012, at 16.08-16.10 hs (GMT -4).

2.4.3 Chemistry, mineralogy and Sr isotopic compositions

For each surface salt sample, the coarser-than-0.5 cm siliciclastic fraction was separated and the rest of the sample was physically homogenized and then soaked in water to dissolve the soluble salts. The ratio of water to sample necessary for full dissolution of the soluble fraction of the sample was determined by experimentation with different sample aliquots and water volumes. Those experiments led us to adopt a standard ratio of approximately 50 mg of the homogenized sample mixed with 35 ml of ultra-pure water (resistivity of 18.2 MΩ cm), which was placed in an ultrasonic warm (~50ºC) bath during 8 hours, and finally centrifuged at 3,000 rpm for 15 minutes.

The F^-, NO_3^-, Cl^- and SO_4^{2-} concentrations of the resulting solution were measured using ion chromatography (Dionex ICS 2000, Cornell University), while the

Ca^{2+}, Mg^{2+}, K^+, Na^+, Sr and Si concentrations were determined using ICP-OES (Amteck SpectroBlue, Cornell University). Sr in some samples was measured by ICP mass spectrometry (Thermo-Finnigan Element2, Cornell University). In all cases measurement uncertainty is better than 5%.

In the case of the fog samples, cation concentrations were obtained in the same manner, except for soluble Si. The concentration of Si was determined based on the absorbance of a silicomolybdate complex solution [Mortlock & Froelich, 1989], within 2% uncertainty.

Identification and quantification of mineral phases of selected bulk solid samples of surface salt accumulations were carried out using a Scintag Theta-Theta X-Ray Diffractometer (XRD, Cornell University). Phase quantification based on XRD analysis has many caveats [e. g., Moore and Reynolds, 1997; Kahle et al., 2002]. Thus, we present our phase quantification results as first-order estimates that make relative comparisons, rather than absolute determinations, possible.

Finally, all solutions (including fog sample TJ-103) were passed through cation exchange columns, using *Eichrom Sr* as the ion-exchange resin, and using the methodology proposed by Horwitz et al. [1992]. For most samples, $^{87}Sr/^{86}Sr$ was measured with thermal ionization mass spectrometry (VG Sector 54, Cornell University). NBS-987 Sr standards run in association with samples averaged 0.71024 ± 0.00003 (2σ, n = 32). For samples NC13-138, 145, 152, 153 and 156, and for fog sample TJ-103, $^{87}Sr/^{86}Sr$ was measured with a Neptune Multicollector ICP-MS (Rutgers University). In this case, NBS-987 Sr standards run in association with samples averaged 0.710282 ± 0.000012 (2σ, n = 18). In both cases, the water:sample ratio used (200 mg of sample and 10 ml water volume) during the soluble salt extraction process was different from the one discussed above for the case of the determination of the chemistry of the samples. Apart from this difference, the process

was the same. Sr isotopic measurements were performed for a subset of eight samples using both extraction water:sample ratios, and in all cases the differences in $^{87}Sr/^{86}Sr$ lay in the fifth decimal, or within 2σ of each other. Thus, even though dissolution of gypsum in the 20 ml : 200 mg experiments may have been incomplete, the results demonstrate that there was not an impact on $^{87}Sr/^{86}Sr$ which would be a concern if various calcium sulfate components bore differing $^{87}Sr/^{86}Sr$.

2.5 Results and discussion

2.5.1 Chemistry of the soluble fraction of the samples and Sr isotopic compositions

The chemical composition of the soluble fraction of the landscape surface samples is dominated by Ca^{2+} and SO_4^{2-} (averages of 1.56 and 1.37 mmol/g of total sample, respectively, Table S1). Na^+ and Cl^- occur in intermediate quantities (0.26 and 0.22 mmol/g respectively, Table S1), while NO_3^-, K^+ and Mg^{2+} are found in small quantities (0.023, 0.019 and 0.020 mmol/g, respectively). Sr and F^- occur in trace amounts (0.002 and 0.003 mmol/g, respectively, Table S1). Finally, the average content of soluble Si is 0.068 mmol/g (Table A1 in Appendix A).

There is a general equimolar trend in Ca^{2+} vs. SO_4^{2-} (Fig. 3a), and a less clear one for Na^+ vs. Cl^- (Fig. 2-3b). Samples in subgroups of high, low and intermediate confidence that they represent Holocene deposition (Table A1 in Appendix A) all yield equal molar ratios. The chemistry and molar trends are consistent with calcium sulfates being the main soluble mineralogical phases.

Sr isotope ratios range between 0.70682 and 0.70850, with one outlier at 0.71195 (NC11-33, Table A1 in Appendix A, Fig. 2-3). There is no apparent

correlation between $^{87}Sr/^{86}Sr$ and the concentrations of soluble Sr (Fig. 2-3c), Si (Fig. 2-3d) and Ca (Fig. 2-3e). No specific trends are observed for any subgroup of samples based on the confidence of recent deposition (Fig. 2-3c, 2-3d and 2-3e). The only outlier, sample NC11-33, has one of the lowest Ca/Si ratios (Fig. 2-3f), which suggests that a component of silicate-derived Sr may be important.

2.5.2 Mineralogy

Four samples from the Huara transect and one from the Pisagua transect were selected for XRD analysis of mineralogy (Table 2-1; see Fig. 2-4 for site locations).

For the Huara transect, bulk mineralogy is dominated by gypsum for the two sites below 800 m.a.s.l., with 70% gypsum by mass. Samples collected further from the coast and above 1200 m.a.s.l. (NC11-8 and NC11-12) show a dominance of anhydrite over gypsum. The sample collected at ~1210 m.a.s.l. is mostly composed of anhydrite, while the sample collected at ~2770 m.a.s.l. has a dominance of quartz (80%). The Pisagua transect sample NC12-74, at ~1180 m.a.s.l., contains ~30% gypsum, with the rest of the mass composed of silicates (quartz and plagioclase).

The results show that gypsum dominates at lower elevations while anhydrite is favored at higher altitudes. Furthermore, the highest salt fractions are found at low elevations. This elevation dependence of the salt composition and its fraction of the total incipient soil mass suggests a strong marine aerosol control. We infer that these trends occur because a) gypsum is the favored calcium sulfate phase during wet and dry marine aerosol precipitation, and b) an enhanced availability of marine aerosols at low elevation produces a high salt-to-siliciclastics ratio.

No halite phase was identified among the major minerals by XRD. Nonetheless, Na and Cl could be present as subordinate halite, or as part of other

mineral phases. Na and Cl may be also present as adsorbed ions on the exchange complexes of silicate clays.

2.5.3 ^{87}Sr/^{86}Sr variations inland from the coast

2.5.3.1 ^{87}Sr/^{86}Sr of fog water at the Coastal Escarpment

The ^{87}Sr/^{86}Sr value obtained (sample TJ12-103, 0.70875 ± 0.00001, see Table A1 in Appendix A) is lower than seawater ^{87}Sr/^{86}Sr (0.70916; Farrell et al., 1995). However, the ratio is higher than for any other material sampled by Rech et al. [2003] or for this study (except the outlier, sample NC11-33).

2.5.3.2. Huara transect

The Huara transect crosses the Coastal Escarpment, Coastal Cordillera, and Central Depression in a zone lacking cross-forearc fluvial drainage, where the escarpment relief is approximately 750 m.. This transect consists of 12 sampling sites (Figure 2-4b), nine of which were classified as unambiguously Holocene, two as likely Holocene, and one as sufficiently ambiguous that we omit it from further consideration (Table A1 in Appendix A).

Considering only samples that are assumed modern with intermediate to high certainty (yellow and blue samples, Fig. 2-4b), the highest ^{87}Sr/^{86}Sr values along the Huara transect are located inside the observational fog zone, peaking at the site ~1 km from the coast on the Coastal Escarpment (NC13-152, 399 m.a.s.l.), where the mixing model indicates ~32% marine contribution (Andean end-member: 0.70749). ^{87}Sr/^{86}Sr values along the Coastal Escarpment decrease towards the shoreline, reaching values

indistinguishable from the Andean average at ~200 m.a.s.l.. To the east, the ^{87}Sr/^{86}Sr of modern salts decrease until reaching values similar to or lower than the Andean average at distances of ~40 km or more from the coast.

2.5.3.3 Pisagua transect

The Pisagua transect was designed to explore the fog-related ^{87}Sr/^{86}Sr signal where there is a breach in the Coastal Escarpment and Coastal Cordillera through which fog penetrates farther to the east than is the case over most of the forearc. The Central Depression at this latitude is incised by two fluvial valleys (Quebradas Tana and Tiliviche, Fig. 2-4a) that parallel to each other before merging, at the eastern limit of the Coastal Cordillera, into a single valley. The single valley drains ~15 km distance to the Pacific Ocean and is deeply incised (~700 m) through the Coastal Cordillera. Along the Tana valley, the vertical incision through the Central Depression decreases to ~100 m at intermediate positions of the Central Depression, and increases again to ~300 m at the easternmost sites. The inter-canyon plain is less incised along the Tiliviche valley, reaching ~40 m at intermediate transect sites, and ~170 m at the easternmost sites. All 7 sites along this transect lie on the plain between the two valleys (Fig. 2-4a).

Few of the samples in this transect meet the criteria to be assigned a high probability that they include only Holocene-age materials. In retrospect this is a logical consequence of the two incised canyons bounding the plain; those canyons divert surface runoff from the adjacent Andean foothill ranges away from the inter-canyon plain. The result is uncharacteristically little fluvial erosion of the forearc basin, and thus there are very few diagnostic Late Pleistocene or Holocene fluvial deposits with which to distinguish Holocene gypsum and anhydrite from pre-Holocene

soil. Both of the samples that are categorized as having a high likelihood of a Holocene age (NC11-74 and NC11-19) are located at elevations that are today above the observational fog zone (1183 m.a.s.l. and 1870 m.a.s.l., respectively). Their Sr ratios (0.70724 and 0. 70755, respectively) are consistent with little to no marine-aerosol contribution.

The samples located at the western tip of the Tana/Tiliviche interfluve (~18 and ~25 km from the coast, westernmost two sites; NC11-21 and 22) were sampled from the best available superficial materials, in eolian deflation pits. However, they are in close proximity (1–3 cm) to bedded Pliocene evaporites, a salt-pan that was active at 3.5 Ma [Kirk-Lawlor et al., 2013] in locations frequently wet by fog. Therefore, we judge that there is a high likelihood for contamination. Because those samples show the lowest $^{87}Sr/^{86}Sr$ values of the transect, the $^{87}Sr/^{86}Sr$ values increase with distance inland, an unexpected trend. This deviation is interpreted to result from the remobilization of salar dust towards sampling sites NC11-21 and 22, thereby acquiring an isotopically light gypsum component [Rech et al., 2003], which would obscure a fog signal even if marine aerosols do indeed contribute to modern salts in that area.

2.5.3.4 Antofagasta and Tocopilla transects

These two transects are located between 22°–24°S and were previously reported by Rech et al. [2003]. Unlike the transects reported above, Rech et al. [2003] did not attempt to sample only Holocene materials. Amundson et al. [2012] provided evidence that along the Antofagasta transect the oldest superficial materials that one would encounter are younger than 2 Ma, hence this set of samples should be considered to represent the Quaternary conditions but not strictly the Holocene. With

that limitation, these $^{87}Sr/^{86}Sr$ values were the original justification for hypothesizing an altitudinal dependence.

The Antofagasta transect has soil gypsum/anhydrite $^{87}Sr/^{86}Sr$ values that systematically decrease with distance from the Pacific Ocean (Fig. 2-4d). Using the two end-member linear mixing model (1), the westernmost sample shows a marine component of ~80% (Andean end-member: 0.70749), while samples more than 50 km from the coast become indistinguishable from the Andean average, as defined by Rech et al. [2003]. Ewing et al. [2008] sampled a vertical profile of an ancient soil located ~30 km to the southwest of the Antofagasta transect at 24.10°S, 70.02°W, at an altitude of 1020 m.a.s.l.. This ancient soil is 2.3 m-thick and is younger than 2.1 Ma [Ewing et al., 2008]. The $^{87}Sr/^{86}Sr$ values decrease from 0.70743 at 1 cm depth to 0.70709 at 134 cm depth [Ewing et al., 2008]. AT258 and AT264 are Antofagasta transect samples located at 845 and 1305 m.a.s.l., respectively (Table A1 in Appendix A). They were sampled at depths of 20-30 cm and have $^{87}Sr/^{86}Sr$ values of 0.70761 and 0.70736, respectively (Table A1 in Appendix A). At similar depths below the ancient soil top, the Ewing et al. [2008] profile has values of 0.70740 and 0.70733. The shallowest sample at this profile, which is the one that is arguably more likely to have the greatest Holocene contribution, has a $^{87}Sr/^{86}Sr$ value of 0.70743, very close to the Andean average by Rech et al. [2003].

The Tocopilla transect (Fig. 2-4c) shows that the sample with highest $^{87}Sr/^{86}Sr$ is the one within the observational fog zone, at ~10 km from the coast. The rest of the samples were all collected outside of the observational fog zone and have $^{87}Sr/^{86}Sr$ values below the Andean average (Fig.2- 4c).

2.5.4 $^{87}Sr/^{86}Sr$ altimetry

A graph of the altitude of salt accumulation and the Sr isotope signature that is inclusive of all samples (n = 50; Fig. 2-5a) displays a general trend of high ratios at low elevation and a $^{87}Sr/^{86}Sr$ decline as elevation increases. However, a meaningful comparison of this result to the known fog climatology requires that we narrow the data to salts formed during the time of stable climate. Therefore, the dataset was filtered to exclude the sites previously categorized as low likelihood that they are Holocene, which leaves 28 data points (Fig. 2-5b; Table A1 in Appendix A). A sample-by-sample analysis of these criteria can be found in Figures A1-A15 in Appendix A.

In the complete dataset, $^{87}Sr/^{86}Sr$ varies between 0.70682 and 0.70875, with an outlier at 0.71195 (~1150 m.a.s.l.). The highest ratios are found at low altitudes (89% of all ratios higher than 0.7079 are located lower than 1150 m.a.s.l.). Also, there is an altitudinal band with high variability around 1150 m.a.s.l..

The outlier NC11-33 has a high likelihood of being Holocene (Table A1 in Appendix A). It also has one of the lowest Ca/Si ratio of the dataset, which suggests that an important component of its Sr is probably derived from silicate Ca. This could occur because of inclusion of adsorbed cations that were located in the exchange complexes of micas, which can be easily incorporated into the aqueous solutions that result from our separation procedure. This outlier is not considered further.

In the age-filtered dataset, we distinguish three altitudinal bands (Fig. 2-5b). The first band contains samples located between ~300 and ~1050 m.a.s.l. where $^{87}Sr/^{86}Sr$ is higher than or equal to 0.70788 and there is relatively little variability. A second altitudinal band is identified below 300 m.a.s.l., where two sites show low $^{87}Sr/^{86}Sr$ values, and one shows a high $^{87}Sr/^{86}Sr$ value. In the third band, for altitudes exceeding 1150 m.a.s.l., 6 out of 7 samples show values that are below the lowest ratio in the 300-1050 m.a.s.l. altitudinal band (the exception is NC11-49, 1533 m.a.s.l.).

Samples located near 1100 m.a.s.l. display a high degree of variability of the ^{87}Sr/^{86}Sr values yet that variability is less than in the unfiltered dataset.

We argue that the ^{87}Sr/^{86}Sr vs. altitude distribution for Holocene salt shows the contribution of the average Holocene (since ~10,000 yrs ago) marine aerosol system to the superficial deposits. In this sense, the *averaged-in-time fog zone* would correspond to the altitudinal band with highest ^{87}Sr/^{86}Sr ratios, ~300 and ~1050 m.a.s.l.. Whereas visual inspection shows ~1100 m.a.s.l. to correspond to the averaged-in-time fog zone upper limit, investigation of this critical boundary region is warranted. An important characteristic of the data set is that some altitudes have been sampled more densely than others. Therefore, to explore for detailed trends in the data requires the use of an estimator of mean deviation that normalizes for the number of samples (N) at each elevation. Division of the altitude domain into 100 m bins and calculation of the unbiased standard error of the mean (s, where $s = \sigma/\sqrt{N}$ and σ is the unbiased standard deviation) for each bin determines that the 1000-1100 m.a.s.l. bin has the highest s value (0.00021), compared to 0.00011 for the next highest s value corresponding to the 1100-1200 m.a.s.l. bin. Changing the bin width to 50 m.a.s.l. reveals that the 1050-1100 m.a.s.l. bin has the highest unbiased standard deviation, s.

An alternative approach is to compare two data samples using the Kolmogorov-Smirnov nonparametric test, which quantifies the difference between the two empirical distribution functions of two samples. In this case, these two samples correspond to the samples defined below and above a given altitude threshold. By conducting this test for several altitude thresholds, we can decide on the most probable time-averaged fog top as the one with the greatest difference between sample sets. For altitudes every 25 m between 1050 and 1250 m.a.s.l., the two sample sets are most different for an altitude threshold of 1075 m.a.s.l..

These results identify the upper time-averaged fog top at 1075 m.a.s.l.. Significantly, the top boundary for the high $^{87}Sr/^{86}Sr$ domain falls within DEM error of the previously defined observational top-of-the-fog altitude at 1100 m.a.s.l. [Cereceda et al., 2002; Farías et al., 2005].

With respect to the lower altitudinal boundary for the fog-influenced domain, visual inspection suggests a high variability between 200 and 250 m.a.s.l., A statistical analysis similar to that done for the top of the fog zone is not possible due to far fewer data points. Further sampling and measurements may improve the definition of a time-averaged lower marine aerosol boundary.

Distance from the coast and local, short-scale topographic variability may also explain in part the distribution of $^{87}Sr/^{86}Sr$ of Holocene salt accumulations. Studies of the spatial distribution of modern fog reveal significantly higher frequency of fog events in certain topographic corridors that transect the Coastal Cordillera [Farías et al., 2005]. We reason that those effects of complex topographic patterns that block or enhance air mass flow may in part explain variability within each domain (inside and outside the Holocene fog zone). Given the clear altitudinal control of the observational fog top, the first-order bi-modal nature of the $^{87}Sr/^{86}Sr$ distribution is best explained by altitude.

In summary, we interpret the domain between ~225 and 1075 m.a.s.l. to represent the land area under marine fog influence. Since salts sampled during our studies are younger than 10,000 years, these domain boundaries are interpreted as averaged over that time period.

2.5.5 Bootstrap analysis

Although Rech et al. [2003] offered one approach to quantifying the $^{87}Sr/^{86}Sr$ of an Andean end-member for the mixed sources of salts in Atacama modern soils (section 2.5), the robustness of that number depends upon whether the included samples are fully representative of all the non-marine processes affecting the Sr isotopic ratio. We can avoid making such assumptions by following another approach based on the statistical properties of the new data sets (Table A1 in Appendix A). In this new approach, we conceptualize a background Sr isotopic ratio, upon which deposition of salts from marine aerosols causes modification of this ratio. That background $^{87}Sr/^{86}Sr$ value would be the Andean average.

Commonly, geochemical variables are not normally distributed (and not log-normally distributed, for that matter), since many processes are at work to define elemental concentration or isotopic ratios in a given rock. Taking advantage of computer-intensive statistical methods such as *bootstrapping* [Efron, 1979], it is not necessary to assume a prior mathematical form for a given distribution at all. Instead, we can use our existing set of samples as an approximation of the underlying population. Specifically, given a dataset of size *n*, take samples with replacement of size *n* from that dataset to approximate samples of size *n* from the underlying population. In order to estimate the background modern (i.e. filtered dataset) non-marine Sr ratio and its standard error:

(i) randomly sample one isotope ratio from the complete n = 12 sub-dataset (number of outside-of-the-fog soil samples), then repeat this 11 times, and finally compute x (mean) of these 12 randomly-sampled isotope ratios,

(ii) repeat (i) a sufficient number of times *B* to come up with 'bootstrap' estimates $x_1, x_2, \ldots, x_B,$

(iii) use the standard deviation of the B estimates in step (ii) to estimate the standard error.

The estimate of mean and standard error of the mean converge quickly to 0.70746 and 0.00010 respectively, with high values of B (Fig. 2-5). This is then the background Sr ratio of modern accumulations of salts in the Atacama Desert, unaffected by marine fog. It coincides within error to 0.70749 ± 0.00046, the Andean average as defined by Rech et al. [2003].

Doing this same analysis with the inside-of-the-fog dataset (n = 9), we obtain a value of 0.70807 ± 0.00004 (Fig. 2-5). Thus, those two datasets belong to different populations. This reinforces our interpretation that the participation of marine fog in formation of superficial calcium sulfate minerals in the Atacama Desert has a clear signature in the resultant $^{87}Sr/^{86}Sr$. This reinforces previous studies that reached the same conclusion [Rech et al., 2003]. Note that neither the samples that fall within the high-variability altitudinal band centered on 1075 m.a.s.l. (time-averaged fog top) nor samples collected between 200 and 275 m.a.s.l. were considered for the bootstrapping.

2.6 Implications for $^{87}Sr/^{86}Sr$ paleoaltimetry

These results show that $^{87}Sr/^{86}Sr$ of modern accumulations of salts in the Atacama Desert, northern Chile, provide a proxy for their altitude of formation. The distribution with altitude of the Sr isotopic ratios is bi-modal with two threshold elevations (~225 m.a.s.l. and 1075 m.a.s.l.). If a comparable relationship existed for salts that formed soils during the Late Miocene through Pleistocene, then the $^{87}Sr/^{86}Sr$ value of pre-Holocene calcium sulfate may provide a measure of paleoaltitude that

would be useful for quantifying tectonically driven surface uplift or subsidence of the Andean forearc. As shown by Rech et al. [2006], Ewing et al. [2008] and Jordan et al. [2014], post-10 Ma buried Gypsisols and exposed relict gypsic soils are widespread and suitable for this paleoaltitude proxy.

The fundamental strategy of this potential paleoaltimeter is that the band of elevations above sea level in which marine fog supplies aerosols to the continental surface provides a reference altitude in a sea level reference frame. To consider the premises necessary for use of this paleoaltimeter, we consider the conditions extant during the Holocene and the likelihood of their stability into the deep geological past. The stability through time of the fog system along the western edge of South America is closely related to the stability of the low-altitude atmospheric temperature inversion in the area. The temperature inversion depends on the combination of regional atmospheric subsidence, cold offshore surface waters and to a lesser extent, the existence of the Andean highlands (section 2.1). The stability of regional atmospheric subsidence in the area is accepted as a result of an almost unchanged latitudinal position of the continent since 150 Ma [e.g. Beck et al., 2000]. The temperature of near-coastal waters has been like that of the modern Humboldt system at least since the Middle Miocene [Amiot et al., 2008]. Finally, more than half of the height of the modern western Andes Cordillera was achieved during the lower-middle Miocene [Gregory-Wodzicki, 2000; Victor et al., 2004; Farías et al., 2005]. Thus, it is to be expected that a persistent offshore low altitude atmospheric inversion layer existed since at least mid-Miocene times, although its altitude need not have been constant.

The ability of geological materials like gypsum and anhydrite to capture an environmental Sr ratio requires that there existed a climate prone to evaporation of fog and crystallization of calcium sulfate. Sillitoe and McKee [1996], Dunai et al. [2005], Rech et al. [2006] and Jordan et al. [2014] presented the evidence that hyperarid

conditions have been typical in the northern Chile forearc for more than 10 million years, although interrupted multiple times for intervals of arid conditions that persisted several hundred thousand to one million years [Jordan et al., 2014]. Therefore, both an analogous paleo-fog system and ancient superficial calcium sulfate deposits may have existed in Atacama Desert.

However, even if analogous relations of altitude to Sr ratio existed during the Late Miocene and Pliocene, it is unlikely that the altitudes of the thresholds and the $^{87}Sr/^{86}Sr$ values were equal to those in the recent past. Several factors of the atmosphere-ocean-land system, both global and local, likely have varied. First, the marine aerosol $^{87}Sr/^{86}Sr$ end-member is anchored to seawater $^{87}Sr/^{86}Sr$, which has changed with time. The secular trend of seawater $^{87}Sr/^{86}Sr$ is well known for the Neogene, rising from 0.70891 to 0.70917 since 10 Ma [Hodell et al., 1991; Farrell et al., 1995]. Second, climate change affects the atmospheric temperature inversion layer and with it the height of the top of the cloud deck above the sea surface [Wang et al., 2004]. Third, global sea level change as well as regional tectonics will both have changed the position of the intersection of sea level with the forearc morphology in a rock reference frame. Even if the "elevation above sea level" of the stratocumulus clouds were to have been constant in a sea level reference frame, global sea level change would alter the intersection of both sea level as well as the stratocumuli clouds with the continental surface in a rock-based reference frame. If the objective is to deduce tectonic uplift or subsidence, then the global sea level change with a magnitude of approximately 175 m during the past 10 million years [Miller et al., 2005] is an interfering signal.

The results presented here lead to the definition of criteria to decide whether a given paleosol was formed inside or outside of the paleo-fog zone that existed while the soil formed. One way to do this is to use the distribution of the outside-of-the-fog

calcium sulfate dataset and, under the bootstrap approximation that it coincides with the underlying population, define a likelihood that a given paleosol (with a given $^{87}Sr/^{86}Sr$ ratio) did not form outside of the paleo-fog zone. For a given paleosol with a $^{87}Sr/^{86}Sr$ value of x, and a given outside-of-the-fog sample size n, the likelihood of this paleosol having formed inside of the fog zone is $100*(p/n)$, where p is the number of outside-of-the-fog soil samples with $^{87}Sr/^{86}Sr$ lower than x.

2.7 Conclusions

We have developed a new bi-modal modern altitude proxy for continental surfaces in the Atacama Desert based on $^{87}Sr/^{86}Sr$ of Holocene superficial salt accumulations. The altitude-dependent phenomenon that underlies this proxy is the first-order topographic control on the spatial extent of marine fog events that advect aerosols inland from the southeast Pacific. As was shown in previous studies [e. g. Rech et al., 2003], evaporation of the water deposited on the land surface from the fog precipitates calcium sulfates on the landscape, and is one of the main contributors of gypsum and anhydrite to calcium sulfate dust and crusts in the Atacama Desert. On average during the last ~10,000 years, the isotopic signature of marine aerosol Sr, precipitated as calcium sulfates between ~225 and 1075 m.a.s.l. is distinctly higher than $^{87}Sr/^{86}Sr$ of salts sampled outside of this altitudinal domain. This Sr isotopic distinction provides a proxy that defines two altitudinal domains. This proxy has been shown to be effective along a ~200 km latitudinal band (19.5-21.5ºS).

Given a set of paleosols of known age, it may be possible to use this novel method as a paleoaltitude proxy. In order to do so, the polygenetic origin of the surficial salt accumulations as well as pedogenesis along vertical profiles of paleosols

and/or relict soils, among other considerations, require further scrutiny. Corrections that must be applied in order to isolate signals related to progressive topographic change include temporal variations in seawater $^{87}Sr/^{86}Sr$, global sea-level changes, and changes in the structure of the atmospheric inversion layer. This is a promising method with which to constrain the tectonic uplift history of the Nazca-South America forearc in northern Chile.

2.8 Acknowledgements

Supporting data is included as an extra table in .xls format in Appendix A; any additional data may be obtained from NJC (njc58@cornell.edu).

2.9 Tables

Table 2-1. Mineralogy of modern accumulation of salt samples[1].

Sample	Location	Distance from coast (km)	Altitude (± 30 m.a.s.l.)	Phases	Comments *
NC11-4	19°52'46.80'' S 70°07'35.04'' W	0.9	260	Gyp: 70% Cal: 20% Qz: 10%	Huara transect Salt-cemented, indurated surficial crust. Coastal escarpment. High confidence[+].
NC11-6	19°56'39.08'' S 70°03'06.63'' W	10.3	750	Gyp: 70% Qz: 30%	Huara transect. Light tan powdery material below gravel. Coastal Cordillera. Low confidence[+].
NC11-8	19°57'47.39'' S 69°37'30.07'' W	54.4	1210	Anh: 100%	Huara transect. White powdery material below gravel. Central Depression. High confidence[+].
NC11-12	19°45'27.01'' S 69°15'56.73'' W	93.6	2770	Qz: 80% Anh: 20%	Huara transect. White powdery material below gravel. Central Depression. High confidence[+].
NC12-74	19°29'01.33'' S 69°52'46.51'' W	35.5	1180	Qz: 40% Plg: 30% Gyp: 30%	Pisagua transect. White powdery material below gravel. Central Depression. High confidence[+].

[1] XRD analysis of selected modern accumulation of salts samples.
*See text for detailed sample description and for discussion of phase quantification uncertainty.
[+]Confidence that sample represents recently deposited (Holocene) materials. See text for discussion.
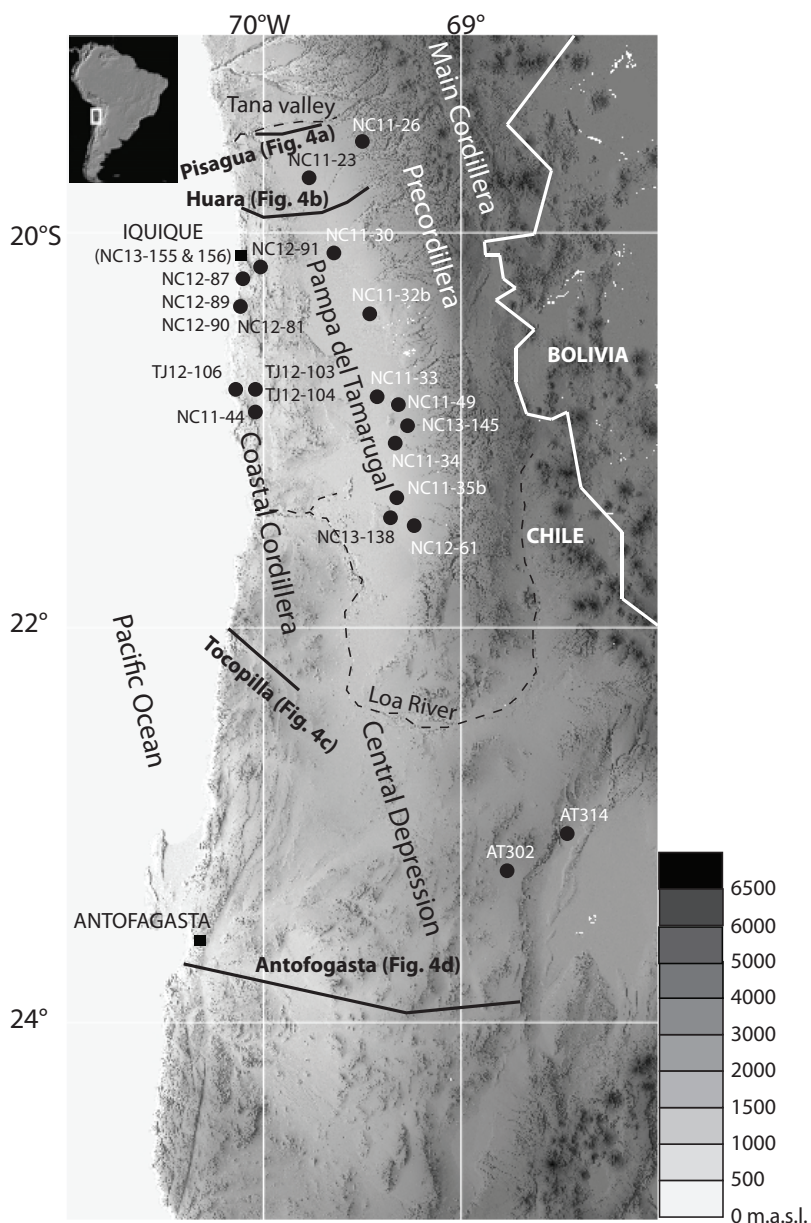
Figure 2-1. Main morphotectonic units of the inland forearc of the Nazca-South America plate system (see text for discussion). Topography is shown as a grey scale on the map, with shading accomplished by light coming from the west in order to better show topographic features. Black lines show the locations of the sample transects, of which the Tocopilla and Antofagasta transects were sampled by Rech et al. [2003]. Black dots are single sampling sites, of which AT302 and AT314 were sampled by Rech et al. [2003].

Figure 2-2. (a) Surficial white powdery intermixture of siliciclastic and salt material loosely attached to the bottom of pebbles, cobbles and boulders (upside-down boulder in the image); (b) widespread 10-20 cm-thick surficial tan/rusty brown crust composed of gypsum and anhydrite and with a low clast density, and usually developed over a bedrock parent material; (c) 2 cm-thick surficial light tan/white laterally continuous powdery material (chusca) below a mm-scale lag gravel; and (d) surficial mm-scale gypsum-rich crust.
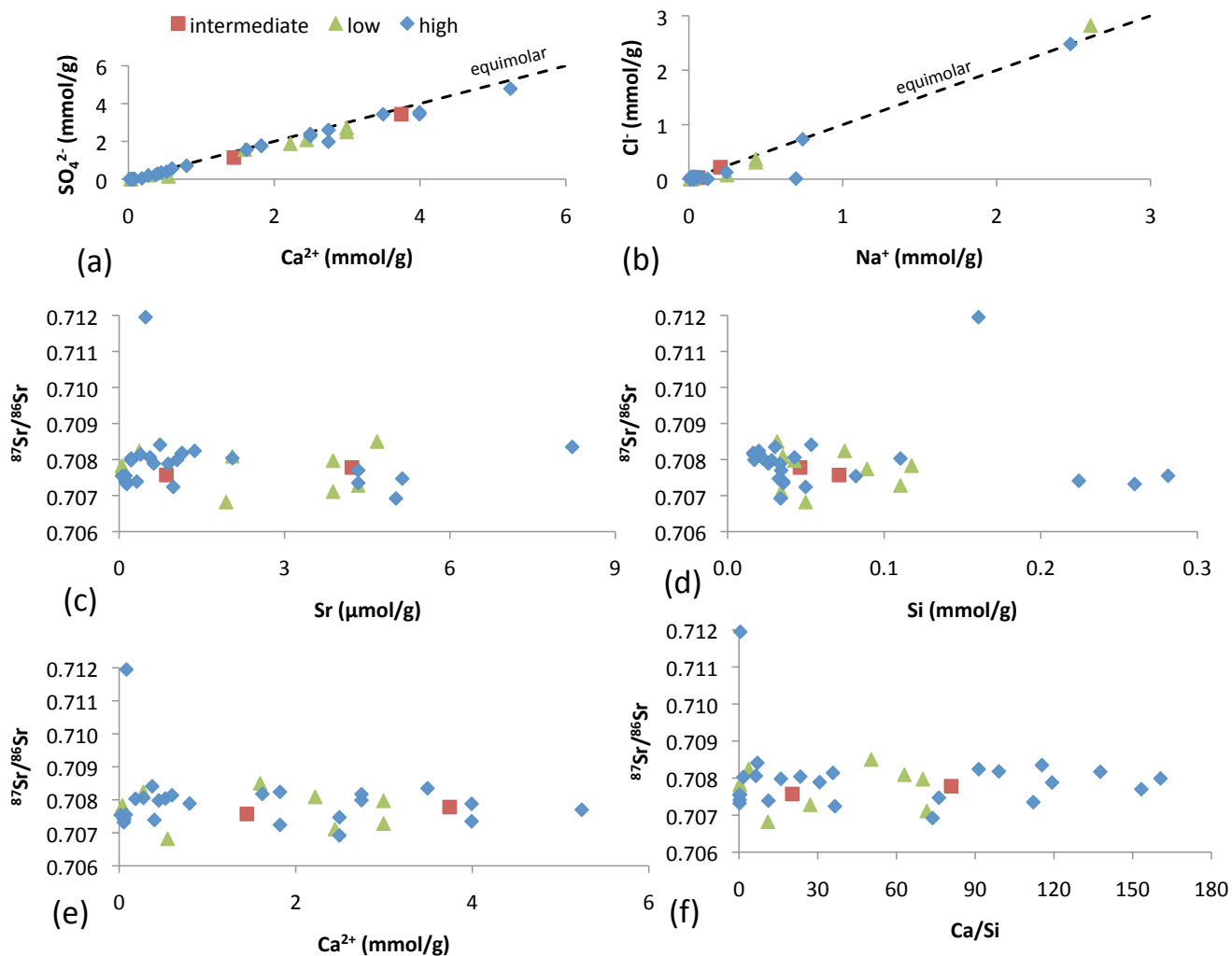
Figure 2-3. Chemistry and Sr isotopic ratio of the soluble fraction of modern accumulations of salt/siliciclastic samples. (a) Ca^{2+} vs. SO_4^{2-}, (b) Na^+ vs. Cl^-, (c) Sr vs. $^{87}Sr/^{86}Sr$, (d) Si vs. $^{87}Sr/^{86}Sr$, (e) Ca^{2+} vs. $^{87}Sr/^{86}Sr$, and (f) Ca/Si vs. $^{87}Sr/^{86}Sr$. Chemistry is expressed per gram of total solid sample. Color-coded according to the confidence of recent deposition: blue for high, red for intermediate, and green for low confidence (see text for discussion).
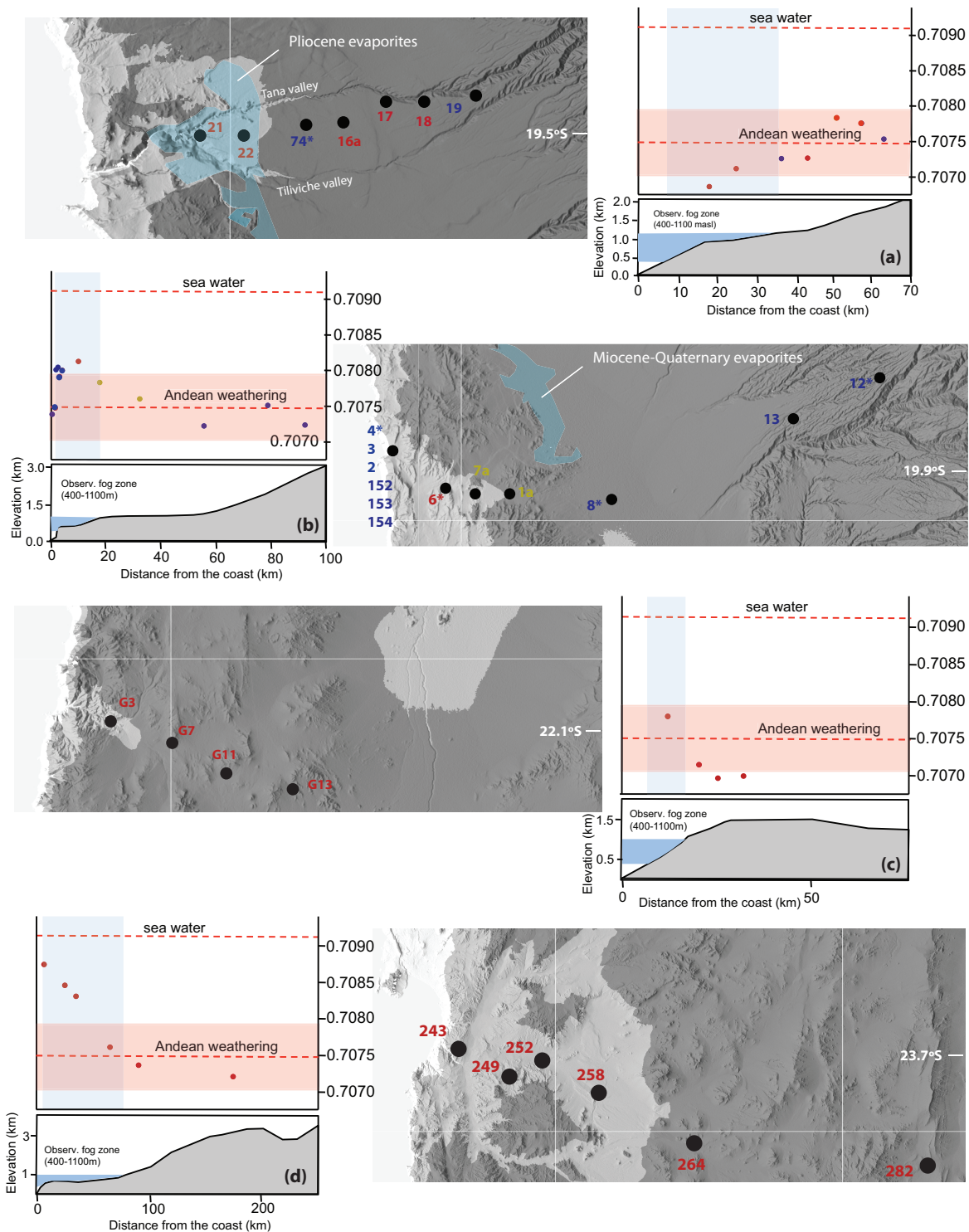
Figure 2-4. Sampled locations along the ~ E-W transects and $^{87}Sr/^{86}Sr$ results plotted against distance to the coast for (a) Pisagua transect, (b) Huara transect, (c) Tocopilla transect and (d) Antofagasta transect. Shown in light blue is the area with altitudes between 400 and 1100 m.a.s.l. (coastal fog zone). Samples for which XRD analysis was performed are asterisked (*). Samples with blue (yellow; red) font in the map and blue (yellow, red) dots in the graphs have a high (intermediate; low) certainty of having been formed in the Holocene. Seawater $^{87}Sr/^{86}Sr$ taken from Farrell et al. [1995] and Andean weathering $^{87}Sr/^{86}Sr$ average from Rech et al. [2003], including uncertainty (pink box).

49
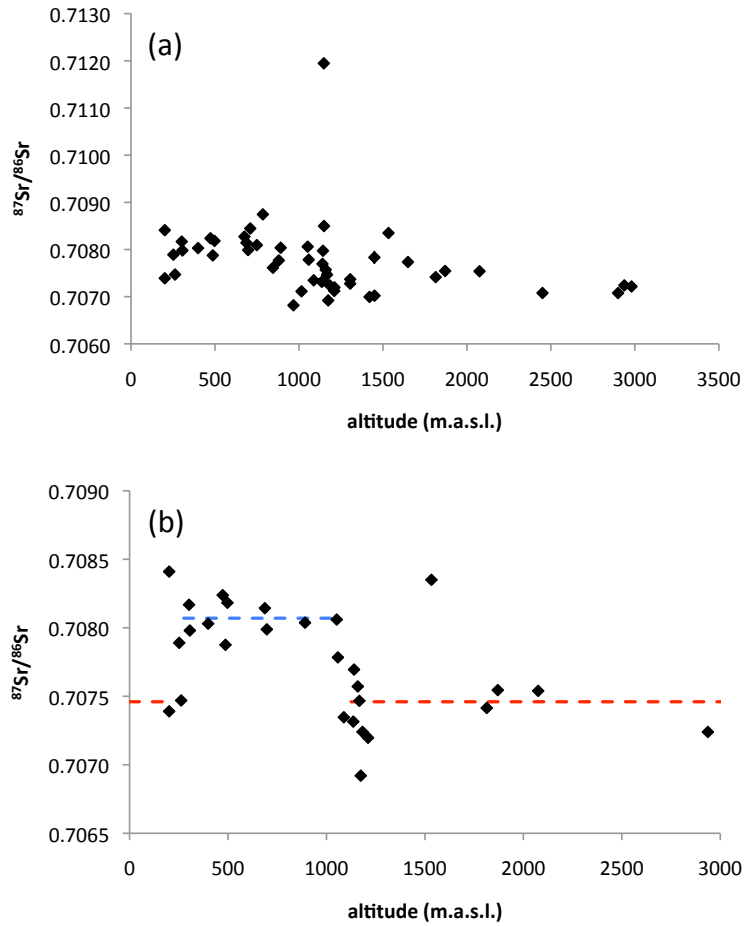
Figure 2-5. (a) Modern accumulations of salts' $^{87}Sr/^{86}Sr$ and altitude of formation for the whole dataset. (b) Subset of samples with high and intermediate certainty of recent deposition (see text for discussion). The red dashed line represents the bootstrap value for the time-averaged outside-of-the-fog isotopic ratio, while the blue dashed line corresponds to the inside-of-the-fog equivalent.

REFERENCES

Amiot, R., U. B. Gohlich, C. Lécuyer, C. de Muizon, H. Cappetta, F. Fourel, M. Héran and F. Martineau (2008), Oxygen isotope compositions of phosphate from Middle Miocene-Early Pliocene marine vertebrates of Peru, Palaeogeography, Palaeoclimatology, Palaeoecology, 264, 85-92.

Amundson, R., W. Dietrich, D. Bellugi, S. Ewing, K. Nishiizumi, G. Chong, J. Owen, R. Finkel, A. Heimsath and B. Stewart (2012), Geomorphologic evidence for the late Pliocene onset of hyperaridity in the Atacama Desert, Geological Society of America Bulletin, 124, 1048-1070.

Azúa-Bustos, A., C. González-Silva, R. A. Mancilla, L. Salas, B. Gómez-Silva, C. P. McKay and R. Vicuña (2011), Hypolithic cyanobacteria supported mainly by fog in the coastal range of the Atacama Desert, Microbial ecology, 61(3), 568-581, doi: 10.1007/s00248-010-9784-5.

Beck, M., R. Bermester, J. Cembrano, R. Drake, A. García, F. Hervé and F. Munizaga (2000), Paleomagnetism of the North Patagonian Batolith, southern Chile. An exercise in shape analysis, Tectonophysics, 326(1-2), 185-202.

Bourgois, J. (2010), A comment on "Non-steady long-term uplift rates and Pleistocene marine terrace development along the Andean margin of Chile (31ºS) inferred from [10]Be dating" by M. Saillard, S. R. Hall, L. Audin, D. L. Farber, G. Hérail, J. Martinod, V. Regard, R. C. Finkel, F. Bondoux, Earth and Planetary Science Letters, 296(3), 502-505.

Cereceda, P., R. S. Schemenauer and F. Velásquez (1997), Variación temporal de la niebla en El Tofo-Chungungo, Región de Coquimbo, Chile, Revista Geográfica Norte Grande, 24, 191–193.

Cereceda, P. and R. S. Schemenauer (1998), Fogwater collection at El Tofo, Chile and other coastal sites in South America and Arabia, In Proceedings of the First International Conference on Fog and Fog Collection (eds. R. S. Schemenauer and H. Bridgman). Vancouver, Canada, 19 – 24 July, pp. 409-411.

Cereceda P., P. Osses, H. Larrain, M. Farías, M. Lagos, R. Pinto and R. S. Schemenauer (2002), Advective, orographic and radiation fog in the Tarapacá region, Chile, Atmospheric Research, 64, 261-271.

Cereceda, P., H. Larrain, P. Osses, M. Farías and I. Egaña (2008), The spatial and temporal variability of fog and its relation to fog oases in the Atacama Desert, Chile, Atmospheric Research, 87, 312-323.

CNE – Ministerio de Energía – Gobierno de Chile (2009), Modelación de recurso solar y eólico en el norte de Chile.

Comte, D. and M. Pardo (1991), Reappraisal of great historical earthquakes in the northern Chile and southern Peru seismic gaps, Natural Hazards, 4, 23-44.

Dunai, T. J., G. A. González López and J. Juez-Larré (2005), Oligocene-Miocene age of aridity in the Atacama Desert revealed by exposure dating of erosion-sensitive landforms, Geology, 33(4), 321-324.

Efron, B. (1979), Bootstrap methods: Another Look at the Jackknife, The Annals of Statistics, 7(1), 1-26.

Espejo, R. (2001), Climatological and microbiological characteristics of the camanchaca phenomenon at Cerro Moreno, Antofagasta, Chile, In Proceedings of the Second International Conference on Fog and Fog Collection (eds. R. S. Schemenauer and H. Puxbaum). St. John's, Canada, 15–20 July, pp. 463–466.

Ewing, S. A., B. Sutter, J. Owen, K. Nishiizumi, W. Sharp, S. S. Cliff, K. Perry, W. Dietrich, C. P. McKay, and R. Amundson (2006), A threshold in soil formation at Earth's arid-hyperarid transition, Geochim. Cosmochim. Acta, 70, 5293-5322.

Ewing, S. A., Yang, W., DePaolo, D. J., Michalski, G., Kendall, C., Stewart, B. W., Thiemens, M. and R. Amundson (2008), Non-biological fractionation of stable Ca isotopes in soils of the Atacama Desert, Chile, Geochim. Cosmochim. Acta, 72, 1096-1100.

Farías, M., P. Cereceda, P. Osses and R. Núnez (2005), Spatial and temporal behavior of the stratocumulus cloud, fog producer in the coast of the Atacama desert (21º south lat., 70º west long.), during one month of winter and another of summer, Investigaciones Geográficas, Boletín del Instituto de Geografía, UNAM, 56, 43-61.

Farías, M., R. Charrier, D. Comte, J. Martinod and G. Hérail (2005), Late Cenozoic deformation and uplift of the western flank of the Altiplano: Evidence from the depositional, tectonic, and geomorphologic evolution and shallow seismic activity (northern Chile at 19º30'S), Tectonics, 24.

Farías, M., R. Charrier, S. Carretier, J. Martinod, A. Fock, D. Campbell, J. Cáceres and D. Comte (2008), Late Miocene high and rapid surface uplift and its erosional response in the Andes of central Chile (33º-35ºS), Tectonics, 27.

Farrell, J. W., S. C. Clemens and L. P. Gromet (1995), Improved chronostratigraphic reference curve of late Neogene seawater ^{87}Sr/^{86}Sr, Geology, 23, 403-406.

Ferranti, L., C. Monaco, F. Antonioli, L. Maschio, S. Kershaw and V. Verrubbi (2007), The contribution of regional uplift and coseismic slip to the vertical crustal motion in the Messina Straits, southern Italy: Evidence from raised Late Holocene shorelines, Journal of Geophysical Research: Solid Earth, 112, B6.

Garzione, C. N., G. D. Hoke, J. C. Libarkin, S. Withers, B. J. MacFadden, J. M. Eiler, P. Gosh and A. Mulch (2008), Rise of the Andes, Science, 320, 1304–1307.

Gayó, E. M., C. Latorre, T. E. Jordan, P. L. Nester, S. A. Estay, K. F. Ojeda and C. M. Santoro (2012), Late Quaternary hydrological and ecological changes in the hyperarid core of the northern Atacama Desert (~21°S), Earth-Science Reviews, 113, 120-140.

Gregory-Wodzicki, K. M. (2000), Uplift history of the Central and Northern Andes: a review, Geological Society of America Bulletin, 112, 1091–1105.

Herrera, C. and E. Custodio (2014), Origin of waters from small springs located at the northern coast of Chile, in the vicinity of Antofagasta, Andean Geology, 41, 314-341.

Hodell, D. A., P. A. Mueller and J. R. Garrido (1991), Variations in the strontium isotopic composition of seawater during the Neogene, Geology, 19, 24-27.

Hoke, G. D., B. L. Isacks, T. E. Jordan, N. Blanco, A. J. Tomlinson and J. Ramezani (2007), Geomorphic evidence for post-10 Ma uplift of the western flank of the central Andes, 18º30' – 22ºS, Tectonics, 26.

Horwitz, E. P., R. Chiarizia and M. L. Dietz (1992), A novel strontium-selective extraction chromatographic resin, Solvent Extraction & Ion Exchange, 10, 313.

Houston, J. and A. J. Hartley (2003), The Central Andean west-slope rainshadow and its potential contribution to the origin of hyper-aridity in the Atacama Desert, Inter- national Journal of Climatology, 23, 1453–1464.

Insel, N., C. J. Poulsen, T. A. Ehlers and C. Sturm (2012), Response of meteoric $\delta^{18}O$ to surface uplift – Implications for Cenozoic Andean Plateau growth, Earth and Planetary Science Letters, 317-318, 262-272.

Jordan, T. E., P. L. Nester, N. Blanco, G. D. Hoke, F. Dávila and A. J. Tomlinson (2010), Uplift of the Altiplano-Puna plateau: A view from the west, Tectonics, 29.

Jordan, T. E., N. E. Kirk-Lawlor, N. Blanco, J. A. Rech and N. J. Cosentino (2014), Landscape modification in response to repeated onset of hyperarid paleoclimate states since 14 Ma, Atacama Desert, Chile, Geological Society of America Bulletin, 126, B30978-B30971.

Kahle, M., M. Kleber and R. Jahn (2002), Review of XRD-based quantitative analyses of clay minerals in soils: the suitability of mineral intensity factors, Geoderma, 109, 3-4, 191-205.

Keene, W. C., Pszenny, A. A., Galloway, J. N. and M. E. Hawley (1986), Sea-salt corrections and interpretation of constituent ratios in marine precipitation, J. Geophys. Res., 91, 6647-6658.

Keller, G., T. Adatte, W. Stinnesbeck, D. Stuben, U. Kramar, Z. Berner, L. Li and K. Perch-Nielsen (1997), The Cretaceous-Tertiary transition on the shallow Saharan Platform of southern Tunisia, Geobios, 30(7), 951-975.

Kirk-Lawlor, N. E., T. E. Jordan, J. A. Rech and S. B. Lehmann (2013), Late Miocene to Early Pliocene paleohydrology and landscape evolution of northern Chile, 19 to 20ºS, Palaeogeography, Palaeoclimatology, Palaeoecology, 387, 76-90.

Lehmann, S., J. A. Rech, B. S. Currie, T. E. Jordan and R. Riquelme (2009), Redefining the Tarapacá pediplain: analysis of relict soils in the northern Atacama Desert, Chile, paper presented at 2009 GSA Annual Meeting, Portland, USA.

Marquardt, C., J. A. Naranjo and A. Lavenu (2006), Efectos geológicos del sismo del 13 de junio 2005, región de Tarapacá: XI Congreso Geológico Chileno, 2, 435-438.

Marquet, P. A., C. M. Santoro, C. Latorre, V. G. Standen, S. R. Abades, M. M. Rivadeneira, B. Arriaza and M. E. Hochberg (2012), Emergence of social complexity among coastal hunter-gatherers in the Atacama Desert of northern Chile, Proceedings of the National Academy of Sciences of the United States of America, 109, 37, 14754-14760.

Miller, K. G., M. A. Kominz, J. V. Browning, J. D. Wright, G. S. Mountain, M. E. Katz, P. J. Sugarman, B. S. Cramer, N. Christie-Blick and S. F. Pekar (2005), The Phanerozoic record of global sea-level change, Science, 310(5752), 1293.

Millero, F. J. (1974), Seawater as a multicomponent electrolyte solution, In The Sea (ed. E. D. Goldberg), John Wiley & Sons, New York, 3-80.

Mintz, Y. and G. K. Walker (1992), Global fields of soil moisture and land surface evapotranspiration derived from observed precipitation and surface air temperature, J. Appl. Meteorol., 32, 1305–1334.

Moore, D. M. and R. C. Reynolds (1997), X-ray diffraction and the identification and analysis of clay minerals, Oxford University Press, Oxford, New York.

Morell, K. D., D. M. Fisher, T. W. Gardner, P. La Femina, D. Davidson and A. Teletzke (2011), Quaternary outer fore-arc deformation and uplift inboard of the Panama Triple Junction, Burica Peninsula, Journal of Geophysical Research, 116.

Mortlock, R. A. and P. N. Froelich (1989), A simple method for the rapid determination of biogenic opal in pelagic marine sediments, Deep Sea Research Part A. Oceanographic Research Papers, 36(9), 1415-1426.

Muzzio, J. G. (1986), Geología de los cuadrángulos Caleta Camarones, Cuya, Punta Gorda, y Cerro Atajaña, I region, Chile: Informe de Avance. Serv. Nac. de Geol. y Minería, Santiago, Chile.

Orellana Cortés, H. H. (2010), Aspectos geodinámicos del desierto costero de Atacama, sector Alto Patache (Oasis de Niebla) y Bajo Patache, M.S. thesis, Universidad de Chile, Santiago, Chile.

Pizarro, O., S. Hormazábal, A. González and E. Yañez (1994), Coastal wind, sea level and temperature variability in the north of Chile, Invest. Mar Valparaíso, 22, 85-101.

Quade, J., J. A. Rech, J. L. Betancourt, C. Latorre, B. Quade, K. Aasen Rylander and T. Fisher (2008), Paleowetlands and regional climate change in the central Atacama Desert, northern Chile, Quaternary Research, 69, 343-360.

Rech, J. A., J. Quade and W. S. Hart (2003), Isotopic evidence for the source of Ca and S in soil gypsum, anhydrite and calcite in the Atacama Desert, Chile, Geochimica et Cosmochimica Acta, 67(4), 575-586.

Rodwell, M. and B. Hoskins (2001), Subtropical anticyclones and summer monsoons, J. Climate, J. Climate, 14(15), 3192-3211.

Rowley, D. B. and C. N. Garzione (2007) Stable isotope-based paleoaltimetry, Annual Review of Earth and Planetary Sciences, 35, 463-508.

Saillard, M., S. R. Hall, L. Audin, D. L. Farber, G. Hérail, J. Martinod, V. Regard, R. C. Finkel and F. Bondoux (2009), Non-steady long-term uplift rates and Pleistocene marine terrace development along the Andean margin of Chile (31ºS) inferred from [10]Be dating, Earth and Planetary Science Letters, 277, 50-63.

Saillard, M., S. R. Hall, L. Audin, D. L. Farber, V. Regard and G. Hérail (2011), Andean coastal uplift and active tectonics in southern Peru: [10]Be surface exposure dating of differentially uplifted marine terrace sequences (San Juan de Marcona, ~ 15.4ºS), Geomorphology, 128(3-4), 178-190.

Sak, P. B., D. M. Fisher, T. W. Gardner, J. S. Marshall and P. C. LaFemina (2009), Rough crust subduction, forearc kinematics, and Quaternary uplift rates, Costa Rican segment of the Middle American Trench, GSA Bulletin, 121(7-8), 992-1012.

Schemenauer, R. S. and P. Cereceda (1992), The quality of fog water collected for domestic and agricultural use in Chile, Journal of Applied Meteorology, 31, 275-290.

Schlunegger, F., G. Zeilinger, A. Kounov, F. Kober and B. Husser (2006), Scale of relief growth in the forearc of the Andes of Northern Chile (Arica latitude, 18ºS), Terra Nova, 18(3), 217-223.

Searl, A. and S. Rankin (1993), A preliminary petrographic study of the Chilean
nitrates, Geol. Mag., 130(3), 319-333.

SERNAGEOMIN (2003), Mapa Geológico de Chile: versión digital. *Servicio
Nacional de Geología y Minería, Publicación Geológica Digital*, No. 4 (CD-
ROM, versión 1.0). Santiago.

Sillitoe, R. H. and E. H. McKee (1996), Age of supergene oxidation and enrichment in
the Chilean porphyry copper province, Economic Geology, 91, 164-179.

Sträter, E., A. Westbeld and O. Klemm (2010), Pollution in coastal fog at Alto
Patache, northern Chile, Environ. Sci. Pollut. Res., doi: 10.1007/s11356-010-0343-
x.

Takahashi, K. and D. Battisti (2007), Processes controlling the mean tropical Pacific
precipitation pattern, J. Climate, 20, 3434-3451.

UNEP/GRID: United Nations Environment Program/Global Resource Information
Database (1991), Global digital data sets for land degradation studies: a GIS
approach. *Prepared by U. Deichmann and L. Eklundh. GRID Case Study Series
No. 4. UNEP/GEMS and GRID. Nairobi, Kenya*.

Vargas, G. and L. Ortlieb (1998), Patrones de variaciones climáticas durante el
Cuaternario tardío en la costa de la Región de Antofagasta, Chile, Bulletin de
l'Institut Françáis d'Etudes Andines, 27(3), 385-394.

Vásquez, P. and F. A. Sepúlveda (2013), Cartas Iquique y Pozo Almonte, Región de
Tarapacá. Servicio Nacional de Geología y Minería, Carta Geológica de Chile,
Serie Geología Básica, Nos. 162-163, 1 mapa escala 1:100.000. Santiago.

Victor, P., O. Oncken and J. Glodny (2004), Uplift of the western Altiplano plateau:
Evidence from the Precordillera between 20 and 21º S (northern Chile), Tectonics,
23(4).

Vivallo, W. and F. Henriquez (1998), Génesis común de los yacimientos
estratoligados y vetiformes de cobre del Jurásico Medio a Superior en la Cordillera
de la Costa, Región de Antofagasta, Chile, Revista Geologica de Chile, 25, 199-
228.

Wang, Y., H. Xu and S. Xie (2004), Model simulations of marine boundary layer
clouds over the southeast Pacific off South America. Part II: sensitivity
experiments, Monthly Weather Review, 132, 2650-2668.

CHAPTER 3

^{87}SR/^{86}SR OF CALCIUM SULFATE IN ANCIENT SOILS OF HYPERARID

SETTINGS AS A PALEOALTITUDE PROXY: PLIOCENE TO QUATERNARY

CONSTRAINTS FOR NORTHERN CHILE (19.5-21.7ºS)[*]

3.1 Abstract

Several lines of geomorphic and geophysical reasoning suggest that the western forearc of northern Chile has undergone kilometer-scale surface uplift relative to sea level during the late Neogene. We have developed a new paleoaltimeter based on the ^{87}Sr/^{86}Sr ratio of ancient gypsic soils in the hyperarid Atacama Desert, and used it to investigate the uplift history of the Andean forearc coastal mountain range (Coastal Cordillera) and of the Andean forearc nonmarine basin surface (Central Depression). Sampled sites span ~330 km strike-parallel distance and elevations between 450 and 1850 m.a.s.l.. A minority of the sites place firm constraints on minimum or maximum vertical movements in an absolute framework. For the majority of locations, the data determine a maximum permissible magnitude of uplift. In all cases the magnitudes of paleo-elevation changes are small compared to the elevation of the study area relative to sea level. We conclude that more than 45% of the ~1000-m.a.s.l. average elevation of the Central Depression main axis and that more than 70% of the ~900 m.a.s.l. average elevation of the westernmost Coastal Cordillera in the study area were achieved by pre-early Pliocene regional scale

tectonic processes. These results refute the hypothesis of kilometer-scale surface uplift of the western nonmarine Andean forearc during the late Neogene.

3.2 Introduction

Three lines of geomorphic and geophysical reasoning suggest that the western forearc of the central sector of the Nazca-South American plate convergence system, west of the Andean Altiplano-Puna plateau, has undergone kilometer-scale surface uplift relative to sea level during the Neogene. In northern Chile and southernmost Peru, the morphologically youthful condition of deeply incised canyons that cross the Coastal Range and forearc basin [e.g. Schlunegger et al., 2006] and a comparison between a transect of crustal thickness and surface elevation [Victor et al., 2004] both lead to hypothetical explanations that can include kilometer-scale uplift of the forearc during the last 10 million years. In northern Chile, an abrupt increase in surface elevation across a Coastal Escarpment constitutes a major out-of-equilibrium geomorphological feature, which also leads to the hypothesis that large magnitude uplift occurred in the comparatively recent past [e.g. Hoke et al., 2007].

East of the forearc, two competing histories for the Neogene surface elevation evolution of the adjacent Altiplano Plateau have been put forward: (i) slow uplift since the early Miocene or before [e.g. Hartley et al., 2007; Barnes and Ehlers, 2009], and (ii) rapid ~2.5 km uplift between 11 and 6 Ma [e.g. Garzione et al., 2006; Ghosh et al., 2006]. Other studies that looked at the relief growth of the easternmost Central Depression and Precordillera in the eastern forearc are more consistent with the slow Altiplano Plateau uplift hypothesis [Victor et al., 2004; Farías et al., 2005; Hoke et al., 2007; Jordan et al., 2010; Evenstar et al., 2015]. Nonetheless, the forearc is a separate

tectonic regime and may have experienced a different uplift history than the Andean region. Yet, comparatively, little attention has been given to study of absolute surface elevation evolution of the Coastal Cordillera and Central Depression during the Neogene (Table 3-1). Until recently there did not exist appropriate isotopic-geologic proxies that could be used to infer surface elevation change in the Atacama Desert.

In this paper, it is our aim to test the hypothesis that there was ~1 km of absolute (i.e. relative to modern sea level) uplift of the western, nonmarine forearc in northern Chile during the late Neogene. To accomplish this, we present a new absolute paleoaltimetry proxy based on $^{87}Sr/^{86}Sr$ of ancient soils of the Atacama Desert. The paleoaltimeter is based on the observed altitude dependence of $^{87}Sr/^{86}Sr$ in modern accumulations of salts in the area [Chapter 2; i.e. Cosentino et al., 2015]. The geological record of environmental salts are relict gypsic soils and paleosols which accumulate only under hyperarid climate conditions. The paleoaltimetric results presented here refute the hypothesis of 1 km of uplift since the early Pliocene for the forearc basin and also demonstrate that it is unlikely to be true for the coastal mountain range.

3.2.1 The Atacama Desert: hyperaridity and longevity

The study area in northern Chile encompasses a ~330 km long sector of the plate boundary system (Fig. 3-1). From west to east, the main morphotectonic units correspond to a narrow coastal platform, an abrupt coastal cliff, a coastal range, and a valley (Central Depression) that gently tilts to the west (Fig. 3-1; Fig.3- 2). The Central Depression is the modern expression of the long-lived Pampa del Tamarugal forearc basin, with Oligocene to recent strata [Nester and Jordan, 2011]. The study area is bounded to the east by the Precordillera.

Three factors explain the study area's modern hyperaridity: i) large-scale atmospheric subsidence, ii) the near-shore equatorward Humboldt current and iii) local atmospheric subsidence on the western side of the Andes [e.g., Houston & Hartley, 2003; Insel et al., 2009; Garreaud et al., 2010]. It can be assumed that the regional atmospheric subsidence would be stable over many millions of years, the result of an almost unchanged latitudinal position of the continent since 150 Ma [e.g., Beck et al., 2000]. Paleoceanographic studies show that a cold water near-shore current like the modern Humboldt current has existed most of the time since at least the Middle Miocene [Amiot et al., 2008]. Furthermore, the fact that more than half of the modern altitude of the western Andes Cordillera was achieved during the early and middle Miocene [Gregory-Wodzicki, 2000; Victor et al., 2004; Farías et al., 2005b] suggests that the local-scale atmospheric subsidence known today on the western side of the Andes would also have existed since the middle Miocene. Thus, conditions conducive to hyperaridity existed in the study area since at least mid-Miocene times.

The time of onset of hyperaridity in northern Chile is still a matter of debate. Based on very different techniques, some studies place it as far back as 26 Ma [Dunai et al., 2005], while others as recently as 2 Ma [Amundson et al., 2012]. Other studies are interpreted to suggest intermediate onsets of hyperaridity at 15 Ma [Evenstar et al., 2009], at ~14 Ma [Sillitoe & McKee; 1996; Arancibia et al., 2006], prior to 10 Ma [Rech et al., 2006], at ~8-7 Ma [Schlunegger et al., 2010; Sáez et al., 2012] and at ~3 Ma [Hartley & Chong, 2002]. Jordan et al. [2014] propose that this divergence in opinions may be the result of a multiplicity of times of onset of hyperaridity and of subsequent shifts towards less arid conditions in northern Chile. These authors studied depositional sedimentary structures and relict soil and paleosols in the central and southern parts of our study area, and showed that predominantly hyperarid conditions prevailed there since ~12-11 Ma [Jordan et al., 2014]. They documented an onset of

hyperaridity at ~11 Ma, with hyperarid stages ~11-5.5 Ma (Stage NIb), 4.5-4 Ma
(Stage NIIb), 3.6-2.6 Ma (Stage NIIIb), 2.2-1 Ma (Stage NIVb) and repeated intervals
during the last 1 myr (Stage NV). Intervening wetter periods, with arid conditions,
occurred roughly between 5.5-4.5 Ma (Stage NIIa), 4-3.6 Ma (Stage NIIIa), 2.6-2.2
Ma (Stage NIVa) and repeated intervals during the last 1 myr [Jordan et al., 2014].

3.2.2 Spatial distribution of Atacama Desert paleosols and relict soils

Ancient gypsic soils occur in multiple parts of the forearc landscape, broadly
covering low relief geomorphic surfaces known regionally as the "Atacama Pediplain"
[García and Hérail, 2005] in the Central Depression and the "Coastal Tarapacá
Pediplain" [Mortimer and Saric Rendic, 1975] in the Coastal Cordillera. The same
basic history is laterally continuous from 18.5°S to 22°S for the Central Depression
across an elevation range from 900 m.a.s.l. in the west to ~2500 m.a.s.l. in the east
[Naranjo and Paskoff 1985; Kober et al., 2006; Hoke et al., 2007; García et al., 2011;
Jordan et al., 2014]: deposition of Upper Oligocene to Upper Miocene alluvial fans
followed by localized incision of drainages, unsteady westward translation of heads of
still active alluvial fans, and abandonment of relict fan surfaces between incised
canyons. The soils occur widely on the depositionally abandoned piedmont slope.
Each gypsic soil occurs as either a resistant cemented unit at the modern landscape
surface (gypsic relict soils) or as gypsic paleosols or Gypsisols [e.g. Mack et al., 1993]
buried by deposition during a less arid phase.

Across the study area, gypsic relict soils, though widespread, are not uniformly
available nor thick. The spatial variability and thickness of these soils depends on (i)
the time-integrated supply of atmospheric-derived salts, (ii) local (i.e. Coastal
Cordillera or Central Depression) precipitation variability, (iii) wind erosion or burial

by wind-blown sand, and (iv) spatial and temporal variability of stream delivery of alluvial fan sediments from the Precordillera. Combinations of some of these process factors result in local geographic settings that strongly favor gypsic soils. For example, proximity to salars and local wind patterns directed from a salar to a particular landscape position enhance salt deposition rates [McFadden et al., 1986; Rech et al., 2003]. Other combinations of these factors create a ~75-km-wide latitudinal band (20-20.6ºS) (Fig. 3-1) where such soils are infrequent. At these latitudes, eolian sand sheets and dunes cover the abandoned sectors of alluvial fans instead, both in the Pampa del Tamarugal forearc basin and in the Coastal Cordillera.

3.2.3 Constraints on the Late Cenozoic uplift history of the non-marine Andean forearc

An intercalated ≥ 24.5 Ma marine horizon in the Upper Oligocene - Lower Miocene upper Moquegua Formation now lies at 1800-2300 meters above sea level (m.a.s.l.) in the Andean piedmont between the Coastal and Western Cordilleras in southwestern Peru. To explain this, Thouret et al. [2007] inferred uplift of the piedmont with respect to sea level between 25 and 14 Ma. Also in southwest Peru, and based on structural and (U-Th)/He thermochronologic studies, on the depositional age of the uppermost fluvial sediments in the piedmont, and on river profiles, Schildgen et al. [2009] used the onset of river incision after ~5 Ma in the piedmont to infer up to 1 km of coupled uplift of the piedmont region and the plateau margin after ~5 Ma and prior to 2.2 Ma.

Based on stream profile analysis at 18ºS, Schlunegger et al. [2006] conclude that an unspecified amount of whole-block absolute surface uplift of the Andean

forearc took place sometime between depostion of El Diablo Formation (c. 8 Ma) and deposition of the Lauca Ignimbrite (3-2.6 Ma), with no further relief growth after that.

Kirk-Lawlor et al. [2013] demonstrated the existence of a deep-water lake and subsequently a salar during the Late Miocene and Pliocene in the westernmost Pampa del Tamarugal basin (19.3-19.8ºS). The eventual demise of this lake system was associated with a ~1 km drop in the paleolake's base level and canyon incision more recently than 3 Ma [Kirk-Lawlor et al., 2013]. They attribute this base level drop to a combination of coastal retreat and continental forearc uplift, but specify that the uplift may have pre-dated the time of incision. Instead, García et al. [2011] attribute to short-lived climate changes the initiation of canyon incision in the area, and credit the high-altitude of the forearc to pre-Neogene uplift. Jeffery et al. [2013] reach a similar conclusion for the initiation of the Ocoña River in southwest Peru.

Evenstar et al. [2015] used the altitude control on the production rate of in situ cosmogenic nuclides to constrain the absolute uplift history of the easternmost margin of the Central Depression, located in the Andean forearc. Based on the concentration of ^{3}He in alluvial boulders at two sites, they argue that most of the current elevation of the eastern Central Depression at 19.6ºS was achieved prior to 13.4 Ma [Evenstar et al., 2015].

Regard et al. [2010] argue that along ~1500 km of coast (16-30ºS) there has been spatially continuous coastal uplift since 400 ± 100 ka, as evidenced from an almost continuous cliff foot lying at 110 ± 20 m.a.s.l. along the study area. This period of uplift would have been preceded in the late Pliocene by quiescence or subsidence [Regard et al., 2010]. However, this Middle Pleistocene age for the onset of uplift may be underestimated, and thus its rate overestimated, by terrace reoccupation processes [Melnick, 2016].

Other studies place constraints on the differential uplift history of the eastern limit of the forearc relative to the Altiplano Plateau. Hoke et al. [2007] used downstream modeling of knickpoint-bounded segments of fluvial valleys in northern Chile between 18.5ºS and 22ºS to infer that at least 1 km of differential uplift took place since 10 Ma. This has been confirmed by the study of stratigraphic markers along the eastern flank of the forearc both at surface exposures and in the subsurface using seismic data, revealing that 810 m (± 640 m) of differential uplift took place between ~11 and ~5 Ma, and another 400 m (± 170 m) since ~5 Ma, in both cases across a long-wavelength monoclinal fold limb [Jordan et al., 2010].

3.2.4 $^{87}Sr/^{86}Sr$ of old gypsic soils as a proxy for surface elevation change

Salt precipitation occurs widely across the forearc Atacama Desert, leaving calcium sulfate minerals as a surficial dust or as a millimeter-scale crust on rock surfaces. Two reported cases of entombment in calcium sulfates of newspapers from the early twentieth century demonstrate a high rate of development of gypsum and anhydrite under modern conditions [Searl and Rankin, 1993; D. Burr and R. Jacobsen, personal communication, 2014]. Based on the first-order topographic control on the spatial extent of marine aerosols [Cereceda et al., 2002; Farías et al., 2005a] and the small fractionation of Sr isotopes, it has been possible to construct a modern altitude proxy based on $^{87}Sr/^{86}Sr$ of these modern accumulations of salts in the landscape (Fig. 3-2b) [Chapter 2; i.e. Cosentino et al., 2015]. This $^{87}Sr/^{86}Sr$ - altitude distribution is bi-modal, with high $^{87}Sr/^{86}Sr$ ratios inside the height band of time-averaged (10^4 yrs) influence by marine aerosols, and low values outside of that elevation range. This height band, which we call the *Holocene time-averaged fog zone*, is bounded below by a zone from the sea surface to 200-250 m.a.s.l. in which fog is rare, and an upper

horizon 1050-1100 m.a.s.l. above which marine-derived fog is rare. Values of ^{87}Sr/^{86}Sr contributed by a marine aerosol Sr source would be influenced by the evolution of seawater ^{87}Sr/^{86}Sr (section B5 in Appendix B), while factors that control the height of the fog band are mainly sea level (section B6 in Appendix B) and sea surface temperature (section B7 in Appendix B).

In order for the proposed ^{87}Sr/^{86}Sr paleo-altimetry method to serve as a proxy for geologically old forearc altitudes, gypsic soils must have developed on the landscape during the times of interest, and the paleo-desert system must have included an active fog system analogous to what exists today. The likelihood that a Gypsisol or gypsic relict soil sample formed within the paleo fog zone is calculated based on its Sr isotopic ratio and the distribution of Sr ratios of Holocene accumulations of salts in the landscape, corrected for temporal changes in the seawater Sr ratio. For a given paleosol with a ^{87}Sr/^{86}Sr value of x, and a given outside-of-the-fog Holocene salt accumulations' sample size n, the likelihood of this paleosol having formed inside of the paleo fog zone is 100*(p/n), where p is the number of outside-of-the-fog soil samples with ^{87}Sr/^{86}Sr lower than x [Chapter 2; Cosentino et al., 2015]. This way, we can infer whether a given soil has formed inside or outside of its contemporaneous paleo-fog zone. A comparison of the modern elevation of a sample site to its formation inside or outside the paleo-fog zone leaves several alternative interpretations of elevation change since the soil formed. Several examples are illustrative (Fig. 3-3). Ancient soil site #1 formed within the paleo-fog zone (i.e. has ^{87}Sr/^{86}Sr indicating a fog signal) and is now located above the corresponding age paleo-fog zone (Fig. 3-3a; Fig. 3-3b), which implies a minimum net surface uplift that equals the difference between the site's modern elevation and the top of its contemporaneous fog zone, and a maximum uplift corresponding to the difference between the bottom of the paleo-fog zone and the current elevation (Fig. 3-3c). Ancient soil site #2 formed above the

paleo-fog zone (i.e. has $^{87}Sr/^{86}Sr$ indicating no fog) and is now located within the Holocene fog zone, which implies a minimum net surface subsidence (Fig. 3-3c) that equals the difference between the top of the paleo-fog zone and the site's modern elevation. Yet the $^{87}Sr/^{86}Sr$ data would be the same if that soil had formed hundreds of meters higher than the top of the fog zone or had formed below the fog zone and been uplifted to its current site. Ancient soil site #3 formed above the paleo-fog zone at the same elevation and are now located above the Holocene fog zone, which implies a maxium permissible net surface uplift that equals the difference between the site's modern elevation and the top of the paleo-fog zone. For this case, alternative interpretations that there was no net surface elevation change, an undetermined net surface subsidence or uplift from below the paleo-fog zone are possible (Fig. 3-3c). To correctly choose among the alternative interpretations requires that the soil site and samples be placed in the context of other information.

Whereas most uplift studies have concentrated on the Precordillera and Altiplano plateau, fog has mostly occured farther west, in the Central Depression and Coastal Cordillera. Thus, it is our objective to complement previous studies to reach a more thorough understanding of the uplift history of the non-marine forearc of the South America - Nazca plate system in northern Chile.

3.3 Methods

3.3.1 Targeting locations to sample and sampling procedure

Targets for field sampling were locations with likely ancient gypsic soils at altitudes below 2000 m.a.s.l.. Relict gypsic soils were mapped using satellite images

(CNES/SPOT and Digital Globe data) displayed with Google Earth, following criteria given by Jordan et al. [2014] (Table B1 in Appendix B). Numerous sites were evaluated by field examination (five field campaigns for 2011-2013). Vertical profiles of soils were described by thickness of soil horizons, fracture properties, types and percentages of salts, and distribution and sizes of rock clasts. The stratigraphic identity of the soil parent material and of any overlying deposits were determined. At this stage of field sampling, samples of the soil mass were selected to be representative of the finer-than-1-cm fraction. During the first campaign, samples were obtained from two depths at the chosen soil sites. At later campaigns, we performed a denser vertical sampling of selected sites.

3.3.2 Laboratory analyses

Approximately 50 mg of the <5 mm grain-size fraction of each sample was crushed, weighed, mixed with 35 ml of ultra-pure water, placed in an ultrasonic bath (~50 ºC) for 8 hours, and centrifuged at 3,000 rpm for 15 minutes. This choice of solid sample:water ratio was found to be adequate to dissolve the complete soluble fraction of the samples.

The Ca^{2+}, Mg^{2+}, K^+, Na^+ and Sr^{2+} concentrations of the sample solutions were measured using an ICP-MS (Thermo Scientific Element 2, Cornell University) and an ICP-OES (Ameck SpectroBlue, Cornell University). SO_4^{2-}, Cl^-, F^- and NO_3^- concentrations were measured using ion chromatography (Dionex ICS 2000, Cornell University). Uncertainties on both measurements are less than 5%. Soil weight percent of each species was calculated based on the dissolved fraction of the soil aliquots and the fraction of the soil sample with grains less than 5 mm diameter.

For Sr isotopic analysis, all resulting solutions were passed through cation exchange columns, using *Eichrom Sr* as the ion-exchange resin, and using the methodology proposed by Horwitz et al. [1992]. $^{87}Sr/^{86}Sr$ was measured with either thermal ionization mass spectrometry (VG Sector 54, Cornell University) or inductively coupled plasma mass spectrometry (Neptune Multicollector ICP-MS, Rutgers University). Uncertainty on individual measurements range from 0.000003 to 0.000020 (± 2σ) [Cosentino et al., 2016a]. NBS-987 Sr standards run in association with samples averaged 0.71024 ± 0.00003 (2σ, n = 32) and 0.710282 ± 0.000012 (2σ, n = 18), respectively.

3.4 Results

Available chronological data either constrain the age of the parent material, thereby placing a maximum age on a specific soil, or the age of strata that overlie the soil, thereby placing a minimum age on the soil. A second category of chronological data uses the concentration of cosmogenic ^{3}He or ^{21}Ne of surface boulders as a proxy for the duration of exposure of the landscape surface on which the soil exists. For the Atacama Desert, these exposure ages are found to represent the approximate time of pavement abandonment [Evenstar et al., 2009]. For the current study, it is interpreted that the onset of soil accumulation started at or after the reported exposure age of a site. In the case of exposure ages cited in the following sections, the uncertainty we report is one based on intra-site age variability, or in the case of one sample, on independent estimates of cosmogenic nuclide inheritance (see Table B2 in Appendix B for further details).

Taken as a whole, the dataset of Gypsisol and gypsic relict soil samples in the study area have $^{87}Sr/^{86}Sr$ values between 0.70670 and 0.70864 (Fig. B9 in Appendix B; Table B3 in Appendix B). This Miocene – Pleistocene range is only slightly broader than the $^{87}Sr/^{86}Sr$ values of Holocene salt accumulations in the landscape, which vary between 0.70692 and 0.70841 (Fig. B9 in Appendix B).

In the following sections, we present the $^{87}Sr/^{86}Sr$ profiles for sampled relict soil profiles and Gypsisols (Table B3 in Appendix B). Suitable gypsic relict soils and Gypsisols with constrained ages mostly occur in the Central Depression, in six sub-regions described here. Three of the sub-regions occur on a single major piedmont slope (Aroma, Camarones and Tiliviche sites), of which the Aroma sub-region is described in the text and illustrated in Figure 3-3. Two of the three southern sub-regions also occur on a laterally continuous piedmont slope (Tambillo and Arcas sites); both sub-regions are described in the text and illustrated in Figure 3-4. Similar results for the other sub-regions are described and illustrated in the Appendix B, and in the references cited therein [Walfort et al., 1995; García & Herail, 2005; von Rotz et al., 2005; Blanco and Tomlinson, 2013; Kirk-Lawlor et al., 2013; Lehmann, 2013]. The few sites in the Coastal Cordillera that have adequate age constraints are then illustrated in Figure 3-6 and described. The chemistry of the soluble fraction for all these soils is reported in Table B4 in Appendix B.

3.4.1 Gypsic relict soils in and adjacent to the Aroma canyon

The Aroma canyon is a NE-trending valley incised 30 to 280 m into the Central Depression piedmont slope (Fig. 3-1; Fig. 3-4). Elevations of the main piedmont slope in this region of the valley range from 1350 to 1900 m.a.s.l.. A major terrace inset about 30% of the distance below the piedmont surface can be traced

within the canyon at least 12 km. The piedmont slope is developed on the alluvial gravels of the upper member of the El Diablo Formation. A conservative interpretation of the age of the parent material is Middle or Late Miocene [Muñoz & Sepúlveda, 1992; Farías et al., 2005b; von Rotz et al., 2005; Lehmann, 2013].

On the main piedmont slope surface within the area examined, exposure ages range from 7.1 ± 0.3 Ma in the southwest, to as old as 17 ± 5 Ma in the northeast [Evenstar et al., 2009] (Table B2 in Appendix B). Two sites in this study sample the major terrace inset into the piedmont slope in Aroma Canyon, with surface exposure ages of ~2.6 Ma and of 2.8 ± 0.2 Ma [Evenstar et al., 2009] (Table B2 in Appendix B).

The age of initiation of the multiple soils reported here has been deduced by combining Evenstar et al.'s [2009] surface exposure dates (Table B2 in Appendix B) with geomorphological information. An attribute of the piedmont slope surface that varies systematically is the spacing of small, incised channels that traverse the surface [García & Hérail, 2005]. Along ~20 km of the western Aroma Canyon rim, the density of incised channels varies at a spatial scale that has been mapped (Fig. 3-4). The least incised surfaces correspond to the sampled Aroma terrace, which yield the youngest exposure ages (~2.6 Ma and 2.8 ± 0.2 Ma). The surfaces with the highest incision densities have the oldest exposure ages (~10 Ma, 15 ± 1 Ma and 17 ± 5 Ma), although the wide range of exposure ages (10-22 Ma) must indicate inheritance as well as multiple episodes of surface erosion reactivation, and because some of these exposure ages are older than the well documented Middle to Upper Miocene age of the El Diablo Formation on which the analyzed materials are found. The correlation between the density of surface fluvial incisions and the surface exposure ages serves as the basis for assignment of an age of initiation of pedogenesis at each sampling site.

The relict soils capping the piedmont slope (NC11-24, NC11-28, NC11-29 and NC13-151) are developed over alluvial matrix-supported conglomerates with a coarse

sand matrix (Gm) (Fig. 3-4). The vertical transition from the undisturbed parent material to the pedogenized alluvial profile is gradational. The soil profiles have two distinct sections: a lower section is characterized by a well-cemented parent material with halite, gypsum and anhydrite comprising the cement (Bym), and an upper section of less indurated parent material in a matrix of gypsum and anhydrite (By). Vertical to sub-vertical cracks that vary in depth between 1–3 m affect mostly the upper layer. The cracks are filled with siliciclastic dust and sand interlayered in vertical bands with gypsum/anhydrite.

Site NC13-151 (1367 m.a.s.l.) samples a complete vertical profile on the youngest studied part of the piedmont slope, where the surface has been stable since about 7.1 ± 0.3 Ma. $^{87}Sr/^{86}Sr$ varies between 0.70676 and 0.70702, with a rising trend from deep to shallow in the upper meter of the soil profile (Fig. 3-4). $^{87}Sr/^{86}Sr$ values for soil profiles on the piedmont slope include values of 0.70701 and 0.70708 in slightly older sample NC11-29 (1477 m.a.s.l.; at depths of 1 cm and 150 cm, respectively). Samples NC11-24 (1882 m.a.s.l.) and NC11-28 (1636 m.a.s.l.) from parts of the landscape stable for times apparently in excess of ~10 Ma have $^{87}Sr/^{86}Sr$ spanning 0.70690 to 0.70707.

Gypsic relict soil site NC13-149 (1660 m.a.s.l.) caps the < 2.8 Ma Aroma Canyon terrace and is composed of a single By layer, ~3 m thick (Fig. 3-4). Some cobbles and boulders are fractured and gypsum/anhydrite fills the cracks. Vertical fractures affect the soil profile down to its base. Sample series NC13-149 displays $^{87}Sr/^{86}Sr$ variations that are smaller than the older relict soils on the piedmont: between 0.70684 and 0.70699, with decreasing values upward between 250–120 cm depths. Two higher samples reverse that trend, with a jump to higher values. Two samples at NC11-25, a position on the same terrace farther upstream, have $^{87}Sr/^{86}Sr$ values,

0.70710 and 070697, that are similar to the shallowest parts of the By layer at NC13-149.

3.4.2 Gypsic relict soils and Gypsisols adjacent to the Tambillo canyon and the Loma de Sal hills

The Tambillo canyon is incised across the eastern Central Depression piedmont slope by the ephemeral Tambillo stream, which also incised a narrow canyon across the Loma de Sal hills (Fig. 3-1; Fig. 3-5). Four complete soil profiles were sampled: three relict soils (NC13-137, 139 and 141) and one Gypsisol (NC13-143). Based on cross-cutting relationships between alluvial surfaces and their overlying soil profiles, as well as the arid-hyperarid chronology noted above [Jordan et al., 2014], the relict soils at sites NC13-141 and NC13-143 are assigned initiation ages of ~4.5 Ma, and relict soil profiles NC13-137 and 139 are assigned a pedogenic onset age of ~3.6 Ma.

Sampled on a ~4.5 Ma landscape surface, two main units can be defined for relict soil NC13-141 (1486 m.a.s.l.; Fig. 3-5). A lower Bym calcium sulfate-halite unit is well-cemented, and the percentage of clasts floating in the soil matrix decreases upward. Above a depth of 25 cm, an upper By unit is dominated by calcium sulfate and the clast to matrix ratio is even lower. Gypsisol NC13-143 (836 m.a.s.l.) is developed on the Quillagua Formation, whose top dates as ~4.5 Ma [Sáez et al., 2012] (Table B2 in Appendix B). The gypsic soil is overlain by 30 cm of horizontally layered tabular sand and gravel beds of latest Pleistocene age (10.1–12.6 kyr ^{14}C) [Nester, 2008; Gayo et al., 2012] (Fig. 3-5). This Gypsisol has one main discontinuity located 10 cm below the Gypsisol top. A lower Bym unit is 40 cm thick, well cemented and composed of both calcium sulfates and halite as important salt phases

constituting the displacive matrix. The upper unit, By, is not well consolidated and is composed predominantly of gypsum/anhydrite, containing very sparse sand clasts.

At NC13-141, absolute values of ^{87}Sr/^{86}Sr range between 0.70712 and 0.70732 (Fig. 3-5). The ^{87}Sr/^{86}Sr values define three sub-trends: in the lower soil unit the ^{87}Sr/^{86}Sr decreases slightly upward and then increases. In the upper unit the ratio rises slightly. Within the NC13-143 lower soil unit, the ^{87}Sr/^{86}Sr of the fine-grained soluble fraction of the soil shows a 5-point trend of upward decrease (Fig. 3-5), with a marked increase in the upper By level. Absolute values range between 0.70713-0.70732.

Relict gypsic soil NC13-139 (1480 m.a.s.l.) caps the north rim of the Tambillo Canyon, on a parent of latest Miocene-earliest Pliocene conglomerate. In its 80-cm-thick profile there is one principal physical discontinuity that separates horizons with differing degrees of cementation, Bym below and By above (Fig. 3-5). Relict soil NC13-137 (1046 m.a.s.l.) formed on a parent Pliocene fluvial conglomerate, is 90 cm thick and has very similar physical characteristics as NC13-139, except that halite is more important in its lower unit and that vertical fractures affect the whole profile (Fig. 3-5).

^{87}Sr/^{86}Sr values for NC13-139 decrease upward within the lower Bym soil unit (Fig. 3-5). This trend is reversed in the upper By unit. Absolute values range between 0.70731 and 0.70738. The pattern of upward change is similar for NC13-137 (Fig. 3-5), for which ^{87}Sr/^{86}Sr values are high at the bottom and top of the profile, while at intermediate depths values are lower and constant within error. Absolute values are lower than those of NC13-139, ranging between 0.70712 and 0.70717.

3.4.3 Gypsic relict soils of the Arcas fan

The Arcas fan (Fig. 3-1; Fig. B4 in Appendix B) is the region of our southernmost data. Over a small central section of the Arcas fan, gypsic relict soils cap the alluvial depositional surfaces. The distal deposits of the Arcas fan interfinger with lacustrine and fluvial deposits represented by the Quillagua Formation, spanning 5.5-4.5 Ma [Sáez et al., 2012]. The distal Arcas fan deposits also interfinger with the salar-facies Soledad Formation [Jordan et al., 2014], with interbedded tephra dated as 4.3 ± 0.2 Ma and 3.73 ± 0.02 Ma [Quezada et al., 2013]. These relations bracket the parent gravels on which relict gypsic soils occur to roughly 5.5-4.3 Ma [Jordan et al., 2014].

Gypsic relict soil NC13-136 (1299 m.a.s.l.), developed over a horizontally-laminated sandstone and conglomerate, is 65 cm thick (Fig. B8 in Appendix B). The pedogenic profile is composed of three units. The lower Bym unit, at a depth of 50-65 cm, is well cemented and composed of coarse sand to cobble clasts dispersed within a calcium sulfate/halite matrix. The intermediate By layer is less well cemented and poorer in calcium sulfate. The topmost By soil horizon is similar to the middle By horizon, but with a lower clast/matrix ratio. Within the top 50 cm of the relict soil, the $^{87}Sr/^{86}Sr$ values rise steadily, from 0.70699 to 0.70723 (Fig. B8 in Appendix B).

3.4.4 Gypsic relict soils and Gypsisols in the Coastal Cordillera and Coastal Escarpment

Gypsisols and gypsic relict soils were sampled over a region of the Coastal Cordillera approximately 100 km in length latitudinally (Fig. 3-1; Fig. 3-6). Samples were obtained at one or two depths within the Gypsisol or gypsic relict soil profiles. All $^{87}Sr/^{86}Sr$ values for these samples range between 0.70777 and 0.70864.

Site TJ12-115 (954 m.a.s.l.) is located in the eastern Coastal Cordillera and consists of a gypsic relict soil within a paleochannel whose latest reactivation was

dated at 3.98 Ma using cosmogenic ^{21}Ne [Carrizo et al., 2008]. Thus, this soil can be considered younger than ~4 Ma. ^{87}Sr/^{86}Sr values at the two depths sampled are almost identical, 0.70777 (6 cm) and 0.70778 (33 cm). Two other sites sampled in the eastern Coastal Cordillera, NC11-40 and TJ12-100, can only be constrained to have formed during the Neogene.

The remaining soils were sampled in proximity to the western margin of the Coastal Cordillera. The southernmost site, TJ12-117 (741 m.a.s.l.), consists of a gypsic relict soil developed over a parent of conglomerate and sandstone that may be correlated to the Gravas de Alto Hospicio Formation, defined for similar units to the north [Marquardt et al., 2008; Blanco et al., 2012]. A ^{40}Ar/^{39}Ar age on an ash level within what is interpreted to be the same sedimentary unit, but ~17 km NNW of this site, yields 3.99 ± 0.06 Ma [Baker, 2012]. Thus, we consider this relict soil to be younger than 4 Ma. Two depths were sampled: one at 5 cm (TJ12-117a) and another one at 13 cm (TJ12-117b). The ^{87}Sr/^{86}Sr ratios are notably higher than values recorded in the Central Depression and the eastern fringe of the Coastal Cordillera, 0.70864 for the shallow sample and 0.70862 for the deeper sample.

The northernmost Coastal Cordillera gypsic relict soil sampled, NC12-80 (1148 m.a.s.l.), formed on a parent of ignimbrite that is interlayed within the Gravas de Alto Hospicio. An ash layer that outcrops 500 m from this location, and that we assign to the same ignimbrite unit, has been dated by ^{40}Ar/^{39}Ar as 7.86 Ma (± 0.10 Ma) [Vásquez & Sepúlveda, 2013] (Table B2 in Appendix B). Thus, the gypsic relict soil is younger than ~7.9 Ma. A single sample from 12 cm below the relict soil top has a Sr isotopic ratio of 0.70848.

Site NC11-46 (506 m.a.s.l.) is a 1.1-m-thick Gypsisol located on the Coastal Escarpment. It is younger than an underlying tuff dated as 4.2 ± 0.4 Ma [Blanco et al., 2012]. The sample was taken from the upper 10 cm. Sample NC12-84, an ~1 m thick

Gypsisol, also is exposed on the Coastal Escarpment, interbedded in Gravas de Alto Hospicio. About 10 km inland, a third Gypsisol within that same formation, only about 25 cm thick, provided sample NC12-82, which is younger than a 8.52 ± 0.11 ash layer [Vásquez & Sepúlveda, 2013] located close by. Their Sr isotopic ratios of 0.70853, 0.70815 and 0.70794, respectively, are all high relative to most samples from the Central Depression.

3.5 Discussion

3.5.1 Land-ocean-atmosphere changes affecting pedogenic sulfate $^{87}Sr/^{86}Sr$

To isolate the role of continental forearc elevation change as the factor potentially forcing change through time in pedogenic calcium sulfate $^{87}Sr/^{86}Sr$, the history of other factors that influence the delivery of a marine $^{87}Sr/^{86}Sr$ signal to the pedogenic system must be collected in a single evolutionary model. Corrections have been applied to account for some of the factors that influence this parameter and that were dynamic over the time span of interest, while assumptions have been made on those factors for which we cannot obtain appropriate corrections. These factors, both corrected and uncorrected for, include: (a) changes in seawater $^{87}Sr/^{86}Sr$ during the Neogene that affect fog $^{87}Sr/^{86}Sr$, (b) changes in the top and bottom of the intersection of the fog zone with the continental landscape due to eustatic changes in sea-level during the Neogene, and (c) changes in the top of the fog zone due to changes in the ocean/atmosphere climate during the Neogene that affect the height of the atmospheric inversion layer.

The composite model (Fig. 3-7) combines corrections for the influence on fog vertical structure due to (i) eustatic sea level changes, and (ii) regional sea surface temperature changes. Other factors, namely changes in atmospheric subsidence and cloud feedbacks, are assumed negligible in terms of their influence on paleo-fog zone top and bottom heights. The corrected paleo-fog zone top altitude varied up to 18% with respect to the Holocene-averaged fog zone top. The corresponding calculated paleo-altitudes of the fog top are between 880 and 1090 m above modern sea level versus the modern value of 1050-1100 m.a.s.l.. The most important factor contributing to this change is SST variability and its effect on the inversion layer base height. Detailed information on the methodology used to derive the temporal evolution of the fog zone elevation can be found in Appendix B (sections B1, B5-B8 and Table B5) and in the references cited therein [Veizer, 1989; Veizer et al., 1999; Hashizume et al., 2002; Mix et al., 2003; Wang et al., 2004; Dekens et al., 2007; Miller et al., 2011; Zhang et al., 2011].

The Coastal Cordillera may act as a barrier to fog advecting from the Pacific Ocean, preventing fog to reach landscape positions even at low-enough elevations. Thus, a detailed analysis of fog corridors across the Coastal Cordillera and their evolution in time is warranted (section B9 in Appendix B). For most of the study area, such fog corridors have likely existed since the the earliest Pliocene.

3.5.2 Mineralogy of salt phases

The majority of sampled Gypsisol and gypsic relict soil profiles show a soluble chemistry dominated by equimolar Ca^{2+} and SO_4^{2-}, while Na^+ and Cl^- are present in relevant quantities in some samples. This is consistent with previous studies of ancient

soils of the Atacama Desert [e.g. Ericksen, 1983; Rech et al., 2003; Ewing et al., 2006; 2008].

The Sr molar concentration curve mimics the general depth trend of both Ca^{2+} and SO_4^{2-} in most gypsic relict soil profiles (Fig. 3-4; Fig. 3-5; Fig. B6-B8 in Appendix B). This can be interpreted to reflect that most soluble Sr in Atacama soils substitutes for Ca in calcium sulfate mineral phases.

3.5.3 On the impact of Sr vertical mixing on soil $^{87}Sr/^{86}Sr$ and chronology

Soil stratification may either be conceptualized as a layer-like accumulation mechanism, which implies a restricted amount of vertical mixing as climate changes, or as a process that also includes stratification of salts by solubility, which implies varying degrees of vertical mixing due to climate change. While both processes are acknowledged to operate in gypsic soil formation in the Atacama Desert [Ericksen, 1981; 1983; Ewing et al. 2006], the distinction between these two explanations of gypsic soil vertical trends has an important impact on the interpretation of the $^{87}Sr/^{86}Sr$ vertical trends. Wang et al. [2015] use the vertical profile of a meteoric constituent, beryllium-10, in a relict gypsic soil in the Atacama Desert to demonstrate that the initial stratification of soil mass that had been contributed to the top surface from the atmosphere is largely retained. Nevertheless, post-depositional vertical mixing processes may potentially obscure the primary source signal of $^{87}Sr/^{86}Sr$ in the Gypsisols and gypsic relict soils of the Atacama Desert. Therefore, a more in-depth look into the pedogenic mixing processes is warranted.

Ewing et al. [2008] measured Ca concentration in a ~140 cm-thick, 2 myr-old gypsic relict soil located in the Coastal Cordillera (24.1ºS; 1022 m.a.s.l.). The vertical Ca concentration trend could be reproduced by modeling Ca downward transport

during small, infrequent and regularly recurring rainfall events [Ewing et al., 2008] (Fig. 3-8b). The simulation shows that a youthful gypsic soil profile contains a maximum Ca concentration at a depth of a few centimeters, with a steady decline to near zero concentration at 20 cm depth (Fig. 3-8b). After the cycles of precipitation have persisted for 2 million years, a high and steady value of Ca spans from ~10 cm to ~50 cm depth, declining to a low but non-zero value by 80 cm depth (Fig. 3-8b). These results show that in some cases, vertical transport of Ca can explain Ca concentration trends in gypsic relict soils.

Ewing et al.'s [2008] model results (Fig. 3-8b) may not be fully applicable to the interpretation of the Ca concentration profiles presented in this study for two main reasons. Model simulations (a) were run for a 2 myr period, and (b) assume a constant Ca atmospheric flux (1 mmol m^{-2} y^{-1}) and a constant rainfall regime (one 1 cm event every 10 years plus five 10 cm events every 100 years) through that time period. In contrast, some of our gypsic relict soils initiated salt accumulation at 4–5 Ma, and since that time some of them have gone through arid-hyperarid cycles. Nevertheless, we will use the vertical patterns of concentration that result from Ewing et al.'s (2008) model as a first-order guide to identify Ca vertical mixing in the vertical profiles of salts (Fig. 3-4; Fig. 3-5; Fig. B6-B8 in Appendix B) and of $^{87}Sr/^{86}Sr$ presented here (Fig. 3-8a).

Given that $SrSO_4$ is more soluble than $CaSO_4$ (3.96 g/100 g water versus 0.205 g/100 g water, respectively), downward migration of $SrSO_4$ is favored over $CaSO_4$. Therefore, Ca/Sr is a proxy for post-depositional downward transport of Sr with respect to Ca. A hypothetical gypsic relict soil that has accumulated during a prolonged period of time at elevations low enough to receive marine-derived aerosols and then suffered uplift to elevations above the paleo-fog zone would show an abrupt break in $^{87}Sr/^{86}Sr$ values from low to high values down-profile (Fig. 3-8c). If this

hypothetical gypsic soil were later subjected to less arid conditions under which more salts dissolved and some Sr with low $^{87}Sr/^{86}Sr$ values migrated down-profile, the Sr with high $^{87}Sr/^{86}Sr$ values of the lower soil horizons would be partially masked (Fig. 3-8c). However, Ca/Sr is also a proxy for Ca source. Marine biogenic mineral precipitation at low temperature produce high molar Ca/Sr of 1000-3000 [e.g. Rosenthal et al., 2006], consistent with > 900 Ca/Sr ratios for airborne particles near the coast [Ewing et al., 2008]. Instead, in-land particles had <600 Ca/Sr ratios [Ewing et al., 2008]. Thus, only a case-by-case analysis of Ca concentration, Ca/Sr and $^{87}Sr/^{86}Sr$ vertical profiles may illuminate the extent of Sr vertical mixing in soils and its impact on paleoaltimetry interpretations.

Once we identify the degree of Sr vertical migration, we infer which model of soil accumulation in terms of Sr is more appropriate, for the sub-regions of the Aroma canyon and Tambillo-Loma de Sal, where there are multiple densely sampled vertical profiles. For cases of restricted Sr vertical mixing, we may be able to go beyond inferring the age of onset of soil accumulation and infer as well internal soil chronologies in terms of Sr to some degree.

3.5.3.1 Extent of Sr vertical mixing in Aroma canyon sites

When compared to Ca transport models in soils (Fig. 3-8b), the lower 175 cm of relict soil profile NC13-149 shows a Ca concentration trend that may be explained by vertical mixing, with peak Ca at 125-210 cm (Fig. 3-4). Ca/Sr ratios peak at higher than 900 at 215-245 cm, and are lower than 600 elsewhere, except 803 at the topmost sample (Fig. 3-4). This is consistent with either a marine source for Ca at 215-245 cm depth, or with Sr downward mobilization with respect to Ca from 215-245 cm depth. Given the lower than 0.70700 Sr ratios at all depths (0-7% likelihood of being formed

in the paleo-fog zone; Fig. 3-8a; Table B3 in Appendix B), we discard an unmixed marine source for Ca anywhere in the profile. Instead, the data are consistent with joint Ca and Sr downward migration from shallow depths to 125-210 cm, and further Sr downward migration with respect to Ca from 215-245 cm.

Shallow $^{87}Sr/^{86}Sr$ at 20-40 cm is ~ 0.70697, while $^{87}Sr/^{86}Sr$ at the deepest sample is 0.70690. In this study, the lowest $^{87}Sr/^{86}Sr$ samples with fog signals lie at 0.70760 (80% likelihood of being formed in the paleo-fog zone; Table B3 in Appendix B). Thus, not even a complete overprint of deep soil $^{87}Sr/^{86}Sr$ by shallow Sr ratios may explain masking of a deep fog signal. Thus, we interpret that despite partial Sr vertical mixing, site NC13-149 has not accumulated at any time within the paleo-fog zone.

The gypsic relict soil at NC13-151 has a pattern of Ca concentrations that does not suggest Ca downward migration below 20 cm depth (compare Fig. 3-8b and Fig. 3-4). Ca/Sr ratios are < 700, which are consistent with non-marine Ca sources. Only a small amount of Sr downward migration with respect to Ca from a source zone at 20-40 cm depth may have occurred. Given the low $^{87}Sr/^{86}Sr$ all along the profile (Fig. 3-8a), particularly the fact that deep Sr ratios are lower than the shallow ones, no masking of a hypothetical deep fog signal is deemed possible. We conclude that the lower than 0.70705 Sr ratios (0-7% likelihood of a fog signal; Table B3 in Appendix B) along the profile are largely indicative of primary sources. Thus, site NC13-151 has not accumulated at any time within the paleo-fog zone.

Gypsic relict soil profile NC13-151 caps the regional piedmont slope into which the Aroma canyon is incised, with no local exposure ages (Fig. 3-4). Given (i) the general trend of surface exposure ages for the Aroma study area piedmont slope from younger in the southwest to older in the northeast based on the ^{3}He exposure ages of Evenstar et al. [2009], (ii) the lower density of incised small-scale channels on

the surface around NC13-151 compared to surfaces to the northeast and (iii) exposure ages of 1.3 ± 0.1 Ma farther southwest of site NC13-151 [Evenstar et al., 2009] (Table B2 in Appendix B), gypsic relict soil NC13-151 can be assumed to have started accumulation after 7.1 ± 0.3 Ma and before 1.3 ± 0.1 Ma. Similarities in the physical characteristics between the upper By unit in profile NC13-151 and the entirety of younger soil profile NC13-149 (salt composition, induration and extent of vertical cracks), as well as the similarities of the ranges of $^{87}Sr/^{86}Sr$ values between those two soil profiles, point to a probable correlation between NC13-151 By and the full profile at NC13-149 (Fig. 3-4; Fig. 3-8a).

3.5.3.2 Extent of Sr vertical mixing in Tambillo canyon and Loma de Sal sites

When compared to Ca transport models in soils (Fig. 3-8b), the upper 25 cm of Gypsisol NC13-143 shows a Ca concentration trend that may be explained by downward transport, with peak Ca at 10-25 cm (Fig. 3-5). Sr mimics Ca (Fig. 3-5). Ca/Sr ratios are < 200 at all depths, peaking at ~180 at 35 cm and with its lowest value at ~50 cm (Fig. 3-5). $^{87}Sr/^{86}Sr$ ratios are < 0.70735 at all depths (7-33% likelihood of being formed in the paleo-fog zone; Table B3 in Appendix B), peaking at 0.70732 at the shallowest sample at 4 cm and with a value of 0.70729 for the deepest sample (Fig. 3-5; Fig. 3-8a). We interpret these data to reflect joint Ca and Sr downward migration in the upper 25 cm, and possible further Sr migration to ~ 50 cm depth. However, there is no evidence of an unmixed marine source for Sr all along the profile. Based on the absolute values of $^{87}Sr/^{86}Sr$, we discard masking of a deep fog signal within the soil by downward migration of a shallow non-fog signal. This soil has thus not formed within the paleo-fog zone since the onset of accumulation. However, the location of this site at 836 m.a.s.l. within the Holocene fog zone leads to the expectation that it

should show high shallow Sr ratios. Despite a sharp rise in $^{87}Sr/^{86}Sr$ toward the top of the profile, there is a lack of a fog signal even in the upper section of the soil. The most straightforward explanation is that this site was incorporated into the fog zone after the end of soil accumulation and during deposition of the Pleistocene sands and gravels.

In the case of gypsic relict soil NC13-137, Ca and Sr versus depth points to downward migration of Ca and Sr in the upper 40 cm (compare Fig. 3-5 and Fig. 3-8b). Ca/Sr ratios are < 210 at all depths (Fig. 3-5), while $^{87}Sr/^{86}Sr$ ratios are < 0.70720 at all depths (7% likelihood of being formed in the paleo-fog zone; Table B3 in Appendix B), peaking at 0.70716-0.70717 at the shallowest (10 cm) and deepest (86 cm) samples (Fig. 3-5; Fig. 3-8a). We interpret these data to reflect joint Ca and Sr downward migration in the upper 40 cm. However, there is no evidence of an unmixed marine source for Sr. Also, based on the absolute values of $^{87}Sr/^{86}Sr$, we discard masking of a deep fog signal within the soil by downward migration of a shallow non-fog signal. Thus, this soil has accumulated outside of the paleo-fog zone. However, given its current position within the Holocene fog zone, one might expect shallow high values for $^{87}Sr/^{86}Sr$. The fact that we do not see high values is probably due to insufficient shallow sampling (shallowest sample at 9.5 cm depth) or to termination of gypsic soil accumulation prior to a relative change in the site elevation to the fog-top altitude.

Ca and Sr vertical concentration trends in site NC13-139 point to joint downward migration of Ca and Sr in the upper 30 cm (compare Fig. 3-5 and Fig. 3-8b). Ca/Sr ratios are < 350 at all depths (Fig. 3-5), while $^{87}Sr/^{86}Sr$ ratios are < 0.70740 at all depths (27-40% likelihood of being formed in the paleo-fog zone; Table B3 in Appendix B), peaking at 0.70738 at the deepest sample (70 cm), with 0.70736 for the shallowest one (4 cm) (Fig. 3-5; Fig. 3-8a). There is no evidence of an unmixed

marine source for Sr. Also, based on the absolute values of $^{87}Sr/^{86}Sr$, we discard masking of a deep fog signal within the soil by downward migration of a shallow non-fog signal. Thus, this soil has accumulated since the onset of formation outside of the paleo-fog zone.

In the case of gypsic relict soil NC13-141, the vertical variation of Ca concentration points to no downward migration of Ca deeper than 15 cm (compare Fig. 3-5 and Fig. 3-8b). Ca/Sr ratios are < 200 at all depths, except at the shallowest sample (1070 at 7 cm depth) (Fig. 3-5), while $^{87}Sr/^{86}Sr$ ratios are < 0.70735 at all depths (7-33% likelihood of being formed in the paleo-fog zone; Table B3 in Appendix B), peaking at 0.70732 at the shallowest sample (7 cm), and with its lowest value at the deepest sample (0.70712 at 53 cm; Fig. 3-5; Fig. 3-8a). We interpret this data to be consistent with downward migration of Sr from the shallowest 10 cm. Also, based on the absolute values of $^{87}Sr/^{86}Sr$, we discard masking of a deep fog signal within the soil by downward migration of a shallow non-fog signal. Thus, this soil has accumulated since the onset of formation outside of the paleo-fog zone.

Gypsic relict soil profiles NC13-137 and 139 started accumulation during hyperarid phase NIIIb, starting at ~ 3.6 Ma (Fig. 3-5). Arguably, for both soils the boundary between the Bym and By horizons may be associated to the less arid stage NIVa (2.6-2.2 Ma). However, given Sr downward migration within the upper 30-40 cm, the age of Sr in salts accumulated at positions directly above the Bym-By boundary is probably younger than 2.2 Ma: the time when soil accumulation resumed after stage NIVa. Gypsic relict soil profile NC13-141 and Gypsisol NC13-143 started accumulation during hyperarid phase NIIb at 4.5 Ma (Fig. 3-5). It may again be argued that the boundary between the Bym and By horizon represents the less arid stage NIIIa (4-3.6 Ma), during which net soil accumulation was interrupted. However, given Sr vertical migration within the upper 15-25 cm, the age of Sr in salts accumulated at

positions directly above the Bym-By boundary is probably younger than 3.6 Ma: the time when soil accumulation resumed after stage NIIIa.

3.5.3.3 Extent of Sr vertical mixing in Arcas fan sites

The gypsic relict soil at NC13-136 has a pattern of Ca concentrations that does not suggest Ca downward migration below 10 cm depth (compare Fig. 3-8b and Fig. B8 in Appendix B). Ca/Sr ratios are < 520 (Fig. B8 in Appendix B), which are consistent with non-marine Ca sources. Only a small amount of Sr downward migration with respect to Ca from a source zone at 25-35 cm depth is possible. Given the low $^{87}Sr/^{86}Sr$ all along the profile (Fig. 3-8a; Fig. B8 in Appendix B), particularly the fact that deep Sr ratios are lower than the shallow ones, no masking of a hypothetical deep fog signal is deemed possible. We conclude that the lower than 0.70725 Sr ratios (0-27% likelihood of a fog signal; Table B3 in Appendix B) along the profile are largely indicative of primary sources. Thus, site NC13-136 has not accumulated at any time within the paleo-fog zone.

3.5.3.4 Collective examination of Sr vertical mixing evidence and $^{87}Sr/^{86}Sr$ variability interpretation

Examined collectively, information on $^{87}Sr/^{86}Sr$ (Fig. 3-8a), Ca concentration and Ca/Sr (Fig. 3-4; Fig. 3-5; Fig. B6-B8 in Appendix B) variations with depth in the nine vertical soil profiles likely reflect vertical migration of salts. Yet the evidence is insufficient to conclude that these processes operating alone in a steady-state system can explain the vertical stratification at the scale of the major divisions of salt composition and consolidation, such as between Bym and By horizons of the Tambillo

soils. The profiles of the seven sites for which the $^{87}Sr/^{86}Sr$ ratio is much lower than that of Holocene fog-fed gypsic soils (Fig. 3-8a) typically show an elevated $^{87}Sr/^{86}Sr$ value near the surface, a decrease in $^{87}Sr/^{86}Sr$ with increasing depth to 10–120 cm below the surface, and below that depth there is a progressive increase. Even though an increase in $^{87}Sr/^{86}Sr$ deep in the profiles is the direction of change that was hypothesized to be the pattern if elevation of the site increased by ~1000 m (Fig. 3-8c), all the values in the seven profiles remain markedly below the value expected for fog-fed gypsic soil. Two other profiles have values of $^{87}Sr/^{86}Sr$ consistently above 0.7078, NC13-146 and NC13-144. Even though their origin does not fit the spatial distribution that we expected (detailed in section 4.4.6), the $^{87}Sr/^{86}Sr$ values and extent of variations in their vertical profiles reinforce the interpretation that fog-fed soil salts like these were not present in the lower parts of the other seven profiles. The recurring pattern of decrease followed by increase of $^{87}Sr/^{86}Sr$ with depth must rest in unknown historical changes in the environment, such as atmospheric contributions, because even downward migration of Sr would not change the ratio unless the $^{87}Sr/^{86}Sr$ composition were stratified to begin with.

3.5.4 Application of the paleoaltimeter to soil results

The following sections include the paleoaltimetric interpretations obtained for the areas discussed previously. For the rest of the areas analyzed within the study area see Appendix B and references cited therein [Nester and Jordan, 2011; García and Fuentes, 2012; Blanco and Tomlinson, 2013; Chapter 2, i.e. Cosentino et al., 2015].

3.5.4.1 Aroma canyon paleoaltitudinal constraints

Samples located within the western section of the studied Aroma Canyon area (NC11-29a,b, NC13-151a-g) are located today at altitudes of 1367 and 1477 m.a.s.l., above both the modern (1050-1100 m.a.m.s.l.) and the contemporaneous paleo-fog zone regional tops (~900-1100 m.a.m.s.l.) (Fig. 3-4). All the Sr ratios in the profile indicate soil formation either below or above the contemporaneous fog zone (e.g., Fig. 3-3 sites #3). A vertical profile through the By unit in NC13-151 has been sampled every 13-15 cm. Based on a layer-like accumulation mechanism, Wang et al. [2015] estimated a soil accumulation rate of 3.43×10^{-5} cm yr^{-1} for a similar site at 1500 m.a.s.l. and at a similar distance from the coast, ~340 km to the south. Based on this accumulation rate and site NC13-151's By unit vertical sampling resolution, we estimate at ~0.4 myr the time resolution of the samples in this soil By unit. In a scenario of uplift from below the paleo-fog zone bottom (~50-200 m.a.m.s.l.) since < 2.8 ± 0.2 Ma, an uplift rate in excess of 2900 m myr^{-1} is required for a fog signal not to be registered along profile NC13-151, which is ~3 to ~29 times higher than independently obtained uplift rates elsewhere in the forearc or in the Altiplano Plateau (~100 m myr^{-1} for Hoke et al., [2007]; < 550 m myr^{-1} for Regard et al., [2010]; < 875 m myr^{-1} for Kar et al., [2016]). It thus seems unlikely that this area was lower in altitude than the paleo-fog zone bottom. Also, samples NC13-151f,g clarify an earlier history of this site: between < 7.1 ± 0.3 Ma and < 2.8 ± 0.2 Ma this site also remained outside of the paleo-fog zone. Over that time span, the height range of paleo-fog zone might have been between ~200-250 and ~1050-1100 m.a.m.s.l. (Fig. 3-7). The preferred paleoaltimetric interpretation is that the location of relict soil NC13-151 has remained above the paleo-fog zone since < 2.8 ± 0.2 Ma, and probably since < 7.1 ± 0.3 Ma. This is consistent with a maximum permissible net surface uplift of ~450 m since < 3 Ma (Table 3-1; Fig. 3-3c; Fig. 3-9a).

Samples located within the eastern section of the studied Aroma Canyon area (NC11-24a, NC11-25b,c, NC11-28a,b and NC13-149a,b,d-h) are located today at altitudes between 1636 and 1882 m.a.s.l., above the modern fog zone regional top (1050-1100 m.a.s.l.). The current site locations are also above the paleo-fog zone regional top for all times represented by these samples (~900-1100 m.a.m.s.l.). It is highly unlikely that this area as well was lower in altitude than the paleo-fog zone bottom (50-200 m.a.m.s.l.) since < 2.8 ± 0.2 Ma. Samples NC11-28a & b and NC11-24a occur on older landscape surfaces, potentially as old as ~10 Ma, the approximate end of deposition of the Middle to Upper Miocene El Diabo Formation. The preferred interpretation is that this area has remained above the paleo-fog zone since < 2.8 ± 0.2 Ma, and arguably since ~10 Ma. This is consistent with a maximum permissible net surface uplift of ~750 m since < 3 Ma (Table 3-1; Fig. 3-9a). Under the assumption of whole-block surface elevation evolution for both eastern and western groups of sites along the Aroma Canyon, we infer a maximum permissible net surface uplift of ~450 m since < 3 Ma (Table 3-1; Fig. 3-9a).

3.5.4.2 Tambillo valley and Loma de Sal paleoaltitudinal constraints

The Central Depression axis and eastern flank near 21.5°S is formed by the upper surface of relict Pliocene alluvial fans and lake beds that are interrupted by two structural features that deform Miocene strata. A fault is located east of the sample sites for ancient soils, and is not considered further. An anticline bounded on the west and north by faults forms Loma de Sal hills [Jordan et al., 2015] which display about 100 m differential uplift relative to the valleys surrounding the anticline on all sides. Consequently, the $^{87}Sr/^{86}Sr$ paleoaltimetric signal of locations within this area will be

dominated by the elevation history of the whole block, with a possible local overprint on and immediately adjacent to Loma de Sal.

Gypsisol site NC13-143 is the lowest elevation sampled soil in the area, and it is located about 3 km west of the Loma de Sal hills (Fig. 3-5). The modern elevation of this site, 836 m.a.s.l., rests within the modern regional fog zone, the 4.5-4 Ma paleo-fog zone (~200-1050 m.a.m.s.l.) and < 3.6 Ma (~50-250 to 900-1100 m.a.m.s.l.) paleo-fog zone (Fig. 3-7). Nevertheless, the gypsic soil data reveal that it is likely that this site has remained outside of the paleo-fog zone since ~ 4.5 Ma (Fig. 3-3c, case #2). Based on the average sample spacing and the salt accumulation rate from Wang et al. [2015] we obtain a time resolution for this site of 0.32 myr. The scenario of uplift from ~200 m.a.m.s.l. to 836 m.a.s.l. between any two samples in the profile implies rates in excess of 1900 m myr^{-1}, which are again much higher than uplift rates reported elsewhere in the forearc and Altiplano plateau [Hoke et al., 2007; Regard et al., 2010; Kar et al., 2016]. We thus rule out the scenario of uplift from below the paleo-fog zone. The alternative interpretation is that the gypsic soil formed above the contemporaneous fog zone, which implies that there has been a minimum net surface subsidence of 50 m since ~ 4.5 Ma (Table 3-1; Fig. 3-9b).

East of Loma de Sal and in the western area of Tambillo Canyon, gypsic relict soil sites NC13-137 and NC12-60 are located at intermediate modern elevations: 1046 m.a.s.l. and 1167 m.a.s.l., respectively. Site NC13-137 is located within the upper limits of the modern fog zone, and had there been no change in the continental surface elevation through time, this location would have been within or slightly above the paleo-fog zone much of the time since its onset of accumulation at ~3.6 Ma (Fig. 3-7). However, its Sr isotopic composition implies a 7% probability of having been formed within the paleo-fog zone. Single-depth sample NC12-60a is younger than 4.5 Ma and was obtained at a site located at a modern elevation of 1167 m.a.s.l.. It has a 27%

probability of having been formed within its contemporaneous paleo-fog zone. These results show that it is highly unlikely that this pair of sites has been within the paleo-fog zone since 3.6 Ma (Fig. 3-7), and probably since sometime between 4.5 and 3.6 Ma. Given that there is no fog signal at any depth along the NC13-137 soil profile (Table B3 in Appendix B; Fig. 3-5), analogous to the Aroma region we rule out the scenario of surface uplift from below the paleo-fog zone. Instead, we interpret that there has been no net surface elevation change or an undetermined amount of subsidence since ~3.6 Ma (Table 3-1; Fig. 3-9b).

In the eastern sector of the studied Tambillo canyon area, gypsic relict soil sites NC13-139 and NC13-141 are located at higher modern elevations: 1480-1486 m.a.s.l.. These are all located above both the modern fog zone and the paleo-fog zones contemporaneous with their formation: ~50-250 to 900-1100 m.a.m.s.l. (Fig. 3-7). Their likelihood of having been formed within the paleo-fog zone ranges from 7% to 40% (Table B3 in Appendix B). Given that there is no fog signal at any sampled depths along both soil profiles, the maximum permissible uplift scenario (Fig. 3-3c, case #3) that is consistent with the data is that there may have been a net surface uplift of no more than ~600 m, from 900 m.a.m.s.l. to 1480 m.a.s.l., in the area since ~4.5 Ma (Table 3-1; Fig. 3-9b).

Considering these different scenarios of surface elevation change for the three groups of sites which are embedded in a single geomorphic surface, the only interpretation that is consistent with a whole-block surface elevation change history is one of a minimum net surface subsidence of ~50 m since ~4.5 Ma. However, based on independent information of the structural setting and the history of facies changes in the area, we cannot rule out the possibility that local subsidence along the western flank of the Loma de Sal anticline might explain the result at NC13-143 [Jordan et al., 2015]. If so, the two sites east of the anticline can be explained by a maximum

permissible net uplift of ~150 m since ~3.6 Ma and of ~600 m since ~4.3 Ma (Table 3-1; Fig. 3-9b). The full set of Tambillo – Lomas de Sal data is also consistent with tilt toward the west of a ~40 km wide crustal block. That scenario would couple subsidence of the western sites (NC13-137, NC13-143) to uplift or stability of the eastern sites (NC12-60a, NC13-139 and NC13-141).

3.5.4.3 Arcas fan paleoaltitudinal constraints

No faults or folds that impact the Arcas alluvial fan could be mapped. Hence any changes in paleoaltitude would relate to the broad Central Depression structural block.

Gypsic relict soil sites TJ12-111 and NC13-136 are Pliocene to recent in age and are located on the central-north section of the Arcas fan, at an altitude of 1270-1299 m.a.s.l.. These sites are above both the modern and paleo-fog zone regional tops (1050-1100 and ~900-1100 m.a.m.s.l., respectively) (Fig. 3-3c, case #3). None of the samples at these sites has a fog signal at any depth (Table B3 in Appendix B), so as described for previous sub-regions it is highly unlikely that this area was lower in altitude than the paleo-fog zone bottom (~50-250 m.a.m.s.l.) since ~4.3 Ma. Instead, the preferred interpretation is that this area has remained above ~900-1100 m.a.m.s.l. since ~4.3 Ma. This is consistent with a maximum permissible net surface uplift of ~400 m since ~4.3 Ma (Table 3-1; Fig. 3-9c).

Gypsic relict soil site TJ12-109 is Pliocene to recent in age and is located within the distal section of the Arcas fan, at an altitude of 988 m.a.s.l.. This site is ~100 m below the modern fog zone regional top (1050-1100 m.a.m.s.l.) and within the error of the paleo-fog zone (top at ~900-1100 m.a.m.s.l.). The fact that the two samples collected at this site have no fog signal (Table B3 in Appendix B), and in

view of the uncertainty of the paleo-fog zone top height, implies a maximum

permissible net surface uplift of ~100 m since < 5.5 Ma (Table 3-1; Fig. 3-9c). This

interpretation includes the scenarios of no net surface elevation change or of an

undetermined amount of net surface subsidence (Fig. 3-3c, case #3). This site is

located within the Holocene fog zone and thus the shallowest salts in the relict soil

should have a fog signal. However, the shallowest sample obtained in this profile (3

cm from surface) does not capture such a signal.

Assuming whole-block surface elevation change across the Arcas fan, a

maximum net surface uplift of ~100 m since < 5.5 Ma is allowed by the data (Table 3-

1; Fig. 3-9c).

3.5.4.4 Western Coastal Cordillera

Three locations in the westernmost Coastal Cordillera near 20.3'S in close

proximity to one another (spaced <10 km apart) provide suitable gypsic soil of

constrained ages. Gypsisol samples NC12-82 (< 8.6 Ma) and NC12-84 (< 15.2 Ma,

>2.7 Ma), as well as gypsic relict soil sample NC12-80 (onset of accumulation < 8

Ma), have a high likelihood (~87 to ~100%) of having been formed in the paleo-fog

zone (Table B3 in Appendix B). Both Gypsisol samples have a modern elevation (823

and 472 m.a.s.l., respectively) within the Holocene-averaged fog zone (~220-250 to

1050-1100 m.a.s.l.). Each Gypsisol sample also has a modern elevation within their

estimated paleo-fog zone (~240 to ~1090 m.a.m.s.l. and 220-250 to 1050-1100

m.a.m.s.l., respectively). On one hand, the difference between the height of the base of

the paleo-fog zone and the modern elevation of each of these samples indicates the

maximum net uplift that could have occurred since these Gypsisols formed, of ~600 m

at site NC12-82 and ~250 m at site NC12-84. On the other hand, the difference

between the height of the top of the paleo-fog zone and the modern elevation of each of these samples indicates the maximum net subsidence that could have occurred in the same time frames, of ~300 m at site NC12-82 and ~600 m at site NC12-84. Gypsic relict soil NC12-80 (1148 m.a.s.l.) lies ~75 m above the Holocene fog zone top. However, its Sr isotopic signal indicates formation within the altitudinal band of late Miocene – Pliocene fog (~200 - ~1050 m.a.m.s.l.). Therefore, the span of appropriate interpretation lies between an increase in altitude of at least ~100 m and of no more than ~950 m. Considered together, and taking into account the different age constraints available at the three sites, the data is consistent with all of the following: (1) a maximum permissible net surface uplift of ~250 m since sometime before 2.7 Ma, (2) at least ~100 m of net surface uplift since sometime after 8 Ma, and (3) a maximum permissible net surface uplift of ~600 m and a maximum permissible net surface subsidence of ~300 since < 8.6 Ma in the western Coastal Cordillera at 20.3-20.4°S (Table 3-1; Fig. 3-9d).

Farther south along the Coastal Escarpment, near 20.75°S, Gypsisol site NC11-46 (Fig. 3-6) is younger than 4.2 Ma (± 0.4 Ma) and has a ~100% likelihood of having been formed in the paleo-fog zone (Table B3 in Appendix B). Today it is located at an altitude of 506 m.a.s.l. on the coastal escarpment, within both the Holocene-averaged fog zone and its estimated paleo-fog zone (~210 - ~1060 m.a.m.s.l.). Thus, this is consistent with zero net surface change since sometime after 4.6 Ma during the Pliocene or early Pleistocene. It is also consistent with a maximum net surface uplift of ~300 m, or a maximum net surface subsidence of ~550 m since < 4.6 Ma (Table 3-1; Fig. 3-9d).

At the southernmost site in the western Coastal Cordillera, near 21.17°S, relict soil TJ12-117 is younger than 4 Ma and is located at a modern elevation of 741 m.a.s.l. (Fig. 3-6), within both the modern fog zone and the paleo-fog zone at the time

at which samples TJ12-117a & b formed (~210 - ~1060 m.a.s.l.). They both have a 100% likelihood of having formed within the paleo-fog zone, which is consistent with this area having experienced no net surface uplift since sometime after 4 Ma. It is also consistent with a maximum net surface uplift of ~550 m or a maximum net surface subsidence of ~300 m since < 4 Ma (Table 3-1; Fig. 3-9d).

Considering whole-block surface elevation change along the ~100 km-long studied section of the westernmost Coastal Cordillera, the Gypsisols' and gypsic relict soils' $^{87}Sr/^{86}Sr$ are consistent with either (a) maximum net surface uplift of ~250 m, (b) maximum net surface subsidence of ~300 m, or (c) no net surface elevation change since the early Pliocene (Table 3-1; Fig. 3-9d).

3.5.5 Clarifying interpretations based on geological context

The application of our new paleoaltimetry method to Gypsisols and gypsic relict soils of the Atacama Desert constrains surface elevation within the Central Depression and Coastal Cordillera of northern Chile (Table 3-1; Fig. 3-9). For several individual sites the data are insufficient to select the correct interpretation among several choices of opposing sign and magnitude that honor the $^{87}Sr/^{86}Sr$ data (Fig. 3-3c). Furthermore, the precision with which the $^{87}Sr/^{86}Sr$ of a gypsic soil places a numerical constraint on the magnitude of change in surface elevation is a function of the current elevation of the sample site. For a gypsic soil that formed above the contemporaneous fog top, a sampling site located above the Holocene fog top near the axis of the Central Depression (1000-1100 m.a.s.l.) can place a maximum constraint on uplift of tens of meters. But the same information from the eastern Aroma, eastern Tambillo and Arcas sites at elevations ranging form 1600–1900 m.a.s.l., cannot provide precision better than 500-800 m. Likewise, for gypsic soils formed within the

altitudinal band of contemporaneous fog, the precision with which uplift or subsidence can be quantified depends on the current altitude at which the soil was sampled. Consequently the maximum permissible uplift reported for each sub-region (Table 3-1) contains this methodological limitation that changes with elevation as well as containing geological information.

For most sites, the results suggest that no more than ~600 m of uplift has taken place in the Central Depression and westernmost Coastal Cordillera between 19.5-21.7ºS since the earliest Pliocene. For the majority of these sites, the maximum permissible net surface uplift since the earliest Pliocene is actually lower: ~100-250 m. No net surface change or even net subsidence are equally allowed by the data. The exception corresponds to the westernmost Central Depression at 21.4ºS, where at least ~50 m of net subsidence has taken place since < 4.5 Ma (Table 3-1; Fig. 3-9b).

The results led to multiple acceptable interpretations of the altitude at which the gypsic soil formed for the Camarones, Tiliviche (see sections B2-B3 in Appendix B), and Coastal Cordillera sub-regions. The uncertainty at Tiliviche is reduced by weighing the alternatives in the context of the regional continuity of the geomorphic surface in which the soil sample site is embedded [Mortimer and Saric Rendic, 1975; García et al., 2011; Kirk Lawlor et al., 2013]. The vertical profile of the Aroma sub-region provides evidence favoring the interpretation that the soils formed above the top of the paleofog horizon. The Tiliviche sub-region lies only 30 km distance from the Aroma region in the same geomorphic surface [Kirk Lawlor et al., 2013] and samples similar current elevations (1159-1398 m.a.s.l.) as the western Aroma sites (1367 m.a.s.l.). This geomorphological continuity weakens the interpretation that the Tiliviche gypsic soils originated below the base of the paleofog zone and rose in elevation by >1000 m. Had it been true, then what is now a laterally continuous pediment slope would be interpreted to have formed near sea level at Tiliviche but

above 1000 m.a.s.l. only 30 km away, a difference that is inconsistent with the similarity of Middle Miocene alluvial fan deposits which underlie the surface and the similarity of incision since the fans became inactive at both locations [Kirk Lawlor et al., 2013]. We thus favor the interpretation that the Pampa de Tiliviche area could not have uplifted more than ~250 m since the earliest Pleistocene (Table 3-1). A similar extrapolation to the Camarones sub-region is reasonable but much less reliable because of an added >50 km distance and three deep incised canyons between the Tiliviche and the Camarones sites.

The Aroma canyon sites are currently located above the Holocene-averaged fog zone top and their oldest, deepest horizons show no fog signals in their calcium sulfate Sr isotopic compositions. Thus, the constraint these data provide is that of a minimum surface elevation at any given time. Under the hypothesis of whole-block surface evolution, a maximum permissible net surface uplift of ~450 m has taken place since the latest Pliocene (Table 3-1; Fig. 3-9a). This is consistent with the findings of Evenstar et al. [2015] based on the concentration of cosmogenic ^{3}He in alluvial boulders located in the piedmont, that most of the current elevation in the area was achieved before 13.4 Ma.

The Tambillo sub-region is laterally continuous with the geomorphic surface on which the 20 km distant Arcas gypsic soil formed and most of the sample sites are at similar modern elevations, roughly 1000-1500 m.a.s.l.. Therefore, the Tambillo sub-region interpretation and the Arcas sub-region interpretation should be coherent. The Tambillo Canyon and Arcas areas revealed no fog signal for middle to upper Pliocene and Quaternary samples, which are located within error above or slightly within the paleo-fog zone. The western Tambillo sites show that no more than ~150 m of net uplift could have taken place in the area since the late Pliocene (Table 3-1; Fig. 3-9b) and the Arcas sites show a maximum permissible net surface uplift of ~100 m since

the earliest Pliocene (Table 3-1; Fig. 3-9c). We thus interpret that no more than ~100 m of whole-block uplift could have occurred in the Arcas-Tambillo sites since the earliest Pliocene (Table 3-1; Fig. 3-9b; Fig. 3-9c).

The paleo-altimetric method does not appear to be equally appropriate at all locations, even within northern Chile's hyperarid Atacama Desert. For example, the latitudinal band of 20.5-21°S contains both Holocene surface accumulations of calcium sulfate and Neogene gypsic soils whose ^{87}Sr/^{86}Sr are inconsistent with the fog-controlled altitudinal band hypothesis. The combination of independent information regarding the long-term wind climatology with the isotopic results from the Chipana and Guatacondo Canyon areas show that localized eolian transport of salts produced at low elevations to high positions in the landscape is a likely explanation of anomalous results in this zone, and must be anticipated elsewhere. For this latitudinal zone, the marine fog-derived, high ^{87}Sr/^{86}Sr calcium sulfates were carried to altitudes outside of the usual altitudinal distribution of the ^{87}Sr/^{86}Sr signal.

3.5.6 Regional tectonic uplift implications of new Central Depression paleoelevation results

For the Central Depression, the relationship of the sample sites to the toe of the Andean plateau western slope is an important factor in assigning tectonic significance to the results. Hoke et al. [2007] and Jordan et al. [2010] presented relative uplift evidence for the Andean western slope for areas that overlap this project. They demonstrate that 1200 m of topographic relief developed between the Central Depression and the Andes across a broad monoclinal fold during the late Miocene to present. The western limit of this large-scale structural feature is a fold hinge. Any paleoaltimetric sample sites located east of the hinge on the lower margin of the

monocline would measure some fraction of the uplift of the monocline system in addition to uplift of the forearc crustal block. Jordan et al. [2010] defined the position of the western hinge by seismic reflection geometries (Fig. 3-1). With the exception of the Miñi Miñi site (MM4.5, MM8) and the two easternmost samples in the Aroma canyon area (NC11-24, NC11-25), all the gypsic relict soil and Gypsisol sites are west of the downdip monoclinal hinge. Therefore, these new paleoaltimetric results indicate surface elevation changes in the Central Depression that are probably unrelated to the deformation of the eastern margin of the forearc. Our results are thus complementary to the aforementioned studies since they offer an absolute surface elevation framework for the Central Depression.

For most of our studied sites, our results suggest small net surface uplift of at most ~250 m during the last 5 million years. Data obtained from high elevation sites allow up to ~600 m of net uplift in the same time frame. Nonetheless, these constraints represent maximum permissible net uplift, and thus scenarios of no net surface change or of net subsidence are equally consistent with the data.

During the 0-5 Ma time interval Garzione et al. [2006] and Kar et al. [2016] demonstrated near zero uplift of the Altiplano and Jordan et al. [2010] deduced 400 m ± 170 m uplift across the western Andean slope. Also, Evenstar et al. [2015] quantified uplift using cosmogenic nuclide data for two sites at which some of our samples are co-located. They showed that all but a small fraction of the current site elevations (1690 m and 1900 m) must have existed at the end of the Middle Miocene. Because the sites lie at and less than 10 km east of the lower hinge of the western Andean monocline, neither our results nor those of Evenstar et al. [2015] constrain uplift of the tectonic block containing the Andes and Altiplano. Nevertheless, this paper suggests that an extrapolation from Evenstar et al.'s [2015] localized results to

the western forearc in general may be robust, although caution is needed because the time spans differ.

3.5.7 Regional tectonic uplift implications of new Coastal Cordillera paleoelevation results

The abrupt increase in surface elevation across the Coastal Escarpment constitutes a major out-of-equilibrium geomorphological feature, which leads to the hypothesis that large magnitude uplift occurred in the comparatively recent past [e.g. Hoke et al., 2007]. However, considering whole-block surface elevation change along the ~100 km-long studied section of the westernmost Coastal Cordillera, our $^{87}Sr/^{86}Sr$ data for dated ancient soils are consistent with either (a) maximum net surface uplift of ~250 m, (b) maximum net surface subsidence of ~300 m, or (c) no net surface elevation change since the early Pliocene (Table 3-1; Fig. 3-9d). In light of this documentation of small amounts of Pliocene to recent net surface uplift in the area, the out-of-equilibrium profile of the Coastal Escarpment is interpreted as a relict of much older uplift phenomena that has been maintained by the extremely small denudation rate of the Atacama Desert [Dunai et al., 2005; Carrizo et al., 2008; Evenstar et al., 2009].

At a shorter timescale, Regard et al. [2010] concluded that there has been 165 m of net surface uplift of the northern Chilean coastal escarpment, including our study area, since 0.4 ± 0.1 Ma, which was preceded by a period of quiescence or even subsidence during the late Pliocene (Table 3-1). Our results are more consistent with this pulse-like behavior of surface elevation evolution than with slower uplift rates of ~0.12 m myr^{-1} derived by Melnick [2016], if those rates were to be characteristic since the early Pliocene.

3.5.8 New paleoaltimetry method caveats

The extent to which this method can be used to determine the timing of pre-4.5 Ma uplift is limited by the scarcity of locations with ancient soils in the Central Depression whose documented ages are between ~11-4.5 Ma. None are known to be older than ~11 Ma [Jordan et al., 2014]. Because hyperarid conditions may have persisted for an even longer time within the Coastal Cordillera [Dunai et al., 2005; Carrizo et al., 2008] there may be better opportunities within the Coastal Cordillera to investigate pre-Pliocene surface elevations. Further exploration for tractable sites in the Coastal Cordillera must meet several criteria. First, for changed altitude to be detectable, locations are needed that formed either i) near sea level (below their contemporaneous fog zone bottom) and are now located within the modern fog zone, ii) at altitudes below the upper threshold of their contemporaneous fog zone and are now located above it, or iii) above the contemporaneous fog zone and are now located within the Holocene fog band. Second, there must be calcium-sulfate rich ancient soils which, while common, are not ubiquitous. Third, at a minimum there must be local data that constrain the age of initiation of the Gypsisol or gypsic relict soil, and preferably there should also be constraints on intermediate points in the history of soil development.

This bi-modal, single-threshold $^{87}Sr/^{86}Sr$-elevation proxy method is limited in its resolution of paleoaltitudes because the Sr ratio signatures resolve only whether a location was within the elevation range of paleo-fog when a gypsic soil formed. Post-depositional Sr vertical migration within the gypsic relict soils limits the ability to extract a chronology of $^{87}Sr/^{86}Sr$ within the soils. For the studied sites, however, vertical mixing was not strong enough to overprint the primary Sr isotope signal.

Despite these significant limitations, the method has potential to resolve in the western forearc of the Central Andes, and perhaps in other hyperarid coastal areas, first-order paleoelevation histories.

3.6 Conclusions

The $^{87}Sr/^{86}Sr$ of pedogenic calcium sulfates that occur on the continental surface of the Atacama Desert can be used as a paleoaltimer because of the altitude-controlled extent of salts formed from marine aerosols. This new approach and data place constraints on the evolution of the absolute (i.e. with respect to sea level) surface elevation of the northern Chile western nonmarine forearc.

In all cases in the Central Depression and westernmost Coastal Cordillera between 19.5-21.7°S, the new paleoaltitude results demonstrate small magnitudes of elevation change compared to the elevation of the study area relative to sea level. For most locations, the paleoaltitude results determine the maximum permissible magnitude of uplift, but do not necessitate any uplift. For most sites, the results suggest that no more than ~550 m of uplift has taken place in the Central Depression and westernmost Coastal Cordillera between 19.5-21.7ºS since the earliest Pliocene. For the majority of these sites, the maximum permissible net surface uplift since the earliest Pliocene is lower: ~250 m.

We conclude that no more than 55% of the ~1000 m.a.s.l. average elevation of the Central Depression main axis and that no more than 30% of the ~900 m.a.s.l. average elevation of the westernmost Coastal Cordillera were accrued by uplift since the earliest Pliocene. These results point to small-magnitude uplift of the western non-

marine Andean forearc since ~5 Ma. We thus refute the hypothesis of kilometer-scale topographic uplift during the late Neogene.

The utility of this method is limited by the availability of age constraints on the relict gypsic soils and Gypsisols, and by post-depositional Sr vertical mixing. However, it has proved sufficient to allow first-order elevation constraints on the western non-marine forearc of the Central Andes, and may be of use in other hyperarid coastal regions.

3.7 Acknowledgements

3.8 Tables

Method	Locality	From (Ma)	To (Ma)	Amount (m)[1]	Amount assuming whole-block surface change (m)[1]	Reference
Table 3-1. Absolute Net Surface Uplift/Subsidence Estimates for the Non-Marine Forearc (Coastal Cordillera and Central Depression).						
marine strata	Ocoña River, S Peru	~25	0	2300		Thouret et al. [2007]
valley incision	Arica (18ºS)	< 8	> 2.6	?		Schlunegger et al. [2006]
valley incision	Tana Canyon, Chile (19.3-19.8ºS)	< 3	0	< 900		Kirk-Lawlor et al. [2013]
cosmogenic nuclides	Aroma Canyon, Chile (19.6ºS)	> 30	13.4	> 900		Evenstar et al. [2015]
structural, thermochronology	Southern Peru	< 5	2.2	< 1000		Schildgen et al. [2009]
various, shorelines	Coastal plain & cliff (16-30ºS)	0.4 ± 0.1	0	165		Regard et al. [2010]
various, shorelines		late Pliocene	late Pliocene	< 0		Regard et al. [2010]
soil ^{87}Sr/^{86}Sr paleoaltimetry	Camarones Canyon, Central Depression (18.9-19ºS)	< 2.7	0	> 100		this study
soil ^{87}Sr/^{86}Sr paleoaltimetry	Pampa de Tiliviche, Chile (19.4-19.5ºS)	< 2.5	0	~250 (maximum permissible)	~250 maximum permissible since < 2.5 Ma	this study
soil ^{87}Sr/^{86}Sr paleoaltimetry	Western Aroma Canyon (19.8ºS, 69.7ºW)	< 3	0	~450 (maximum permissible)		this study
soil ^{87}Sr/^{86}Sr paleoaltimetry	Eastern Aroma Canyon (19.7ºS, 69.6ºW)	< 3	0	~750 (maximum permissible)		this study
soil ^{87}Sr/^{86}Sr paleoaltimetry	West of Loma de Sal (21.4ºS, 69.5ºW)	~4.5	0	> -50 (minimum subsidence)		this study
soil ^{87}Sr/^{86}Sr paleoaltimetry	Western Tambillo Canyon (21.5ºS, 69.4ºW)	~3.6	0	~150 (maximum permissible)	~100 (maximum permissible since < 5.5 Ma)	this study
soil ^{87}Sr/^{86}Sr paleoaltimetry	Eastern Tambillo Canyon (21.4ºS,	~4.5	0	~600 (maximum		this study

	69.2ºW)			permissible)		
soil ^{87}Sr/^{86}Sr paleoaltimetry	Central-North Arcas Fan (21.6ºS, 69.3ºW)	~4.3	0	~400 (maximum permissible)		this study
soil ^{87}Sr/^{86}Sr paleoaltimetry	Distal Arcas Fan (21.7ºS, 69.5ºW)	< 5.5	0	~100 (maximum permissible)		this study
soil ^{87}Sr/^{86}Sr paleoaltimetry	Western Coastal Cordillera (20.3-20.4ºS)	> 2.7	0	~250 (maximum permissible)	~250 maximum permissible since the early Pliocene; ~ -300 maximum permissible since the early Pliocene	this study
soil ^{87}Sr/^{86}Sr paleoaltimetry		< 8	0	> 100		this study
soil ^{87}Sr/^{86}Sr paleoaltimetry		< 8.6	0	~600 (maximum permissible); ~ -300 (maximum permissible)		this study
soil ^{87}Sr/^{86}Sr paleoaltimetry	Western Coastal Cordillera (20.75ºS)	< 4.6	0	~300 (maximum permissible); ~ -550 (maximum permissible)		this study
soil ^{87}Sr/^{86}Sr paleoaltimetry	Western Coastal Cordillera (21.17ºS)	< 4	0	~550 (maximum permissible); ~ -300 (maximum permissible)		this study

[1]Positive values correspond to uplift; negative values correspond to subsidence

3.9 Figures
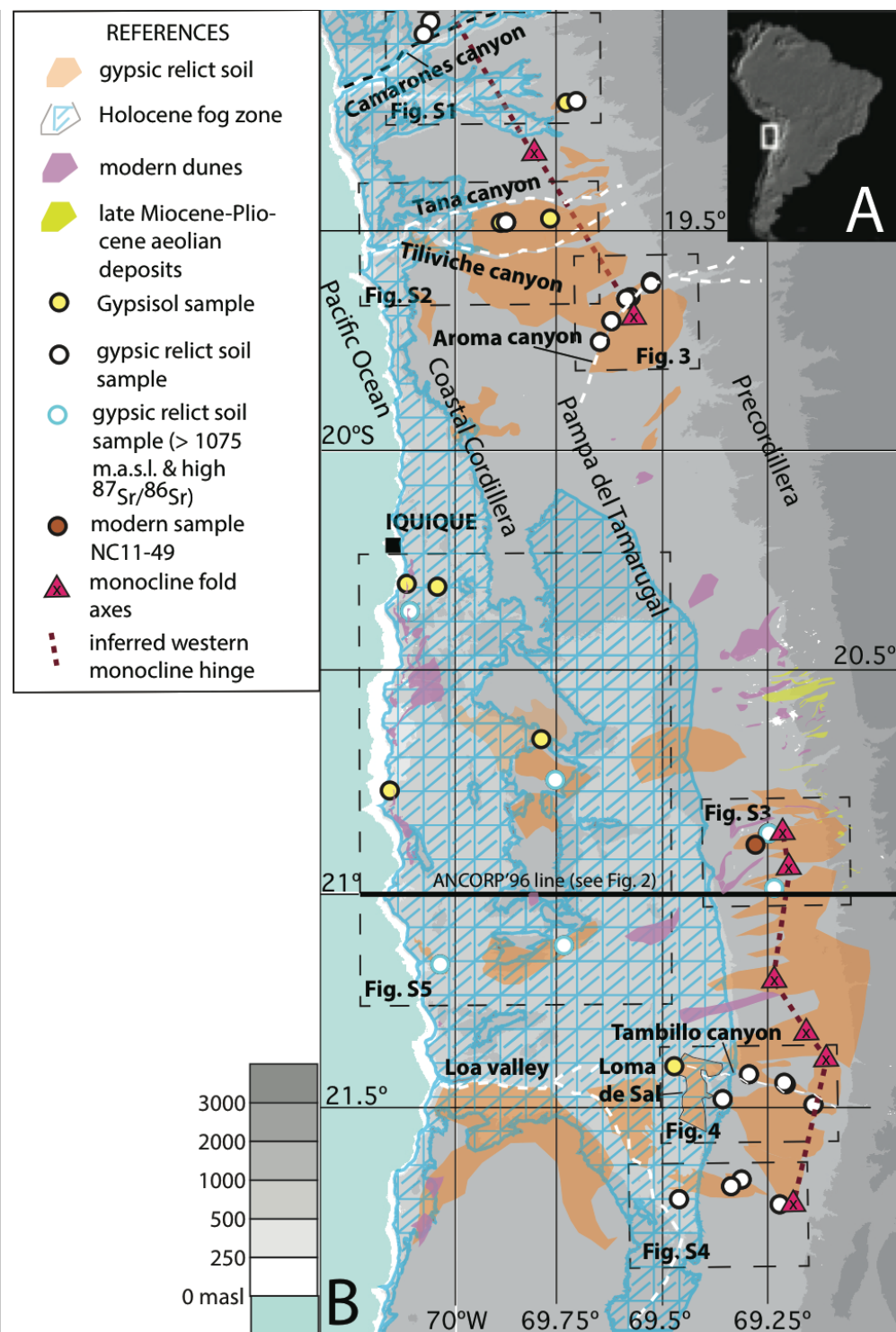
Figure 3-1. (see next page)

Figure 3-1. A. South America and study area in box. B. Map showing the distribution of gypsic relict soils in the Central Depression of northern Chile below 3000 m.a.s.l. (see Table S1 for mapping criteria). The mapped gypsic relict soils within the Coastal Codillera are the subset of gypsic relict soils that could be mapped according to the criteria presented in the text, and should not be considered the complete set of gypsic relict soils capping surfaces within the Coastal Cordillera. Also shown are modern eolian landforms (satellite image analysis combined with 1:1,000,000 mapping; SERNAGEOMIN, [2003]), late Miocene-Pliocene eolian deposits (based on Nester and Jordan, [2011] and 1:100,000 mapping by Blanco and Tomlinson, [2013] in the Guatacondo area) and site NC11-49 ($^{87}Sr/^{86}Sr$ = 0.70835) of Holocene accumulations of salts higher than the Holocene-averaged fog zone top (see Fig. 3-2b). The subset of gypsic relict soil sites that both have a fog signal and are higher than 1075 m.a.s.l. is also shown. Dashed white lines are fluvial valleys that incise the forearc all the way to the Pacific Ocean. The area under the influence of the Holocene-averaged fog zone is shown in light blue. Crosses represent locations of monoclinal fold axes, and from these the dashed pink line is drawn as an inference of the western monocline hinge position [Jordan et al., 2010]. Seismological line ANCORP'96 shown in thick black.
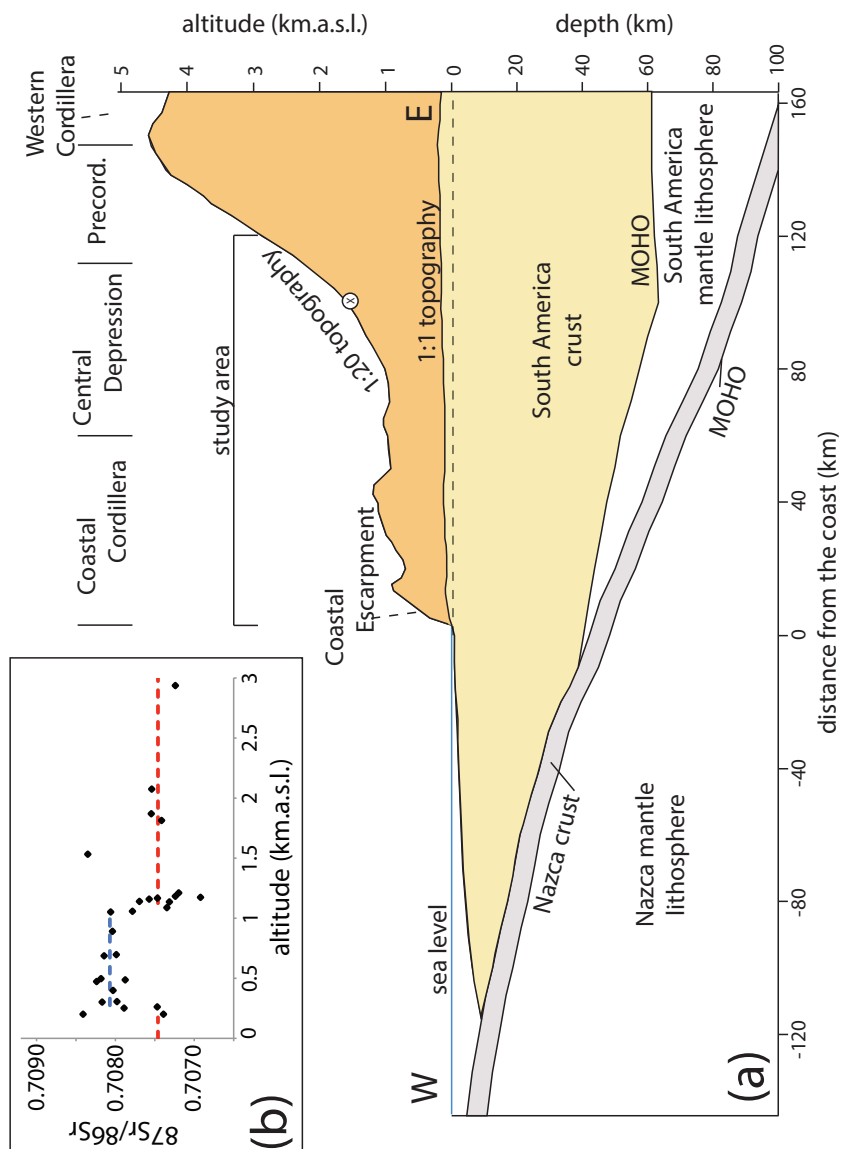
Figure 3-2. (a) Simplified cross section of the forearc lithosphere, from the Nazca Plate to the western flank of the Central Andes in northern Chile (21ºS). Thicknesses and divisions are based on seismological interpretations of geophysical data collected along line ANCORP'96 and receiver function data (Victor et al., [2004] and references therein). The upper envelope of the crust is the topographic surface, shown both with 1:1 and 1:20 vertical exaggeration. The cross represents the down-dip hinge of the long-wavelength, crustal-scale monocline [Jordan et al., 2010]. (b) Holocene accumulations of salts' $^{87}Sr/^{86}Sr$ and altitude of formation (n = 28) in the Atacama Desert [Chapter 2; i.e. Cosentino et al., 2015]. The red dashed line represents the bootstrap value for the Holocene-averaged outside-of-the-fog isotopic ratio (0.70746 ± 0.00010), while the blue dashed line corresponds to the inside-of-the-fog equivalent (0.70807 ± 0.00004). Colored boxes correspond to the bootstrap standard errors in the definition of the average values. The vertical black dashed lines correspond to the Holocene-averaged base and top of the fog zone (225 and 1075 m.a.s.l., respectively). Precord.: Precordillera.
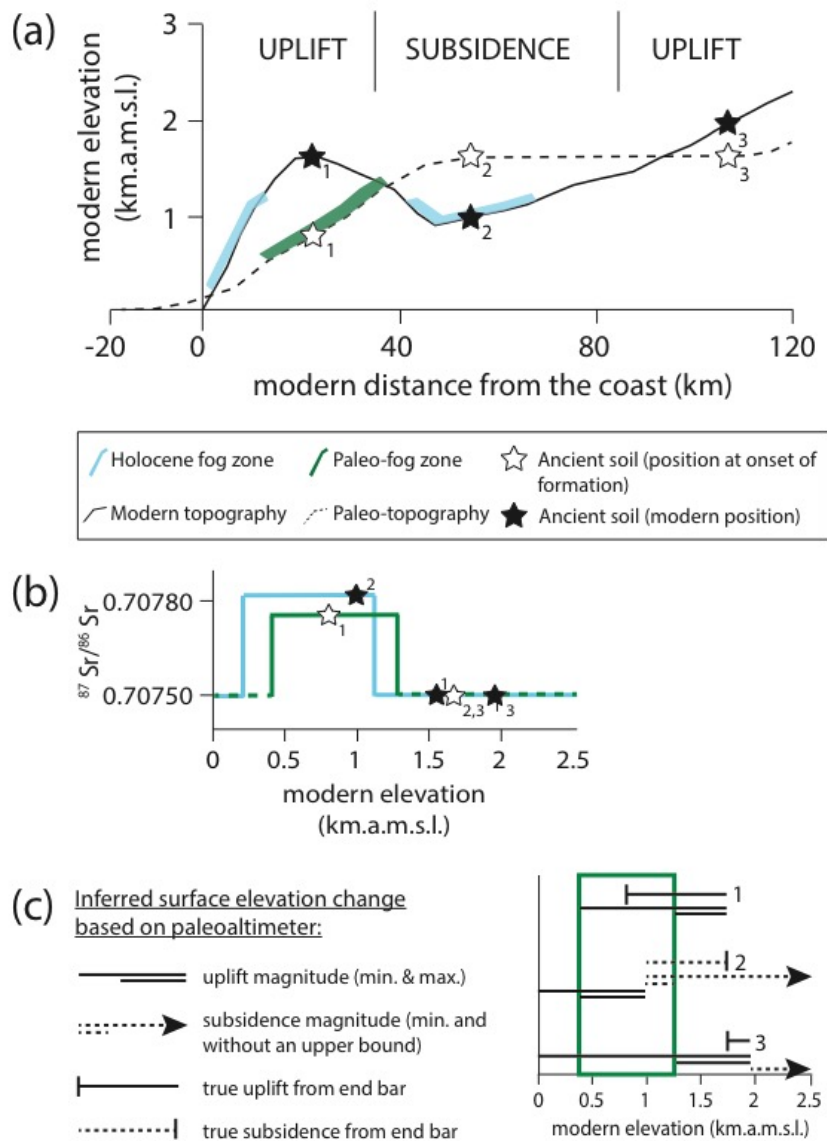
Figure 3-3. (a) Hypothetical paleo and modern topographic configurations, Holocene time-averaged fog zone, paleo-fog zone, and ancient soil locations. Sites shown by stars 1-3 illustrate the elevations at which a soil formed (open stars) and at which it is now found (solid stars). (b) Holocene accumulations of salts in the landscape and within the Holocene time-averaged fog zone have calcium sulfate $^{87}Sr/^{86}Sr$ of 0.70807 ± 0.00004 (bootstrap 1σ), while for those located outside this value is 0.70746 ± 0.00010 (bootstrap 1σ) [Chapter 2; i.e. Cosentino et al., 2015]. Correction factors needed to quantify elevation change are schematically indicated: the rise in seawater $^{87}Sr/^{86}Sr$ with time translates to a higher $^{87}Sr/^{86}Sr$ within the Holocene fog zone than within paleo-fog zones; the rise in eustatic sea level results in a rise of the fog zone layer, while lower sea surface temperatures (SST) result in a lower fog zone layer. (c) For the soil sites in (a), the starting elevation is marked by the vertical bar and the true change in elevation is shown. For each site, several interpretations of the magnitude of uplift or subsidence based on the proposed paleoaltimeter method are also shown. Geological context and geochemical information are needed to choose among the alternatives.
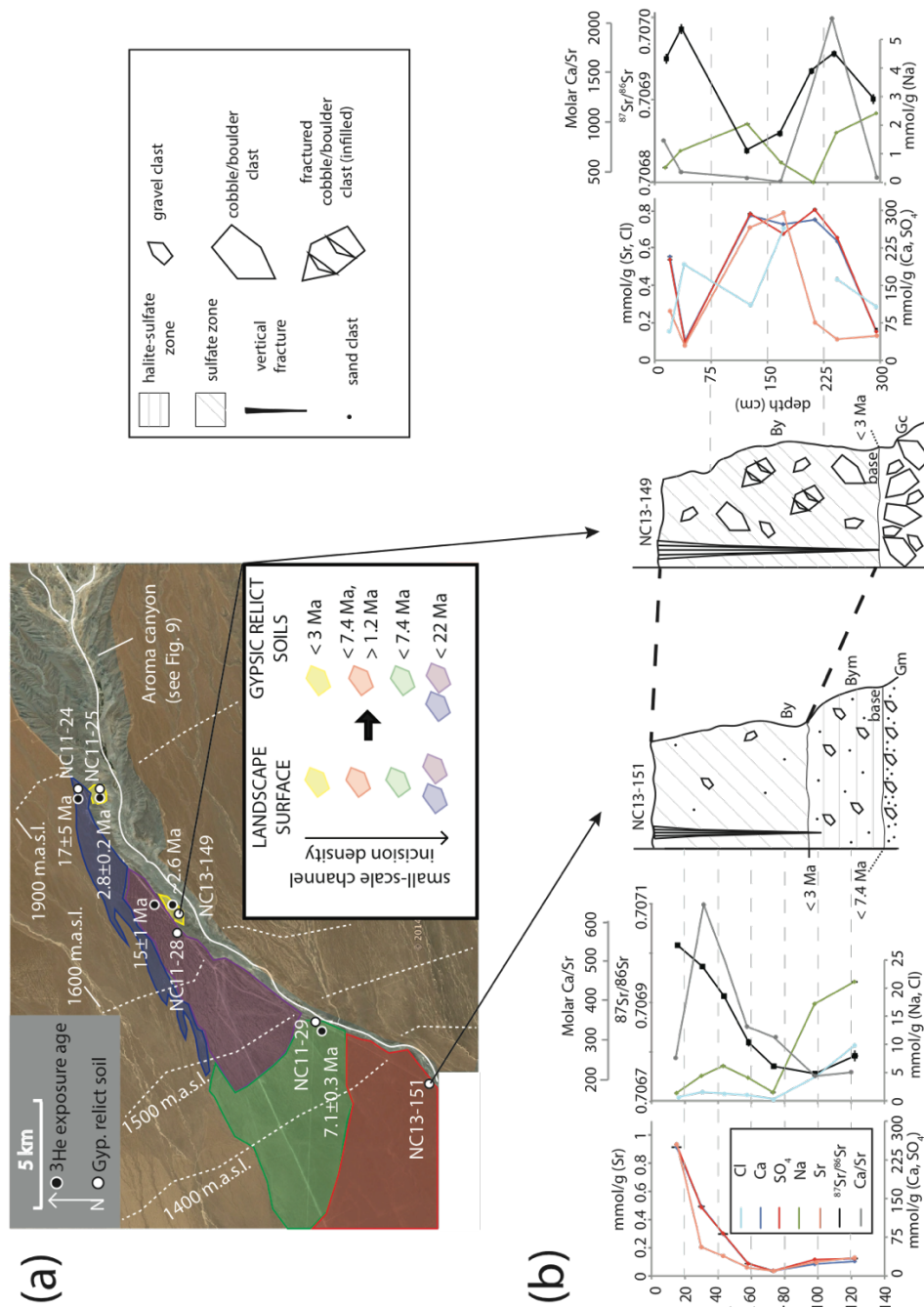
Figure 3-4. Chronological constrains on relict gypsic soils and Gypsisols of the Aroma canyon area. (a) Map of surface zones defined by density of incised minor drainage channels (colors), modern elevations (dotted white contours), and sample locations. (b) Profiles of soil zones and salt profiles for relict and paleosols that form the landscape surface. Ages given in profiles are the interpreted time of initiation of accumulation of each soil unit, based in part on [3]He exposure ages [Evenstar et al., 2009] and on soil unit correlations based on physical and chemical soil characteristics of the soil profiles. For soil NC13-151 a hiatus in soil accumulation is inferred between an unspecified point in time and 2.6 Ma, coinciding with the Bym-By unit boundary. Only soil profiles with dense vertical sampling have been included.

113
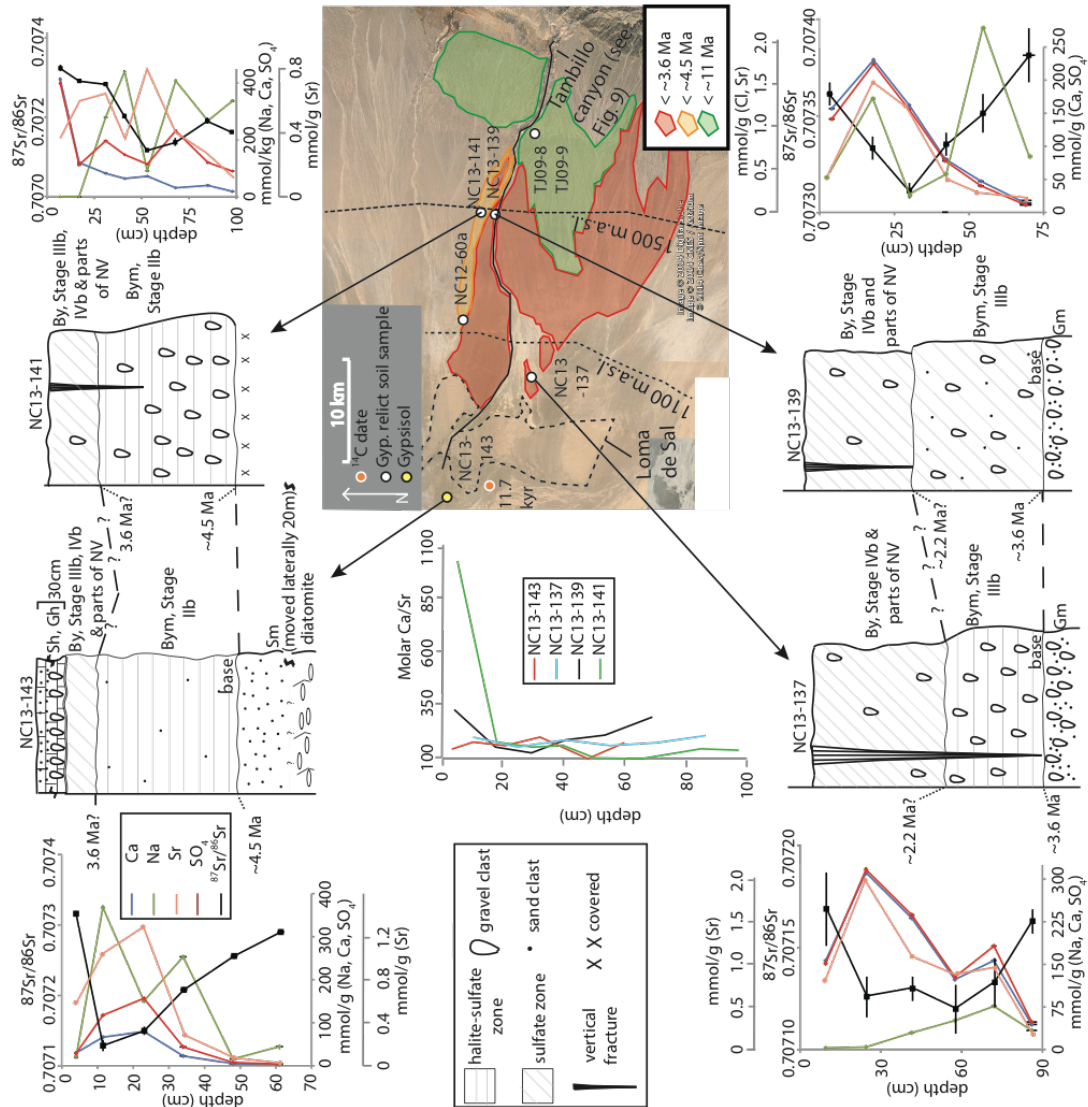
Figure 3-5. Chronological constrains on relict gypsic soils and Gypsisols of the Tambillo canyon and Lomas de Sal area. Ages correspond to the time of initiation of accumulation of each soil unit, based on arid/hyperarid cycles [Jordan et al., 2014] and on soil unit correlations based on physical and chemical characteristics of the soil profiles. For soils NC13-141 and NC13-143 a hiatus in soil accumulation is inferred between 4 Ma and 3.6 Ma, corresponding to Jordan et al.'s [2014] arid stage NIIIa. For soils NC13-137 and NC13-139 a hiatus is inferred between 2.6 Ma and 2.2 Ma, corresponding to Jordan et al.'s [2014] arid stage NIVa. Only soil profiles with dense vertical sampling have been included.
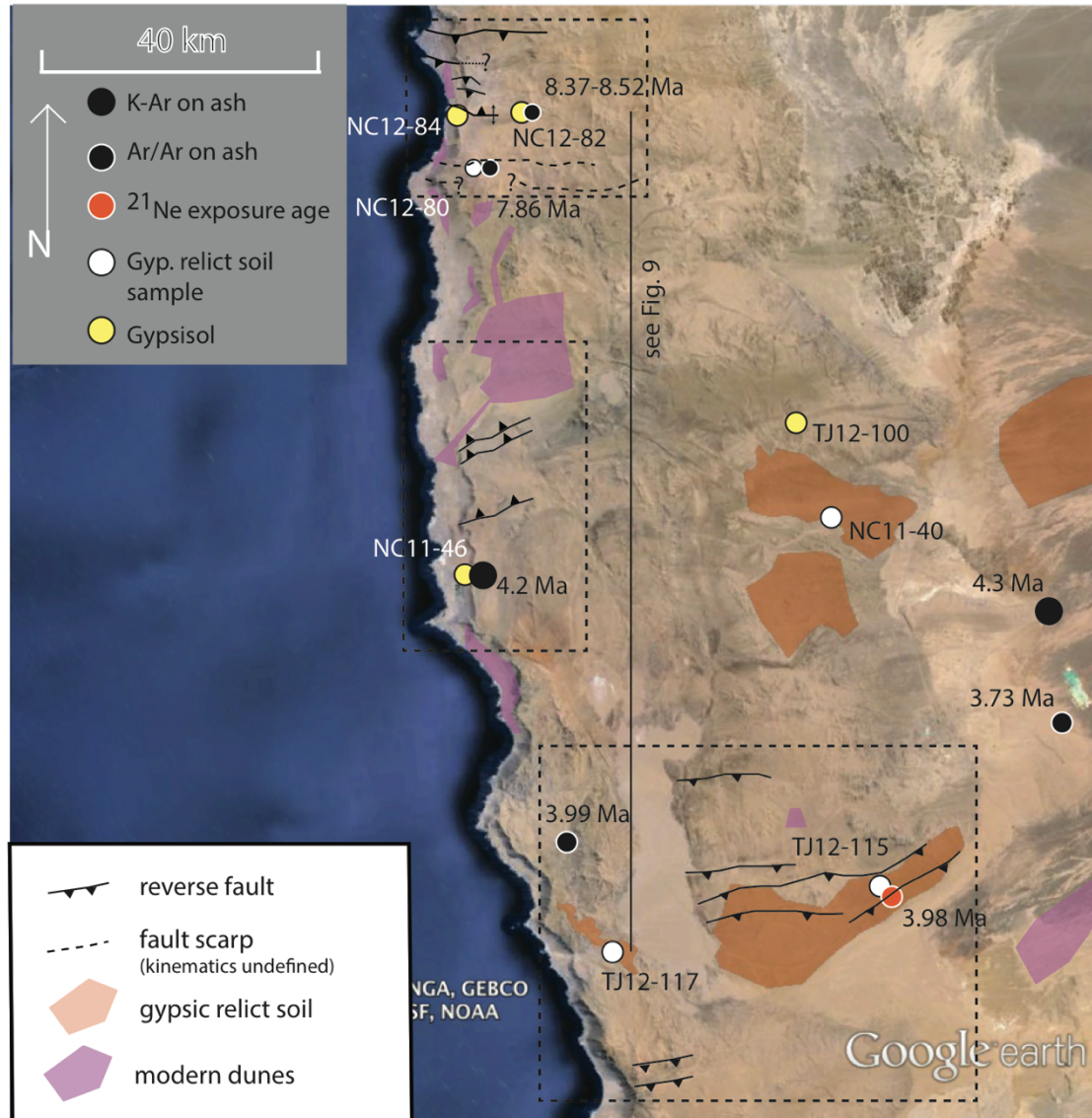
Figure 3-6. Sampled Gypsisols and gypsic relict soils in the Coastal Cordillera and Coastal Escarpment: ash dates correspond to Blanco et al. [2012], Baker [2012], Quezada et al. [2013] and Vásquez & Sepúlveda [2013] (Table B2 in Appendix B). The exposure age corresponds to Carrizo et al. [2008] (Table B2 in Appendix B). Mapping of east-trending inverse faults and fault scarps within the dashed boxes is based on Allmendinger et al. [2005], Allmendinger & González [2010], and DEM analysis. Double arrow indicates a fold scarp. Sawteeth on reverse faults on the upper plate. See Fig. 3-1 for the general study area map.
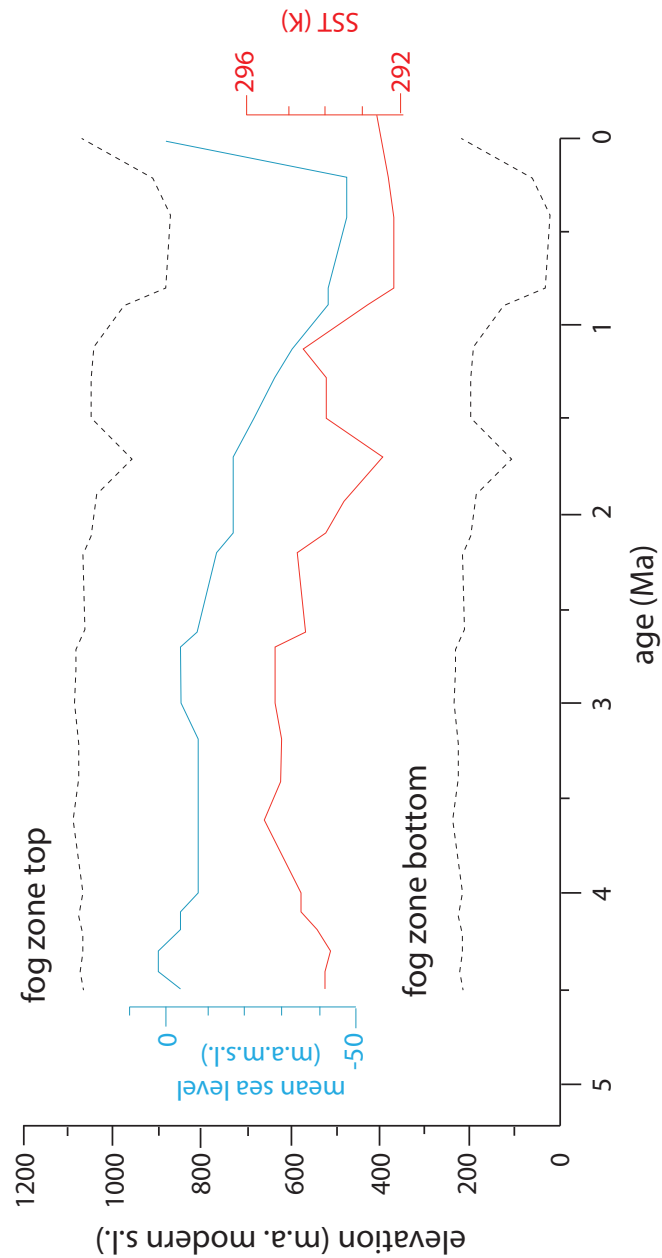
Figure 3-7. Evolution of mean sea level, paleo-SST offshore northern Chile, and the fog zone top and bottom during the Pliocene-Holocene (since 4.5 Ma). Mean sea level was averaged using a 0.1 myr window. Best-estimate paleo-SST based on the Dekens et al.'s [2007] weighted smoothing curve for ODP site 1237. Corrections on paleo-SSTs were applied to account for the difference between modern SST at the ODP 1237 site and the average coastal SST in the study area at 18.75-21.75ºS (World Ocean Atlas 2013 - NODC - NOAA - 1955-2012 decadal average), as well as for the eastward migration of ODP site 1237 through the last 5 m.y. [Mix et al., 2003]. The latter explains part of the cooling trend observed (1 ºC at 5 Ma, linearly interpolated to 0 ºC at 0 Ma).
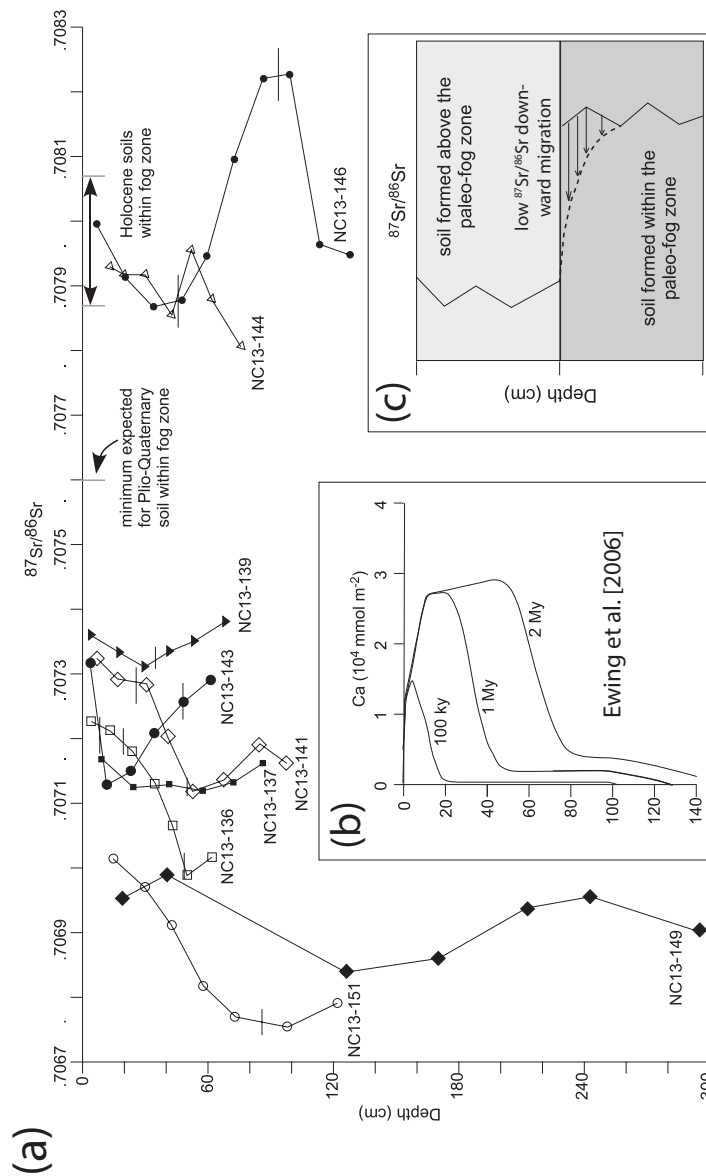
Figure 3-8. (a) Vertical soil profiles of $^{87}Sr/^{86}Sr$ for nine sites. The horizontal lines in profiles mark the position of soil horizon boundaries (details in Fig. 3-4; Fig. 3-5; Fig. B6 in Appendix B; Fig. B8 in Appendix B). Values of $^{87}Sr/^{86}Sr$ expected of gypsic soil formed in the fog elevation belt are noted. (b) Modeled vertical soil profile of Ca concentrations (mmol m^{-2}cm^{-1}) that result from a ~2 myr simulation of atmospheric Ca input and downward Ca transport that considers small, infrequent and regularly recurring rainfall events (see Ewing et al. [2008] for the transport model parameters used in the simulation). The soil profile started to accumulate ~2 myr ago and is located in the Coastal Cordillera at 24.1ºS and 70.0ºW, at an altitude of 1022 m.a.s.l. [Ewing et al., 2008]. (c) Hypothetical vertical distribution of $^{87}Sr/^{86}Sr$ for a gypsic relict soil that started to accumulate within the paleo-fog zone, then suffered enough uplift to place it above the paleo-fog zone, and then continued to accumulate to the present (solid line). The dashed line shows plausible smoothing and downward shift of the Sr isotopic variations due to dissolution, based on (b).

117
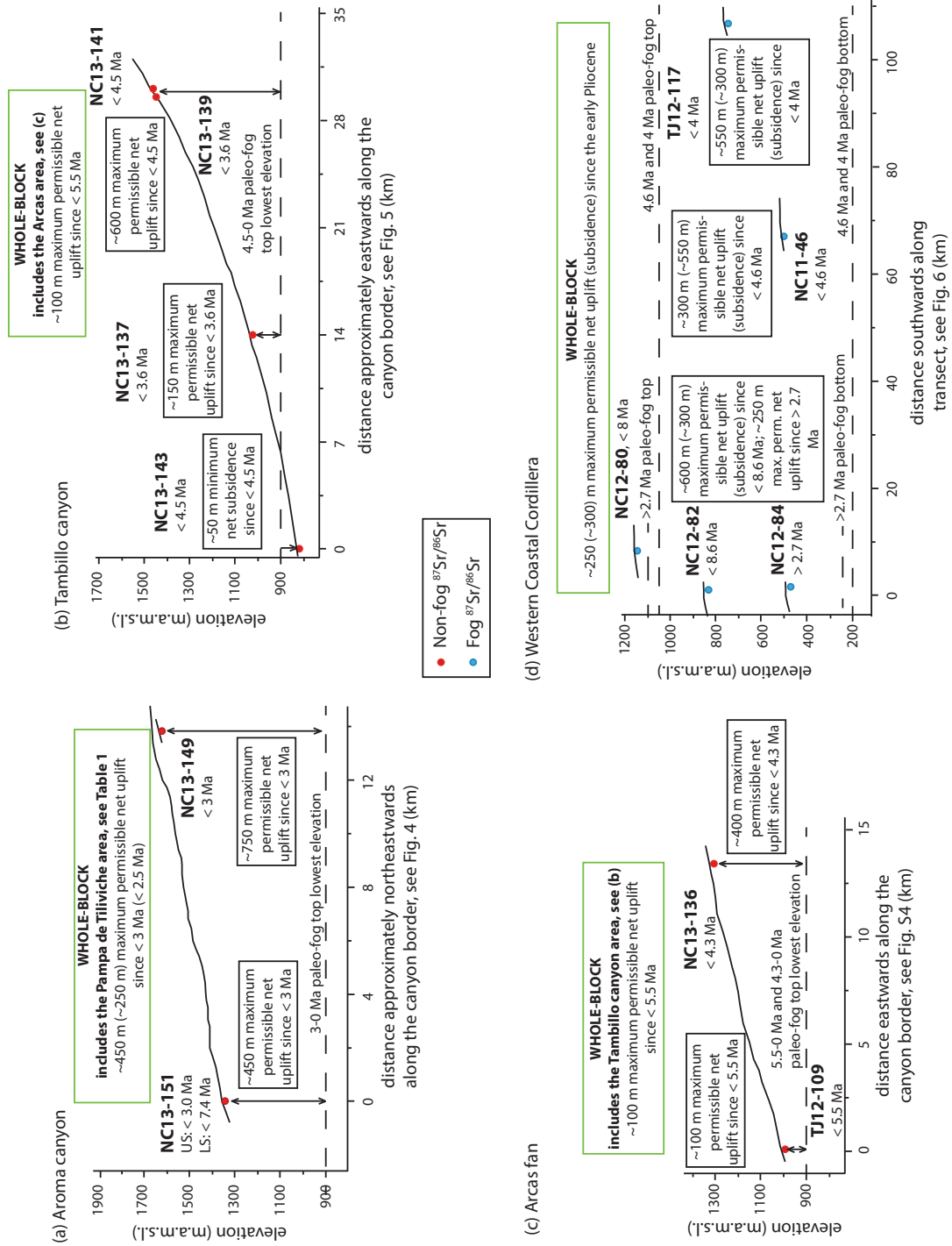
Figure 3-9. Cross-sections showing modern elevations and locations of sites for which paleoaltimetric constraints could be extracted: (a) Aroma canyon, (b) Tambillo canyon and Loma de Sal hills, (c) Arcas fan, and (d) Western Coastal Cordillera. The preferred interpretation of uplift or subsidence at each site and its magnitude are noted.

REFERENCES

Allmendinger, R. W., G. González, J. Yu, G. Hoke, and B. Isacks (2005), Trench-parallel shortening in the Northern Chilean Forearc: Tectonic and climatic implications. *Geological Society of America Bulletin* **117**, 89-104.

Allmendinger, R. W., and G. González (2010), Invited review paper: Neogene to Quaternary tectonics of the coastal Cordillera, northern Chile. *Tectonophysics* **495**, 93-110.

Amiot, R., U. B. Gohlich, C. Lécuyer, C. de Muizon, H. Cappetta, F. Fourel, M. Héran, and F. Martineau (2008), Oxygen isotope compositions of phosphate from Middle Miocene-Early Pliocene marine vertebrates of Peru. *Palaeogeography, Palaeoclimatology, Palaeoecology* **264**, 85-92.

Amundson, R., W. Dietrich, D. Bellugi, S. Ewing, K. Nishiizumi, G. Chong, J. Owen, R. Finkel, A. Heimsath, and B. Stewart (2012), Geomorphologic evidence for the late Pliocene onset of hyperaridity in the Atacama Desert. *Geological Society of America Bulletin* **124** (7-8), 1048-1070.

Arancibia, G., S. J. Matthews, and C. Pérez de Arce (2006), K-Ar and $^{40}Ar/^{39}Ar$ geochronology of supergene processes in the Atacama Desert, northern Chile: tectonic and climatic relations. *Journal of the Geological Society* **163** (1), 107.

Baker, A. (2012), Alluvial fan surfaces in the Atacama Desert: Implications for surface modification rates, the earthquake cycle, and Mars, PhD thesis, Earth & Atmospheric Sciences, Cornell University, Ithaca, New York, USA.

Barnes, J. B., and T. A. Ehlers (2009), End member models for Andean Plateau uplift. Earth Sience Reviews 97 (1-4), 105-132.

Beck, M., R. Bermester, J. Cembrano, R. Drake, A. García, F. Hervé, and F. Munizaga (2000), Paleomagnetism of the North Patagonian Batolith, southern Chile. An exercise in shape analysis. *Tectonophysics* **326 (1-2)**, 185-202.

Blanco, N., and A. Tomlinson (2013), Carta Guatacondo, Región de Tarapacá. *Servicio Nacional de Geología y Minería, Carta Geológica de Chile, Serie Geológica Básica*, p. 1. Mapa de escala 1:100,000. Santiago.

Blanco, N., P. Vásquez, F. Sepúlveda, A. J. Tomlinson, A. Quezada, and M. Ladino (2012), Levantamiento geológico para el fomento de la exploración de recursos minerales e hídricos de la Cordillera de la Costa, Depresión Central y Precordillera de la Región de Tarapacá (20°-21°S). Servicio Nacional de Geología y Minería, Informe Registrado IR-12-50: 246 p., 7 mapas escala 1:100.000. Santiago.

Carrizo, D., G. González, and T. Dunai (2008), Constricción neógena en la Cordillera de la Costa, norte de Chile: neotectónica y datación de superficies con ^{21}Ne cosmogénico. *Revista Geológica de Chile* **35** (1), 1-38.

Cereceda, P., P. Osses, H. Larrain, M. Farías, M. Lagos, R. Pinto, and R. S. Schemenauer (2002), Advective, orographic and radiation fog in the Tarapacá region, Chile. *Atmospheric Research* **64**, 261-271.

Cosentino, N. J., T. E. Jordan, L. A. Derry, and J. P. Morgan (2015), ^{87}Sr/^{86}Sr in recent accumulations of calcium sulfate on landscapes of hyperarid settings: A bimodal altitudinal dependence for northern Chile (19.5°S–21.5°S). Geochem. Geophys. Geosyst. **16**, 4311-4328.

Cosentino, N. J., et al., (2016a), Sr isotopic ratios of ancient gypsic soils in Atacama

Desert, northern Chile. Integrated Earth Data Applications (IEDA).

doi:10.1594/IEDA/100594. URL: http://dx.doi.org/10.1594/IEDA/100594

Cosentino, N. J., et al., (2016b), Major and selected trace element chemistry of ancient

gypsic soils in Atacama Desert, northern Chile. Integrated Earth Data Applications

(IEDA). doi:10.1594/IEDA/100593. URL:

http://dx.doi.org/10.1594/IEDA/100593

Dekens, P. S., A. C. Ravelo, and M. D. McCarthy (2007), Warm upwelling regions in

the Pliocene warm period. *Paleoceanography* **22**, PA3211.

Dunai, T. J., G. A. González López, and J. Juez-Larré (2005), Oligocene-Miocene age

of aridity in the Atacama Desert revealed by exposure dating of erosion-sensitive

landforms. *Geology* **33**, 321-324.

Ericksen, G. E. (1981), Geology and the origin of the Chilean nitrate deposits. *Geol.

Soc. Amer. Spec. Paper*, 1188, 37.

Ericksen, G. E. (1983), The Chilean Nitrate Deposits. American Scientist, vol. 70, no.

4, 366-374.

Evenstar, L. A., A. J. Hartley, F. M. Stuart, A. E. Mather, C. M. Rice, and G. Chong

(2009), Multiphase development of the Atacama Planation Surface recorded by

cosmogenic [3]He exposure ages: Implications for uplift and Cenozoic climate

change in western South America. *Geology* **37**, 27-30.

Evenstar, L. A., F. M. Stuart, A. J. Hartley, and B. Tattich (2015), Slow Cenozoic

uplift of the western Andean Cordillera indicated by cosmogenic [3]He in alluvial

boulders from the Pacific Planation Surface. *Geophys. Res. Lett.* **42**, 8448-8455.

Ewing, S. A., B. Sutter, J. Owen, K. Nishiizumi, W. Sharp, S. S. Cliff, K. Perry, W. Dietrich, C. P. McKay, and R. Amundson (2006), A threshold in soil formation at Earth's arid-hyperarid transition. *Geochimica et Cosmochimica Acta* **70**, 5293-5322.

Ewing, S. A., W. Yang, D. J. DePaolo, G. Michalski, C. Kendall, B. W. Stewart, M. Thiemens, and R. Amundson (2008), Non-biological fractionation of stable Ca isotopes in soils of the Atacama Desert, Chile. *Geochimica et Cosmochimica Acta* **72**, 1096-1110.

Farías, M., P. Cereceda, P. Osses, and R. Núnez (2005a), Spatial and temporal behavior of the stratocumulus cloud, fog producer in the coast of the Atacama desert (21º south lat., 70º west long.), during one month of winter and another of summer. *Investigaciones Geográficas, Boletín del Instituto de Geografía, UNAM* **56**, pp. 43-61.

Farías, M., R. Charrier, D. Comte, J. Martinod, and G. Hérail (2005b), Late Cenozoic deformation and uplift of the western flank of the Altiplano: Evidence from the depositional, tectonic, and geomorphologic evolution and shallow seismic activity (northern Chile at 19°30'S). *Tectonics* **24**, TC4001.

García, M., and G. Fuentes (2012), Carta Cuya, Regiones de Arica y Parinacota y de Tarapacá. Servicio Nacional de Geología y Minería, Carta Geológica de Chile, Serie Geología Básica 146: 80 p., 1 mapa escala 1:100.000. Santiago.

García, M., and G. Hérail (2005), Fault-related folding, drainage network evolution and valley incision during the Neogene in the Andean Precordillera of Northern Chile. *Geomorphology* **65**, 279-300.

García, M., R. Riquelme, M. Farías, G. Hérail, and R. Charrier (2011), Late Miocene-Holocene canyon incision in the western Altiplano, northern Chile: tectonic or climatic forcing? *Journal of the Geological Society* **168**, 1047-1060.

Garreaud, R. D., A. Molina, and M. Farias (2010), Andean uplift, ocean cooling and Atacama hyperaridity: A climate modeling perspective. *Earth and Planetary Science Letters* **292**, 39-50.

Garzione, C. N., P. Molnar, J. C. Libarkin, and B. J. MacFadden (2006), Rapid late Miocene rise of the Bolivian Altiplano: Evidence for removal of mantle lithosphere. Earth and Planetary Science Letters 241 (3–4), 543–556.

Ghosh, P., C. N. Garzione, and J. M. Eiler (2006), Rapid uplift of the Altiplano revealed through 13C-18O bonds in paleosol carbonates. Science 311, 511-515.

Gregory-Wodzicki, K. M. (2000), Uplift history of the Central and Northern Andes: a review. *Geological Society of America Bulletin* **112**, 1091–1105.

Hartley, A. J., and G. Chong (2002), Late Pliocene age for the Atacama Desert: Implications for the desertification of western South America. *Geology* **30** (1), 43-46.

Hartley, A. J., T. Sempere, and G. Wörner (2007), A comment on "Rapid late Miocene rise of the Bolivian Altiplano: Evidence for removal of mantle lithosphere" by C. N. Garzione et al. [Earth and Planetary Science Letters 241 (2006) 543-556]. Earth and Planetary Science Letters 259 (3-4), 625-629.

Hashizume, H., S. Xie, M. Fujiwara, M. Shiotani, T. Watanabe, Y. Tanimoto, W. T. Liu, and K. Takeuchi (2002), Direct Observations of Atmospheric Boundary Layer

Response to SST Variations Associated with Tropical Instability Waves over the Eastern Equatorial Pacific. Journal of Climate 15, 3379-3393.

Hoke, G. D., B. L. Isacks, T. E. Jordan, N. Blanco, A. J. Tomlinson, and J. Ramezani (2007), Geomorphic evidence for post-10 Ma uplift of the western flank of the central Andes, 18º30' – 22ºS. *Tectonics* **26**.

Horwitz, E. P., R. Chiarizia, and M. L. Dietz (1992), A novel strontium-selective extraction chromatographic resin. *Solvent Extraction & Ion Exchange* **10**, 313.

Houston, J., and A. J. Hartley (2003), The Central Andean west-slope rainshadow and its potential contribution to the origin of hyper-aridity in the Atacama Desert. *Inter- national Journal of Climatology* **23**, 1453–1464.

Insel, N., C. J. Poulsen, and T. A. Ehlers (2009), Influence of the Andes Mountains on South American moisture transport, convection, and precipitation. *Climate Dynamics*, 1-16.

Jordan, T. E., P. L. Nester, N. Blanco, G. D. Hoke, F. Dávila, and A. J. Tomlinson (2010), Uplift of the Altiplano-Puna plateau: A view from the west. *Tectonics* **29**, TC5007.

Jordan, T. E., N. E. Kirk-Lawlor, N. Blanco, J. A. Rech., and N. J. Cosentino (2014), Landscape modification in response to repeated onset of hyperarid paleoclimate states since 14 Ma, Atacama Desert, Chile. *Geological Society of America Bulletin* **126** (7-8), 1016-1046.

Jordan, T. E., N. J. Cosentino, and A. Jensen (2015), Pliocene-Quaternary Tectonic Subsidence of part of the Central Depression Forearc, 20-22°S, paper presented at XIV Congreso Geológico Chileno, La Serena, Chile.

Jordan, T. E., et al., (2016), Sr isotopic ratios of Holocene gypsum and anhydrite salt

deposits in Atacama Desert, northern Chile. Integrated Earth Data Applications

(IEDA). doi:10.1594/IEDA/100590. URL:

http://dx.doi.org/10.1594/IEDA/100590

Kar, N., C. N. Garzione, C. Jaramillo, T. Shanahan, V. Carlotto, A. Pullen, F. Moreno,

V. Anderson, E. Moreno, and J. Eiler (2016), Rapid regional surface uplift of the

northern Altiplano plateau revealed by multiproxy paleoclimate reconstruction.

Earth and Planetary Science Letters **447**, 33-47.

Kirk-Lawlor, N. E., T. E. Jordan, J. A. Rech, and S. B. Lehmann (2013), Late

Miocene to Early Pliocene paleohydrology and landscape evolution of northern

Chile, 19 to 20ºS. *Palaeogeography, Palaeoclimatology, Palaeoecology* **387**, 76-

90.

Kober, F., Ivy-Ochs, S., Schlunegger, F., Zeilinger, G., Kubik, P. W., Baur, H., and R.

Wieler (2006), Multiple cosmogenic nuclides and landscape evolution in the

Atacama Desert, northern Chile, paper presented at 2006 Philadelphia Annual

Meeting, Philadelphia, USA.

Lehmann, S. (2013), Climatic and tectonic implications of a mid-Miocene landscape:

Examination of the Tarapacá Pediplain, Atacama Desert, Chile, Msc thesis, Miami

University, Miami, Florida, USA.

Mack, G. H., W. C. James, and H. C. Monger (1993), Classification of paleosols.

Geological Society of America Bulletin **105**, 129-136.

Marquardt, R. C., S. N. Marinovic, and T. V. Muñoz (2008), Geología de las ciudades de Iquique y Alto Hospicio. *Carta Geológica de Chile, Serie Geológica Básica, 113. SERNAGEOMIN, Santiago*.

McFadden, L. D., S. G. Wells, and J. C. Dohrenwend (1986), Influences of Quaternary climatic changes on processes of soil development on desert loess deposits of the Cima volcanic field, California: Catena, v. 13, no. 4, p. 361-389.

Melnick, D. (2016), Rise of the central Andean coast by earthquakes straddling the Moho. *Nature Geoscience* **9**, 401-408.

Miller, K. G., G. S. Mountain, J. D. Wright, and J. V. Browning (2011), A 180-million-year record of sea level and ice volume variations from continental margin and deep-sea isotopic records. Oceanography 24, 40-53.

Mix, A. C., R. Tiedemann, and P. Blum (2003), Proceedings of the Ocean Drilling Program Initial Results. *Ocean Drilling Program, vol. 22, College Station, Tex.*

Mortimer, C. and N. Saric Rendic (1975), Cenozoic studies in northernmost Chile. *Geologische Rundschau* **64**, 395-420.

Muñoz, N., and P. Sepúlveda (1992), Estructuras compresivas con vergencia al oeste en el borde oriental de la Depresión Central, Norte de Chile (19º15'S). *Andean Geology* **19** (2), doi: 10.5027/andgeoV19n2-a07.

Naranjo, J. A., and R. Paskoff (1985), Evolución cenozoica del piedemonte andino en la Pampa del Tamarugal, norte de Chile (18–21ºS), paper presented at 4th Congreso Geológico Chileno, Dep. de Geocienc. Univ. Catolica del Norte, Antofagasta, Chile.

Nester, P. (2008), Basin and paleoclimate evolution of the Pampa del Tamarugal forearc valley, Atacama Desert, northern Chile, PhD thesis, Earth & Atmospheric Sciences, Cornell University, Ithaca, New York, USA.

Nester, P., and T. Jordan (2011), The Pampa del Tamarugal Forearc Basin in Northern Chile: The Interaction of Tectonics and Climate. *In Tectonics of Sedimentary Basins: Recent Advances (eds C. Busby and A. Azor)*, John Wiley & Sons, Ltd, Chichester, UK. doi: 10.1002/9781444347166.ch18.

Quezada, A., P. Vásquez, and F. Sepúlveda (2013), Soledad Formation: detailed mapping and radiometric ages, *in* Proceedings, International Geological Congress on the Southern Hemisphere (GEOSUR 2013): Viña del Mar, Chile, Bollettino di Geofisica teorica ed applicata, volume 54 (Supplement B), p. 242.

Rech, J. A., J. Quade, and W. S. Hart (2003), Isotopic evidence for the source of Ca and S in soil gypsum, anhydrite and calcite in the Atacama Desert, Chile. *Geochimica et Cosmochimica Acta* **67**, no. 4, 575-586.

Rech, J. A., B. S. Currie, G. Michalski, and A. M. Cowan (2006), Neogene climate change and uplift in the Atacama Desert, Chile. *Geology* 34(9), 761-764.

Regard, V., M. Saillard, J. Martinod, L. Audin, S. Carretier, K. Pedoja, R. Riquelme, P. Paredes, and G. Hérail (2010), Renewed uplift of the Central Andes Forearc revealed by coastal evolution during the Quaternary. *Earth and Planetary Science Letters* **297**, issues 1-2, 199-210.

Rosenthal, Y., C. H. Lear, D. W. Oppo, and B. K. Linsley (2006), Temperature and carbonate ion effects on Mg/Ca and Sr/Ca ratios in benthic foraminifera: Aragonite species Hoeglundina elegans. *Palaeoceanography* **21**, PA1007.

Sáez, A., L. Cabrera, M. Garcés, P. van den Bogaard, A. Jensen, and D. Gimeno (2012), The stratigraphic record of changing hyperaridity in the Atacama desert over the last 10 Ma. *Earth and Planetary Science Letters* **355-356**, 32-38.

Schildgen, T. F., K. V. Hodges, K. X. Whipple, M. S. Pringle, M. van Soest, and K. Cornell (2009), Late Cenozoic structural and tectonic development of the western margin of the central Andean Plateau in southwest Peru. *Tectonics* **28**, TC4007.

Schlunegger, F., G. Zeilinger, A. Kounov, F. Kober, and B. Hüsser (2006), Scale of relief growth in the forearc of the Andes of Northern Chile (Arica latitude, 18ºS). *Terra Nova* **18** (3), 217-223.

Schlunegger, F., F. Kober, G. Zeilinger, and R. von Rotz (2010), Sedimentology-based reconstructions of paleoclimate changes in the Central Andes in response to the uplift of the Andes, Arica region between 19 and 21° S latitude, northern Chile. International Journal of Earth Sciences 99 (1), 123-137.

Searl, A., and S. Rankin (1993), A preliminary petrographic study of the Chilean nitrates, Geol. Mag., 130(3), 319–333.

SERNAGEOMIN (2003) Mapa Geológico de Chile: versión digital. *Servicio Nacional de Geología y Minería, Publicación Geológica Digital*, No. 4 (CD-ROM, versión 1.0). Santiago.

Sillitoe, R. H., and E. H. McKee (1996), Age of supergene oxidation and enrichment in the Chilean porphyry copper province. *Economic Geology* **91** (1), 164-179.

Thouret, J. C., G. Wörner, Y. Gunnell, B. Singer, X. Zhang, and T. Souriot (2007), Geochronologic and stratigraphic constraints on canyon incision and Miocene

uplift of the Central Andes in Peru. *Earth and Planetary Science Letters* **263**, 151-166.

Veizer, J. (1989), Strontium isotopes in seawater through time. Ann. Rev. Earth Planet. Sci. 17, 141–167.

Veizer, J., D. Ala, K. Azmy, P. Bruckschen, D. Buhl, F. Bruhn, G. A. F. Carden, A. Diener, S. Ebneth, Y. Godderis, T. Jasper, C. Korte, F. Pawellek, O. G. Podlaha, and H. Strauss (1999), ^{87}Sr/^{86}Sr, δ13C and δ^{18}O evolution of Phanerozoic seawater. Chemical Geology 161, 59-88.

Victor, P., O. Oncken, and J. Glodny (2004), Uplift of the western Altiplano plateau: Evidence from the Precordillera between 20 and 21° S (northern Chile). *Tectonics* **23**, no. 4.

von Rotz, R, F. Schlunegger, F. Heller, and I. Villa (2005), Assessing the age of relief growth in the Andes of northern Chile: Magneto-polarity chronologies from Neogene continental sections. *Terra Nova* **17(5)**, 462-471.

Walfort, B., K. Hammerschmidt, and G. Wörner (1995), New Ar/Ar ages from Tertiary volcanics in the North chilean Andes (18°S): Implication for tectonic and magmatic evolution. *Terra Abstracts. Terra Nova* **7**, 354.

Wang, Y., S. Xie, H. Xu, and B. Wang (2004), Regional Model Simulations of Marine Boundary Layer Clouds over the Southeast Pacific off South America. Part I: Control Experiment. Monthly Weather Review 132, 274-296.

Wang, F., G. Michalski, J. Seo, D. E. Granger, N. Lifton, and M. Caffee (2015), Beryllium-10 concentrations in the hyper-arid soils in the Atacama Desert, Chile:

Implications for arid soil formation rates and El Niño driven changes in Pliocene precipitation. *Geochimica et Cosmochimica Acta* **160**, 227-242.

Zhang, C., Y. Wang, and K. Hamilton (2011), Improved Representation of Boundary Layer Clouds over the Southeast Pacific in ARW-WRF Using a Modified Tiedtke Cumulus Parameterization Scheme. Monthly Weather Review 139, 3489-3513.

CHAPTER 4

2D FINITE ELEMENT MODELING OF CLIMATE-CONTROLLED FLOW IN

SUBDUCTION CHANNELS: IMPLICATIONS FOR THE EVOLUTION OF

TOPOGRAPHY IN THE FOREARC OF THE CENTRAL ANDES

4.1 Abstract

Subduction channels have been recognized both in modern and fossil convergent

plate margins, yet their role on forearc surface elevation evolution has not been

sufficiently explored. We characterize the response of the offshore and onshore

forearc surface to 2D viscoelastic flow in a subduction channel with variable thickness

and viscosity. We find that for a given choice of these two parameters, the forearc

surface effectively reaches a steady-state configuration after ~6 myr. Subduction

channels 800-1100-m-thick with viscosities of 5-10 x10^{18} Pa s best fit the Central

Depression topography in northern Chile. The topographic relief of the Coastal

Cordillera with respect to the Central Depression, as well as the abrupt increase in

elevation of the coastal area, are not well reproduced by the models, suggesting that

other processes such as underplating or coseismic deformation create topographic

relief at a shorter spatial scale than subduction channel flow. To the east, the effects of

subduction channel flow wane and are not able to reproduce the topography of the

onshore forearc transition to the volcanic arc, which suggests that here surface

elevation change is dominated by processes acting to uplift the Altiplano Plateau. The

onset of hyperaridity in the Coastal Cordillera at ~25 Ma starved the trench and

subduction channel of sediments, causing a rise in shear stress at the subduction

channel top that triggered long-term 500-700 m of uplift in the Central Depression,

bringing this surface to its present elevation. Most of this uplift likely occurred during the first ~6 myr following the onset of hyperaridity. Less arid phases of 0.4-1-myr duration have taken place in the onshore forearc platform. These climate pulses may have translated into pulsed reductions of subduction channel viscosity by 3×10^{18} Pa s, which would have produced transient <350 m subsiding events; the surface would then uplift back to the long-term equilibrium elevation 4-4.5 myr after the end of the pulse. This scenario is consistent with known paleoelevation constraints in the Central Depression of northern Chile that suggest that most of the modern elevation of the western and eastern Central Depression has been accrued before the earliest Pliocene and before the Middle Miocene, respectively.

4.2 Introduction

Modern topography along trench-perpendicular transects of forearcs constitutes one of the main constraints for studies of the geologic processes acting at subduction zones. In the Nazca-South America plate system, forearcs share first-order topographic trends such as the existence of roughly flat onshore or slightly submerged platforms toeing the main Andes (Fig. 4-1). They also differ in second-order topographic trends such as the existence of coastal mountain ranges, as well as in the absolute elevations of the generally flat platforms (Fig. 4-1).

The erosive Nazca-South America plate interface has been characterized by long-term intraplate and interplate mass transfer processes such as subduction erosion [von Huene and Ranero, 2003] and underplating [Clift and Hartley, 2007]. This interface has been described as a subduction channel of finite width [Shreve and Cloos, 1986], and probably plays a dynamic role in accommodating various types of

mass flow between and within plates. The amount of sediment input to the trench, which is dependent on the mass flux from a continental surface by rivers, which is in turn linked to climate, has been proposed as a control on the interface rheology [Lamb and Davis, 2003].

The subduction channel model characterizes the interface between the subducting slab and the overlying plate in subduction zones as a finite width, variably consolidated sedimentary layer that in part coincides with a shear deformation zone between the two rigid plates [e.g. Shreve & Cloos, 1986; Vannucchi et al., 2012]. Two main lines of evidence support the existence of subduction channels: seismic data show a low-velocity channel-like layer bounded by surfaces of high reflectivity [e.g. Bangs et al., 2004; Calahorrano et al., 2008], while field studies of fossil subduction channels characterize them as shear fault zones that are formed of lower plate meta-ophiolites and upper plate crystalline materials [e.g. Bachmann et al., 2009], and prism slope, debris flows and accretionary prism deposits [e.g. Vannucchi et al., 2008].

Lamb and Davis [2003] suggested that not only does mountain building cause climate change, but that climate change may also be a driver of orogeny. They base this on the fact that the latitudinal band of maximum relief between the Peru-Chile trench and the crest of the Andes strongly coincides with the latitudinal extents of minimum annual mean coastal precipitation values (< 50 mm yr^{-1}) and of minimum trench sediment fill. The conceptual framework behind the proposed mechanism of mountain building is that the buoyancy stress contrast between the trench and the high Andes is balanced by the shear stress at the interface of the Nazca and South America plates. The sediment-starved sections of the trench lack layered turbidites that both smooth the top of the subducting plate and become water-rich lubricants of the interface between the upper and lower plates, and where that lubricant is lacking the shear stress rises to uncommonly high levels [Lamb & Davis, 2003]. Since the

provision of continental sediments to the trench is mostly accomplished by fluvial and glacial erosion and transport processes, and given that precipitation is the main climatic variable dictating the degree of fluvial and glacial action on the landscape, climate change controls the variability of trench sediment fill [Schweller et al., 1981]. Even if not made explicit, the idea that trench sediment fill influences the mechanical properties of the plate interface hundreds of kilometers from the trench implies some kind of sediment transport mechanism from the trench downdip along the plate interface, such as would be the case in the subduction channel model [e.g. Vannucchi et al., 2012].

The western flank of the Central Andes in northern Chile constitutes the quintessential forearc in a non-collisional convergent zone, comprised from west to east by a trench axis 6700-7600 m deep, a ~110-160 km wide offshore forearc whose easternmost ~50 km has a smooth slope reduction towards the coast, a coastal cliff that abruptly rises from sea level to 500-1200 m.a.s.l., a 30-60 km wide Coastal Cordillera with elevations < 1500 m.a.s.l., a 50-75 km wide Central Depression forearc basin at elevations of ~1000-2500 m.a.s.l., and the Precordillera western foothills of the Andes (Fig. 4-2a-b). We will discuss our results relative to three major forearc zones: an offshore forearc (from the trench to the coast), an onshore forearc platform (the Coastal Cordillera and the Central Depression), and an onshore forearc transition to the volcanic arc (Precordillera). Hyperaridity may have been the predominant long-term climatic state in the Coastal Cordillera throughout the Neogene [Dunai et al., 2005] and farther inland at elevations below 3000 m.a.s.l. since 12 ± 1 Ma, with 0.5-1 myr intervals of less arid conditions [Jordan et al., 2014].

Four main ideas have been put forward to explain cumulative long-term surface uplift of the onshore forearc platform of northern Chile: (a) plate convergence-driven interseismic compression in the upper plate [e.g. González et al., 2003], (b)

coseismic deformation during earthquakes originating at the plate interface below the Moho [Melnick, 2016], (c) underplating to the continental lithosphere of subduction erosion-derived sediments [von Huene and Ranero, 2003], and (d) higher shear stress along the plate interface due to a paucity of water-rich sediment in the trench [Lamb and Davis, 2003]. The last two mechanisms of surface elevation change in the onshore forearc platform involve the existence of a subduction channel along at least part of the plate interface.

Here, we experiment numerically with the mechanism of flow within a simplified subduction channel. We ask ourselves whether climate-controlled subduction channel flow explains surface elevation change in the offshore forearc and onshore forearc platform of the Nazca-South America plate system in the Central Andes. We first characterize the effects of subduction channel flow in concert with ideas of climate change-driven million-year-scale variability in continental sediment input to the trench as drivers of surface elevation change in subduction margins. We then test this proposed mechanism against modern forearc topography and available late Cenozoic surface paleoelevation constraints in northern Chile. In order to do so, we use the finite element method as a numerical tool to investigate the response of a free-surface land topography to deformation within a viscoelastic subduction channel.

4.3 Methods

We use the finite element method to model two-dimensional incompressible, Newtonian, isotropic, Stokes viscoelastic fluid flow in a several hundred meters-wide subduction channel at the interface between the upper rigid lithospheric plate and the subducting slab (Fig. 4-2c; Table 4-1). The former is characterized both in terms of

geometry and material properties based on density models [Tassara et al., 2006], while the latter is represented as a subduction velocity boundary condition applied at the bottom of the subduction channel. We perform a series of model runs keeping all geometrical and physical parameters constant except subduction channel thickness and subduction channel viscosity (Table 4-1). We use a Lagrangian description to follow the deformation of the atmosphere-land and seafloor free surfaces after each 10 kyr time step. The initial configuration is that of a flat atmosphere-land surface at sea level, and of a seafloor with a linear variation in depth from the trench axis to the coastline (Table 4-1).

The *Triangle* C program [Shewchuk, 1996] is used to generate $\sim 10^5$-element unstructured two-dimensional Delaunay triangular meshes for our two subdomains: the subduction channel and the upper plate (Fig. 4-2c). Re-meshing is performed after each time step, keeping the free surface configuration of the preceding time step. A horizontal resolution of ~250 m is achieved for the free surfaces. We use MILAMIN, a MATLAB-based finite element method mechanical solver [Dabrowski et al., 2008], modified to include the viscoelasticity terms. See sections C1-C6 in Appendix C for details on the finite element method formulation of viscoelasticity, the application of boundary conditions, a description of the mechanical solver, the general code structure, and a the main Matlab code from which all relevant functions are called.

We perform two series of numerical simulations: (1) 18 runs with varying subduction channel viscosity (η_{SC}) and thickness (h_{SC}) pairs (Table 4-1), both of which are constant throughout the runs; (2) starting with one channel viscosity-thickness pair ($\eta_{SC} = 7\times10^{18}$ Pa s; $h_{SC} = 500$ m), 8 runs to which 0.5-myr- or 1-myr-long pulses of higher or lower subduction channel viscosity are applied after 4 myr. These pulses migrate downdip along the channel with the velocity of relative subduction. In both cases, runs are performed for a total run time of 12 myr.

4.4 Results

Two-dimensional results are described as if geographically oriented like the Nazca-South America plate boundary system of northern Chile and the eastern Pacific Ocean region: west on the left, east on the right, and plate subducting from left to right (Fig. 4-2). Horizontal distance is measured from the trench axis (Fig. 4-2b-c). For all eighteen 12-myr-long simulations with constant-in-time channel viscosity, topographic relief from the trench to the eastern model boundary grows with increasing subduction channel viscosity and with decreasing subduction channel thickness (Fig. 4-3a). The topographic relief is due both to net surface uplift and net surface subsidence east and west, respectively, of a hinge located 150-240 km from the trench (Fig. 4-3a).

The integrated shear force along the subduction channel roof has a positive linear correlation with subduction channel viscosity (Fig. 4-4a) and an inverse correlation with subduction channel thickness (Fig. 4-4b). As was stated above, subduction channel viscosity and thickness also correlate positively and inversely, respectively, with topographic relief between the trench and high Andes (Fig. 4-3a).

When measured from each simulation's end-of-run coastline position, the modeled elevation at the center of the Central Depression (65 km from the coast) varies between 1000 and 3500 m.a.s.l. for a range in subduction channel viscosities of 3-20 x10^{18} Pa s and in subduction channel thickness of 350-1100 m (Fig. 4-3b; Fig. 4-5a; Table 4-1). The simulations whose elevations west of 80 km from the coastline are closest to DEM data are those with 800-1100-m-thick subduction channels with viscosities in the range of 5-10 x10^{18} Pa s (Fig. 4-3b; Fig. 4-5b). The 350-500-m-thick

subduction channels show good accordance with DEM data only for a viscosity of 3 x10^{18} Pa s, the lowest in the range considered in this study (Fig. 4-3b; Fig. 4-5b). None of the simulations achieves the high gradient of elevation change from sea level characteristic of the westernmost Coastal Cordillera (Fig. 4-3b). Also, six runs show an eastward reduction in elevation east of 85-100 km from the coast (Fig. 4-3b).

The evolution in time of the coastline position depends on the choice of subduction channel parameters, as well as on the choice of geometrical initial conditions, as will become apparent in the following paragraph (Fig. 4-6). For the set of model runs with 1100-m-thick subduction channels, in all cases coastline migration reaches a nearly steady posiiton after at most 5 myr of run time: the two simulations with lowest subduction channel viscosities show a >8.5-myr-long phase of stability, while the higher viscosity simulations show a ≥7-myr-long phase of slow ~0.8 km myr^{-1} trenchward migration (Fig. 4-6a). For the most part, the higher the viscosity of the subduction channel, the farther to the west is the final coastline position (Fig. 4-6a).

The rise in inland topography occurs rapidly: more than 80% of the change in surface elevation is achieved during the first 17% of the total run time (Fig. 4-7). This is indicative of the system evolving towards a steady-state bathymetric/topographic configuration from initial conditions that are far from it, particularly at positions far from the trench. After 6 myr of run time, surface elevation change rates are close to zero, effectively reaching bathymetric/topographic steady-state (Fig. 4-7).

The effect on surface elevation of applying pulses of subduction channel material with different viscosity is transient (Fig. 4-8). For a packet of a given viscosity, the maximum continental surface elevation change is similar throughout the onshore forearc platform, and is achieved first at locations close to the coastline: 1.3-2.2 myr after the end of the event for the case of the 1-myr-long pulses, and 1.7-2.5

myr after the end of the event for the case of the 0.5-myr-long pulses (Fig. 4-8).
Between 85-90% of the transient effect of subduction channel pulses on surface
elevation between 35 and 95 km from the end-of-run coastline positions is lost by 4
myr after the end of the 1-myr-long pulses, and after 4.5 myr after the end of the 0.5-
myr-long pulses (Fig. 4-8a-c). Closer to the coast, this effect is shorter-lived: 85% of it
is lost after 2.6 myr (Fig. 4-8d). These pulses also have a transient effect on coastline
migration: 1-myr-long higher viscosity pulses produce trenchward migration of the
coastline, while lower viscosity ones produce migration of the coastline toward the arc
(Fig. 4-6b). In all cases, the maximum coastline deviation is reached 2 myr after the
start of the pulse (Fig. 4-6b).

4.5 Discussion

Mass removal processes such as tectonic erosion of the upper plate close to the
trench [e.g. von Huene and Ranero, 2003; Vannucchi et al., 2012] coupled with mass
accretion processes such as underplating beneath the coastal region [e.g. Clift and
Hartley, 2007; Vannucchi et al., 2012] have been put forward as mechanisms to
explain coupled, long-term net surface subsidence of the offshore forearc and uplift of
the westernmost onshore forearc platform west of the Central Andes. However, no
geodynamic mechanism has been proposed as of yet to explain this behavior at the
scale of the entire trench-prependicular extent of the forearc, including the central and
eastern onshore forearc platform. We here show that flow within a subduction channel
is a numerically plausible process that explains this dual behavior at that scale.

The mechanical role of the subduction channel is as a buffer to the stress applied
by the subducting slab to the upper plate, since a fraction of this energy is consumed in

straining the subduction channel fill. The higher the viscosity of the subduction channel, the higher is the resistance to flow of the materials within the channel. This causes a greater portion of the force applied by the subducting slab to the subduction channel bottom to be transmitted through the subduction channel to the upper plate (Fig. 4-4a). Also, the narrower the subduction channel, the smaller the portion of the force applied by the subducting slab that can be transformed into strain of the subduction channel fill, and thus the higher the force that is transmitted to the upper plate (Fig. 4-4b). The calculated shear forces integrated along the subduction channel top after 12 myr of run time are in the range of ~2-9 x10^{12} N per unit length in the direction parallel to the trench. Lamb and Davis [2003] estimated that the average shear stresses at the plate interface that are required to balance the buoyancy stress contrast between the trench and high Andes between 5-45ºS at 10-50 MPa, which for the length of our modeled plate interface translates to 4-20 x10^{12} N per unit length in the direction parallel to the trench. This is in line with our own estimations.

All runs show an eastern topographic feature characterized by a positive bulge and a negative trough, each ~500 m above the regional elevation and with an 80 km wavelength, that cannot be explained by fixed geometrical model parameters such as Moho topography, model boundary effects and subduction channel depth (Fig. 4-3a; see section C7 and Fig. C1 in Appendix C). Instead, it seems to be a robust feature that arises from the dynamics of subduction channel flow, and may indicate the waning effect of subduction channel flow as we go east (section C7 and Fig. C1 in Appendix C). Isacks [1988] defined the western flank of the Altiplano Plateau as a crustal-scale monoclinal fold, which dominated relief production of the Altiplano Plateau with respect to the onshore forearc platform. Jordan et al. [2010] showed that the downdip monoclinal hinge between 19.5-21.5ºS is located at an average of 95 km from the coast, on the eastern onshore forearc platform (Fig. 4-2a-b). For all the model runs the

bump/trough topographic feature lies greater than 80 km east of the coastline (Fig. 4-3b). We conclude that our model cannot explain uplift of the easternmost Central Depression and of the onshore forearc transition to the volcanic arc. This is due to the fact that other processes unrelated to the dynamics of the subduction channel are superimposed east of the downdip monoclinal fold hinge.

Only a few studies have placed constraints on the absolute surface elevation evolution of the onshore forearc platform in northern Chile during the Neogene. The Sr isotopic ratio of recent accumulations of calcium sulfate on the landscapes of the Coastal Cordillera and Central Depression of northern Chile show a bimodal distribution in elevation, with high values between 200-250 m.a.s.l. and 1050-1100 m.a.s.l. [Chapter 2; i.e. Cosentino et al., 2015]. This was exploited to obtain paleoelevation constraints from $^{87}Sr/^{86}Sr$ of Pliocene and Quaternary calcium sulfates of the Central Depression and westernmost Coastal Cordillera between 19.5-21.7ºS [Chapter 3; i.e. Cosentino and Jordan, 2017]. They deduced that more than 70% of the present elevation of the westernmost onshore forearc platform (i.e. the western Coastal Cordillera) was achieved prior to the earliest Pliocene, while more than 45% of the present elevation of the eastern onshore forearc platform (i.e. the Central Depression) was also achieved prior to the earliest Pliocene [Chapter 3; i.e. Cosentino and Jordan, 2017]. Evenstar et al. [2015] used the altitude control on the production rate of cosmogenic nuclides to conclude that more than 50% of the current easternmost onshore forearc platform (i.e. the eastern Central Depression) elevation at 19.6ºS was achieved prior to 13.4 Ma. Furthermore, based on facies of the late Oligocene continental Azapa Formation in the Central Depression of northern Chile, García et al. [2011] deduced that this paleosurface had to be above sea level at 27 Ma, and the 500-m-thickness of the unit implies that the horizon was at least 500 m above sea level.

Though pertaining to larger time and spatial scales, Lamb and Davis [2003] proposed that the onset of hyperaridity triggered sediment starvation at the trench and associated high shear stresses at the plate interface, which would in turn produce uplift of the Andes. Jordan et al. [2014] used the landforms and deposits of alluvial fans, including soils and their mineralogical and chemical compositions, to conclude that hyperaridity has been the mean climatological state in the Atacama Desert since 12 ± 1 Ma. Nonetheless, the onset of hyperaridity may precede the age recorded in the basin fill beyond 12 ± 1 Ma [Sillitoe and McKee, 1996; Dunai et al., 2005; Arancibia et al., 2006]. Dunai et al. [2005] date the onset of hyperaridity in northern's Chile Coastal Cordillera at ~25 Ma based on cosmogenic nuclide exposure dating.

Our numerical experiments suggest that 0.5- to 1-myr-long pulses of material of different viscosity migrating down the subduction channel have a transient effect on surface elevation (Fig. 4-8). The magnitude of the maximum surface elevation deviations with respect to the "no pulse" constant flow model runs are similar throughout the inland forearc (Fig. 4-8). Close to the final coastline position, these maximum deviations are reached 1.3 myr after the perturbation ceased (Fig. 4-8d), while farther inland they are reached after 2.2 myr elapse (Fig. 4-8a). While this timing is not dependent on the magnitude of the viscosity contrast between the pulse and the long-term subduction channel material, the magnitude of the surface elevation deviation is: for a ± 1 (2; 3) x10^{18} Pa s contrast in subduction channel viscosity, surface elevation 65 km inland from the final coastline position changes ± ~110 (~220; ~340) m (Fig. 4-8b).

Indeed cycles of hyperarid and less arid climate phases have been proposed for the Central Depression (21.5ºS) since 12 ± 1 Ma [Jordan et al., 2014; Wang et al., 2015]. After a prolonged period of hyperaridity starting at ~11 Ma and ending at ~5.5 Ma, Jordan et al. [2014] identified 0.4- to 1-myr-long arid interruptions to hyperaridity

in the Central Depression. However, this section of the forearc basin surface may have drained to the Pacific Ocean only since the incision of the Loa River, and not before. This incision started sometime after ~6 Ma [Hoke et al., 2007], so that no causal relationship can be established between arid/hyperarid cycles in the Central Depression at 21.5ºS and sediment trench fill prior to ~6 Ma. The same holds true for the endorheic section of the Central Depression between 19.5-21.5ºS, since even beyond ~6 Ma. In these cases, it is climate variability in the Coastal Cordillera that may effectively dictate sediment trench fill variability.

A scenario that is consistent with our numerical results as well as with the aforementioned paleoelevation constraints for northern Chile is the following: (i) At ~26 Ma the paleosurface that corresponds to the Azapa Formation – Oxaya Formation discontinuity was at an elevation of at least 500 m.a.s.l. in the central onshore forearc platform (i.e. western Central Depression). (ii) At ~25 Ma the Coastal Cordillera suffered a reduction in precipitation towards hyperarid conditions, triggering sediment starvation at the trench and a reduction in sediment transport along the subduction channel flow, a condition which would prevail as the mean climatic state to the present. (iii) Flow within a 800-1100-m-thick subduction channel with viscosities in the range of 5-10 x10^{18} Pa s has taken place for the most part since shortly after ~25 Ma, causing long-wavelength, long-term net uplift of the eastern onshore forearc platform (i.e. Central Depression) to its present elevation no later than ~19 Ma. (iv) Short-duration less arid paleoclimate states may have recurred in the Coastal Cordillera several times since ~25 Ma, each one instigating subsidence of the onshore forearc platform after a short delay, followed by uplift during approximately the same amount of time, effectively taking the surface back to its long-term equilibrium elevation. (v) These transient episodes of subsidence and subsequent uplift placed the easternmost onshore forearc platform at ~900 m.a.s.l. or above by 13.4 Ma. (vi) These

same climatic variations episodes could not have produced more than 500 m of net uplift in the Central Depression and more than 300 m of uplift in the Coastal Cordillera since the earliest Pliocene. These last two conditions place bounds on the viscosity contrast between the long-term materials flowing in the subduction channel during Coastal Cordillera arid and hyperarid phases: assuming constant subduction channel thickness, less arid deviations from the hyperarid mean state should correspond to viscosities in the range of 2-7 $\times 10^{18}$ Pa s.

None of the model runs reproduces either the abrupt elevation gain at the coastal zone, whose geomorphic expression is a coastal escarpment, nor the western Coastal Cordillera elevation (Fig. 4-3b). This suggests that subduction channel flow should be considered a long-wavelength, whole-block deformation process, and that other, more local mechanisms such as the aforementioned coseismic deformation and coastal underplating are required to explain short-wavelength coastal uplift.

Pulses of introduction of weaker (i.e. lower viscosity) material into the trench end of subduction channels have a transient effect on landward coastal migration (Fig. 4-6b). Time-variable properties of the subduction channel could explain the non-steady-state retreat of the Central Chilean and Peruvian coastlines; the validity and timing of that retreat is debated [Clift and Hartley, 2007a, b; Encinas and Finger, 2007]. We propose that pulses of more sediment coming into the trench within a general state of sediment-starved conditions may explain non-steady-state retreat of the coastline.

In order to better simulate the effects of subduction channel flow on surface elevation of erosive forearcs, it is necessary to incorporate into these numerical models mass removal and mass accretion mechanisms such as frontal erosion and underplating. These mechanisms of exchange of mass between the subducting plate and the upper plate imply a more dynamic concept of subduction channels, and may

have important consequences on forearc surface elevation, both in terms of magnitude and short- and long-wavelength shape. The relationship between shallow subduction channel flow and the seismogenic zone is also a matter of debate, especially in terms of the flow mechanisms that dominate in the locked zone. Appropriate flow parameters that are representative of the seismogenic zone may influence short-scale surface elevation in the coastal region, as proposed previously by Melnick [2016].

4.6 Conclusions

This study demonstrates that viscoelastic flow in a subduction channel is a numerically plausible geodynamic mechanism to explain coupled long-wavelength offshore forearc subsidence and onshore forearc platform uplift in subduction margins. Subduction channels with materials with viscosities several orders of magnitude lower than the overlying plate act as buffers of the shear force applied by the subducting slab to the upper plate: part of this energy is consumed in shearing the subduction channel materials, reducing the energy available to generate topographic relief between the trench and the high Andes. One important control on the rheology of the subduction channel that is explored here is continental forearc climate: more arid conditions favor less sediments reaching the trench and entering the subduction channel, thus raising the subduction channel viscosity.

This mechanism may be directly applicable to explain broad facets of the history of the northern Chile forearc surface in the Central Andes. The modern elevation of the eastern onshore forearc platform (i.e. Central Depression) is best fit by long-term flow in an 800-1100-m-thick subduction channel with viscosities in the range of 5-10 $x10^{18}$ Pa s during at least 6 myr. The abrupt elevation increase at the coast, whose

geomorphological expression is the Coastal Escarpment, is not well reproduced by the models. Other mechanisms producing topography at a shorter scale, such as underplating under the coast or plate interface coseismic deformation, must work in tandem with subduction channel flow. The topographic role of the subduction channel wanes towards the east, and cannot explain topography to the east of 80 km from the coastline, where the onshore forearc platform uplifts in response mostly to the driving forces uplifting the Altiplano Plateau.

The onset of hyperaridity in the Coastal Cordillera at ~25 Ma has likely triggered net 500-700 m of uplift of the Central Depression to its modern elevation. Most of this uplift was concentrated during the first 6 myr since the onset of hyperaridity in the Coastal Cordillera. This agrees well with paleoelevation constraints that place most of the western and central Central Depression uplift prior to the earliest Pliocene, and most of the eastern Central Depression uplift prior to mid-Miocene times.

Hyperaridity has been the mean climatic state in the Central Depression since at least the late Middle Miocene, with 0.4-1-myr-long less arid phases. Such climate cycles have arguably also operated in the Coastal Cordillera. Where surficial sediment flow paths exist between either the Coastal Cordillera or the inland forearc basin and the Pacific Ocean, these phases of less aridity translated to more sediment flow into the trench. Our models show that 1-myr-long pulses of less viscous subduction channels produce transient subsidence, with magnitudes that are similar across the onshore forearc platform, but that are reached earlier the closer to the coast as the pulse migrates downdip along the plate interface. Model results suggest that in order not to contradict the paleoelevation constraints discussed above, and assuming constant-in-time subduction channel thickness, less arid deviations from the hyperarid mean state should have translated to viscosities in the range of 2-7 $\times 10^{18}$ Pa s. Also,

pulses of introduction of weaker (i.e. lower viscosity) material into the trench end of subduction channels have a transient effect on landward coastal migration, which may contribute to the non-steady-state retreat of the coastlines in Chile and Peru.

We suggest that the next generation of subduction channel models should incorporate mass removal/accretion mechanisms between the channel and the upper plate, as well as differential flow parameters for the seismogenic section of the interface. This should capture the more dynamic aspects of subduction channel flow, and should enable us to test the hypothesis that either underplating or coseismic deformation acts to produce short-scale topographic relief at the western Coastal Cordillera.

4.7 Acknowledgements

4.8 Tables

Table 4-1. Geometrical and material model parameters, and boundary conditions.					
		Parameter	**Value/ Range**	**Comments**	**Reference**
Geometrical	*Fixed*	Subduction angle (sφ, °)	23	Constant along the downdip direction	David et al. [2002]
		Subduction velocity (v$_s$, mm yr^{-1})	71	Orthogonal	David et al.

147

		Parameter	Value	Notes	Reference
				component of convergence rate	[2002]
		Initial trench depth (h_{ti}, km)	-7.45	20-21ºS SRTM-90 average	-
		Initial coastline (x_{ci}, km)	115	From trench	-
		Eastern domain limit (x_{el}, km)	400	From trench	-
		Initial inland topography (y_{csi}, m)	0	Everywhere	-
		Depth domain limit (y_{dl}, km)	100	-	-
		MOHO	-	-	Tassara et al. [2006]
		Upper crust-lower crust discontinuity	-	-	Tassara et al. [2006]
	Variable	Subduction channel thickness (h_{sc}, m)	350-1100	Constant along the downdip direction	-
Material parameters		Subduction channel viscosity (η_{SC}, x10^{18} Pa s)	3-20	Homogeneous in space	-
	Fixed	Sea water density (ρ_w, kg m^{-3})	1020	-	-
		Subduction channel density (ρ_{SC}, kg m^{-3})	2200	Homogeneous in space and constant in time	Shreve and Cloos [1986]
		Upper crust density (ρ_{UC}, kg m^{-3})	2700	-	Tassara et al. [2006]
		Lower crust density (ρ_{LC}, kg m^{-3})	3100	-	Tassara et al. [2006]
		Lithospheric mantle density (ρ_{LM}, kg m^{-3})	3240	-	Tassara et al. [2006]
		Subduction channel shear modulus (G_{SC}, x10^9 Pa)	10	-	Dinther et al. [2013]
		Upper crust shear modulus (G_{UC}, x10^9 Pa)	25	-	Dinther et al. [2013]
		Lower crust shear modulus (G_{LC}, x10^9 Pa)	25	-	Dinther et al. [2013]
		Lithospheric mantle shear modulus (G_{LM}, x10^9 Pa)	67	-	Dinther et al. [2013]
		Upper crust viscosity (η_{UC}, x10^{21} Pa s)	82	-	Roy and Roydan [2000]
		Lower crust viscosity (η_{LC}, x10^{21} Pa s)	26	-	Roy and Roydan [2000]
		Lithospheric mantle viscosity (η_{LM}, x10^{21} Pa s)	1.7	-	Roy and Roydan [2000]
Fixed		Time step (yr)	10,000	-	-
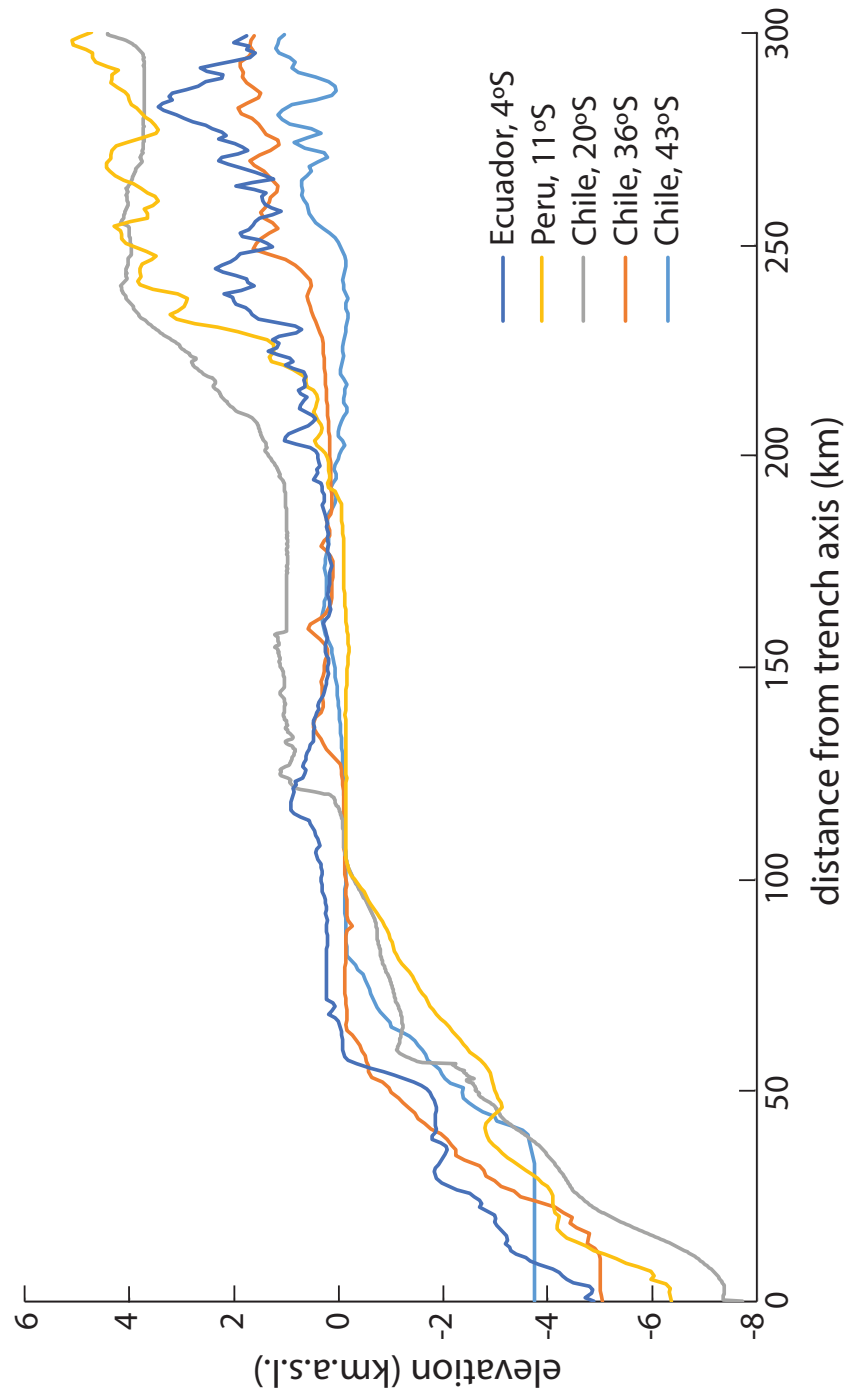
Figure 4-1. Forearc topography along trench-perpendicular transects in the Nazca-South America plate system.

A

Altiplano Plateau

Western Cordillera

Precordillera

Central Depression

Coastal Cordillera

IQUIQUE

trench

20°
21°S
71°W   70°   69°

5000
3000
2000
1500
1000
500
200
0
-100
-200
-500
-1000
-2000
-4000
-7000

m.a.s.l.

△ western downdip monocline fold axes [Jordan et al., 2010]

┇ inferred western downdip monoclinal hinge [Jordan et al., 2010]

B

Western
Cordillera

Coastal   Central   Precord.   Altiplano Plateau
Cordillera   Depression   4055 m.a.s.l.
                 1544 m.a.s.l.   300 km
sea level   △
                                                         200 km
                        100 km

-7580 m.a.s.l.
0 km   sea level

C

$F = \rho_w gh(x)$ x_{ci} $F = 0$ UC (η_{UC}, ρ_{UC}, G_{UC}) x_{el}

h_{ti} y_{csi}

$s\varphi$ UC-LC   ↓ g

y ⌐ x LC (η_{LC}, ρ_{LC}, G_{LC})

UC   Moho $v_x = 0$

v_s SC (η_{SC}, ρ_{SC}, G_{SC}) v_s LM (η_{LM}, ρ_{LM}, G_{LM})

v_s h_{sc} y_{dl}

h_{sc} SC (η_{SC}, ρ_{SC}, G_{SC})   UM $v_y = 0$
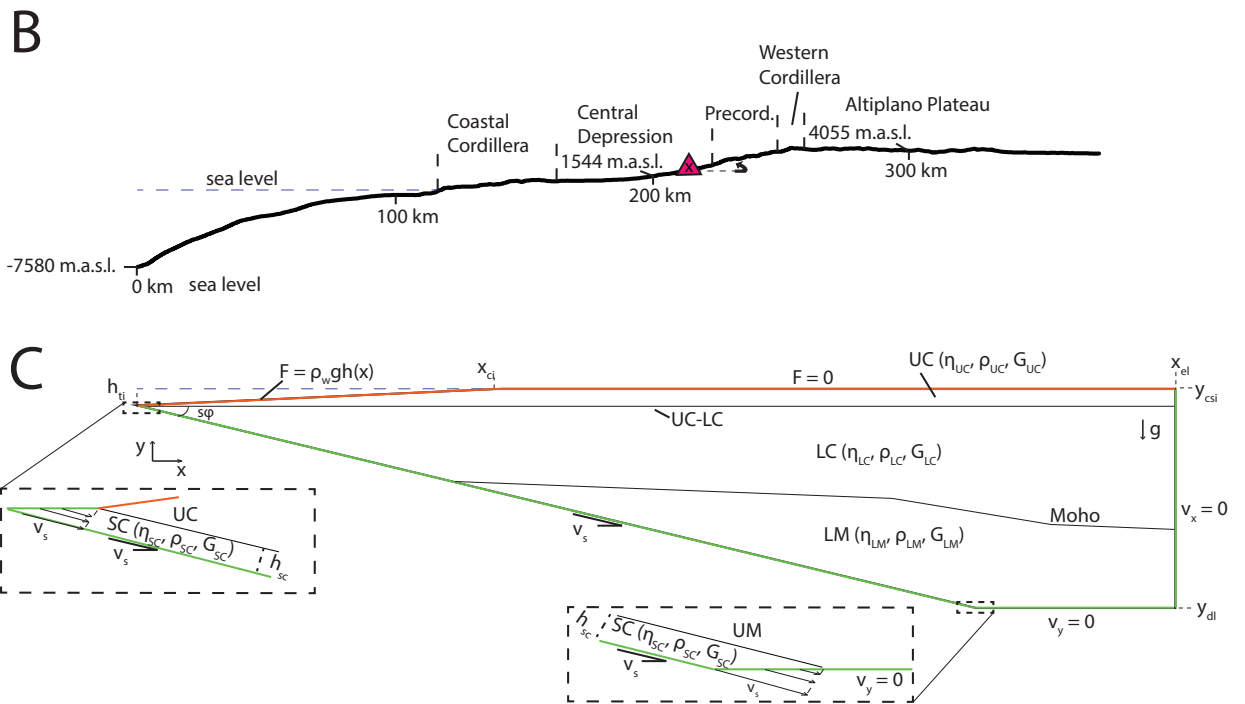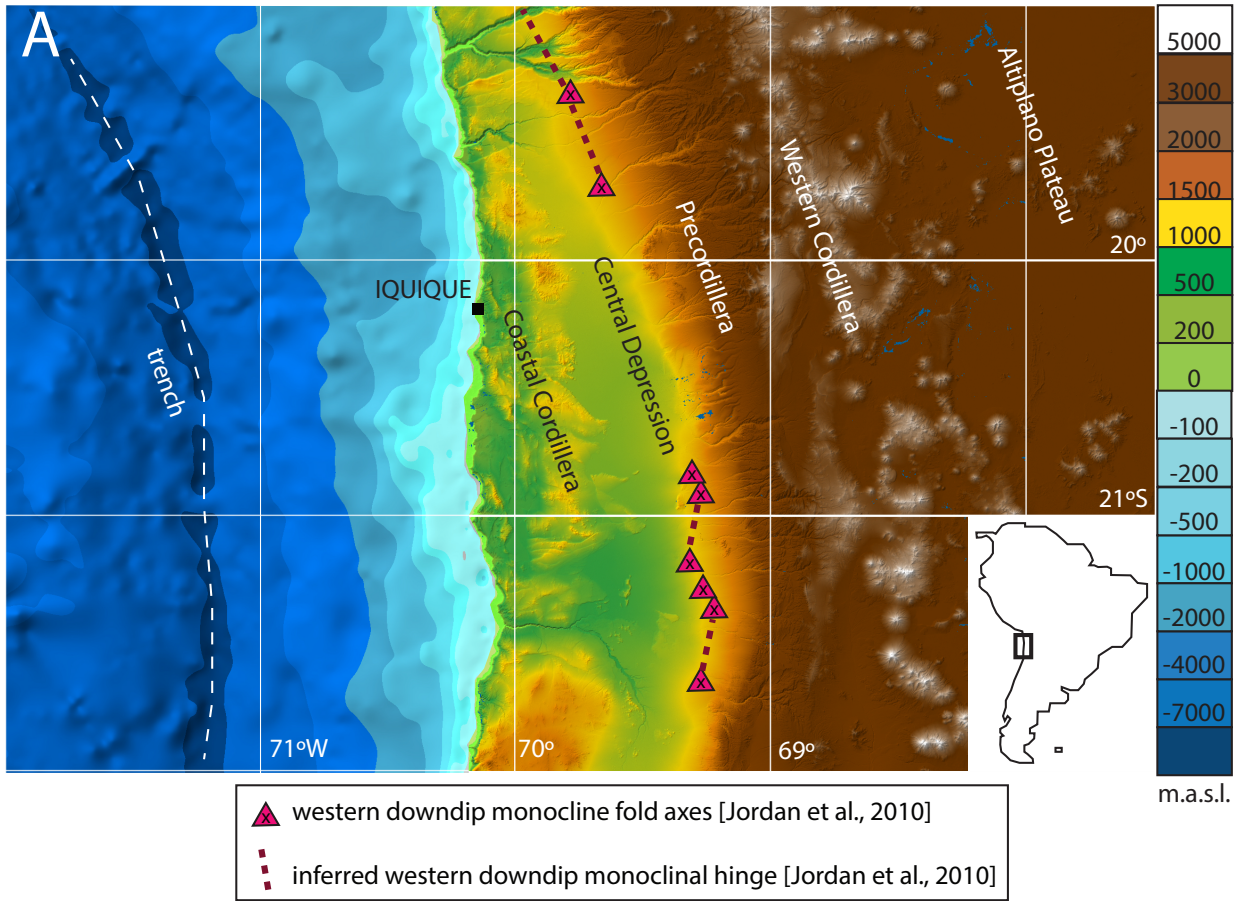
v_s

v_s $v_y = 0$

Figure 4-2. (see next page)

150

Figure 4-2. (a) The Nazca-South America forearc of the Central Andes of northern Chile. The western downdip hinge of the monocline defined according to Jordan et al. [2010]. Bathymetry based on ETOPO1 and topography on SRTM-90. (b) The DEM bathymetry and topography of the Altiplano Plateau, western flank of the Central Andes and offshore forearc consist of the average surface and seafloor elevation for 19.53ºS, 20.00ºS, 20.50ºS, 21.00ºS and 21.44ºS (SRTM-90). The start (i.e. 0 km) of each of these five transects corresponds to the deepest seafloor location at their latitude. (c) The geometry of the modeled domain is defined by the subduction angle ($s\varphi$), domain depth limit (y_{dl}), domain eastern limit (x_{el}), initial coastal position (x_{ci}), initial continental surface topography (y_{csi}), initial trench depth (h_{ti}), subduction channel thickness (h_{sc}) and upper crust-lower crust boundary and Moho discontinuity (based on Tassara et al. [2006]). Physical parameters that define the modeled materials in each subdomain are the density (ρ), viscosity (η) and shear modulus (G). Applied boundary conditions are either essential (fixed velocity; green domain boundaries) or natural (applied forces; orange domain boundaries). UC: upper crust, LC: lower crust, LM: lithospheric mantle, SC: subduction channel, UC-LC: upper crust-lower crust boundary; v_s: relative subduction rate.
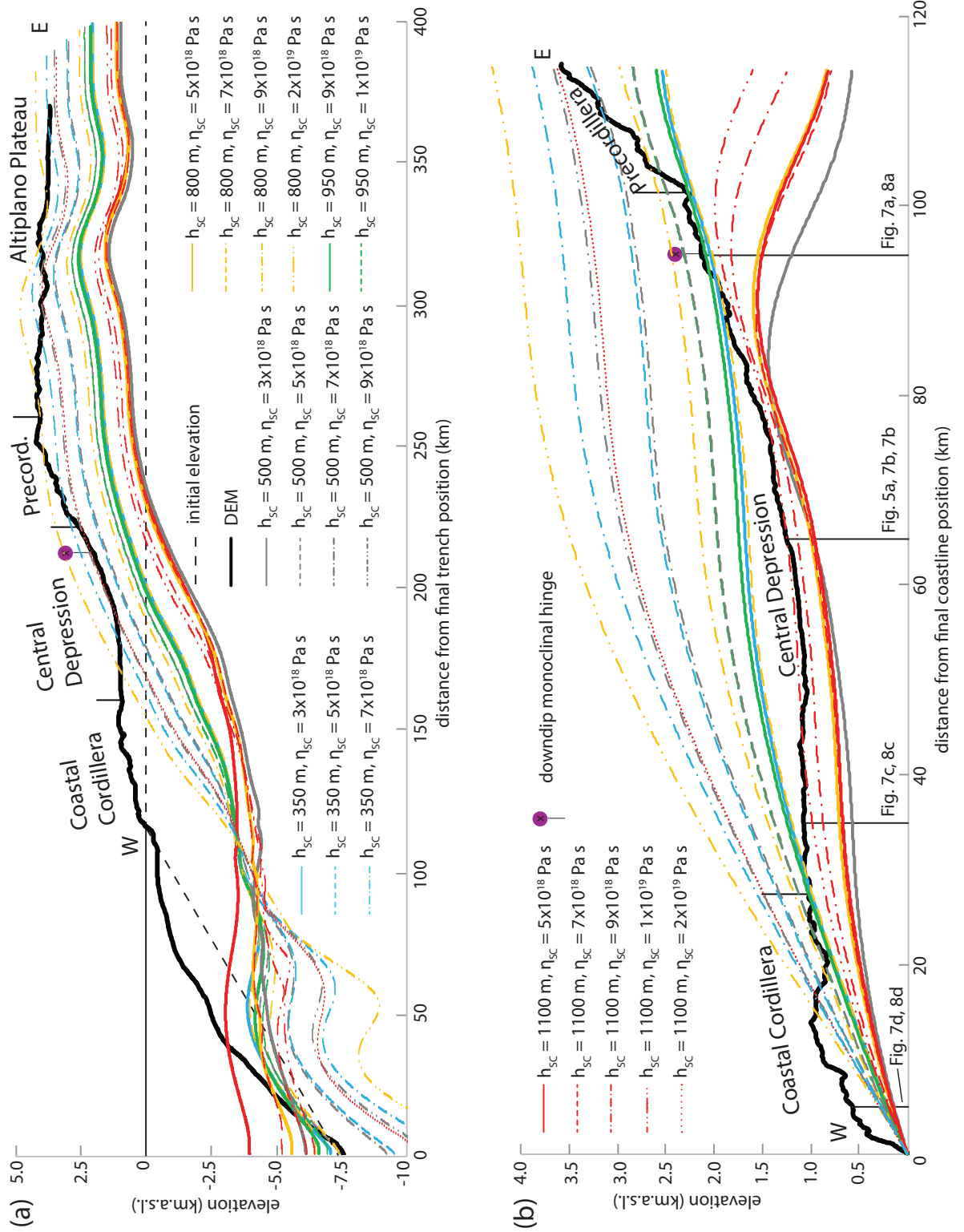
Figure 4-3. (see next page)

Figure 4-3. Final bathymetry/topography of 12-myr long simulations spanning subduction channel thicknesses of 350-1100 meters and constant, homogeneous subduction channel viscosities of $3x10^{18}$-$1x10^{19}$ Pa s. Horizontal distance is measured (a) with respect to the modern trench position (DEM curve) or to each end-of-run trench position (model curves), and (b) with respect to the modern coastline position (DEM curve) or to each end-of-run coastline position (model curves). The DEM curve consists of the average of elevations along trench-perpendicular profiles at 19.53ºS, 20.00ºS, 20.50ºS, 21.00ºS and 21.44ºS (SRTM-90). The downdip monoclinal hinge is defined as the average hinge position between 20.75ºS and 21.75ºS [Jordan et al., 2010]. See Table 4-1 for simulation parameters.
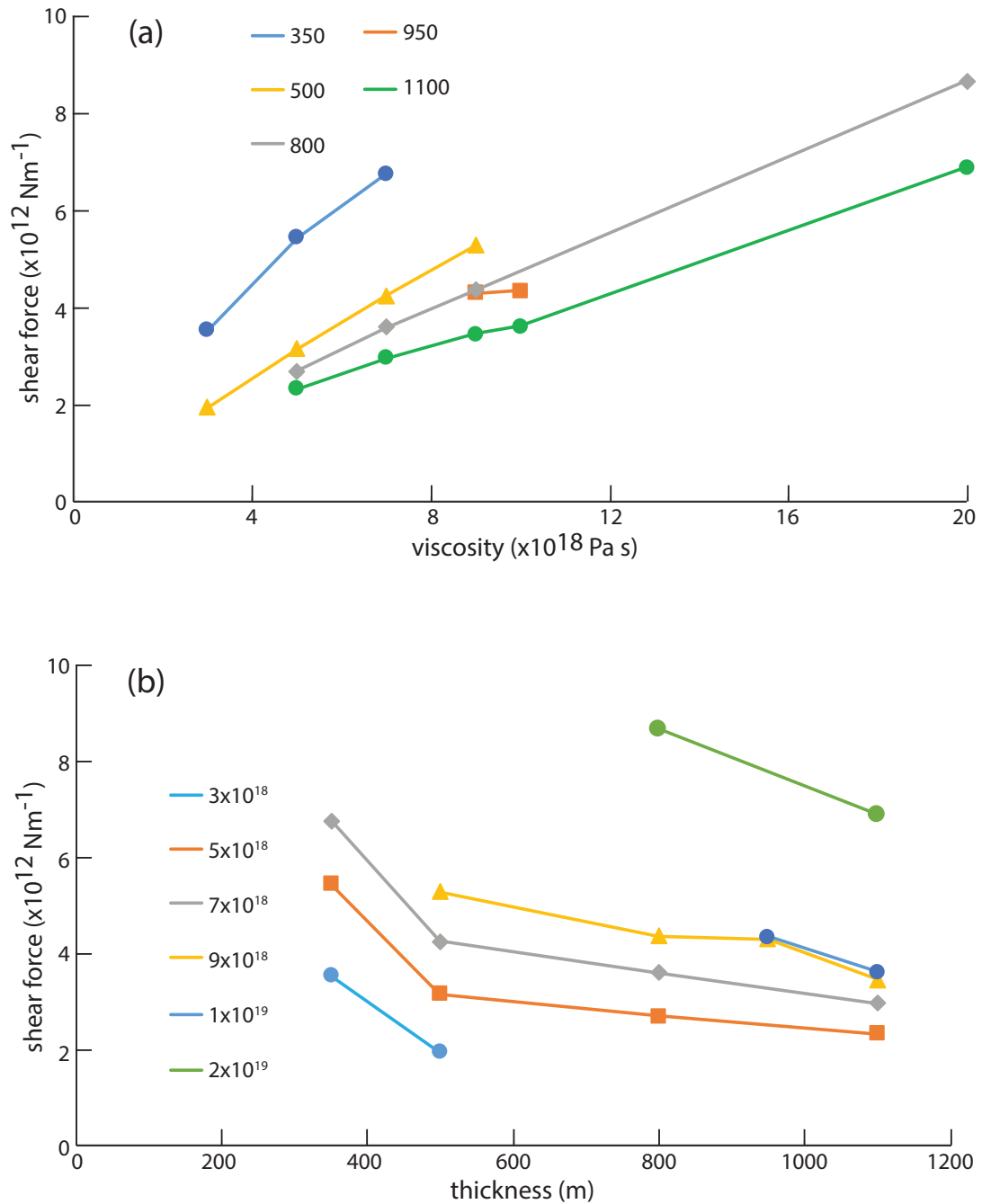
Figure 4-4. Shear force per unit length in the direction parallel to the trench, integrated along the entire subduction channel roof surface after 12 myr of run time, (a) versus subduction channel viscosity, color-coded by subduction channel thickness (units in m), and (b) versus subduction channel thickness, color-coded by subduction channel viscosity (units in Pa s). See Table 4-1 for other model parameters.
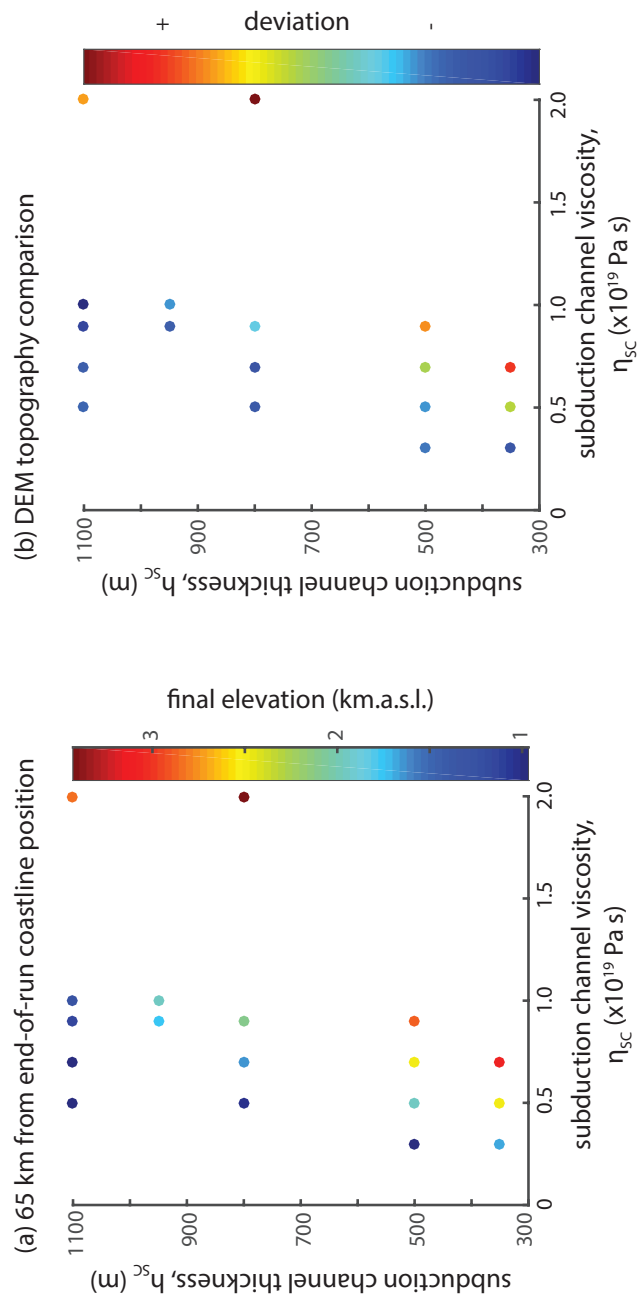
Figure 4-5. (a) Final, cumulative elevations at 65 km to the east of the final coastline position of each simulation, for simulations with different pairs of subduction channel thickness (h$_{SC}$) and viscosity (η_{SC}). (b) Comparison of modeled final, cumulative topography with DEM topography, between 0 and 80 km to the east of the final coastline position. In this case, the sum of differences in topography between each model's final output and DEM is calculated, and then normalized with respect to the model with the highest sum. See Table 1 for other simulation parameters. DEM topography is based on the average values for trench-perpendicular profiles at 19.53ºS, 20.00ºS, 20.50ºS, 21.00ºS and 21.44ºS (SRTM-90).
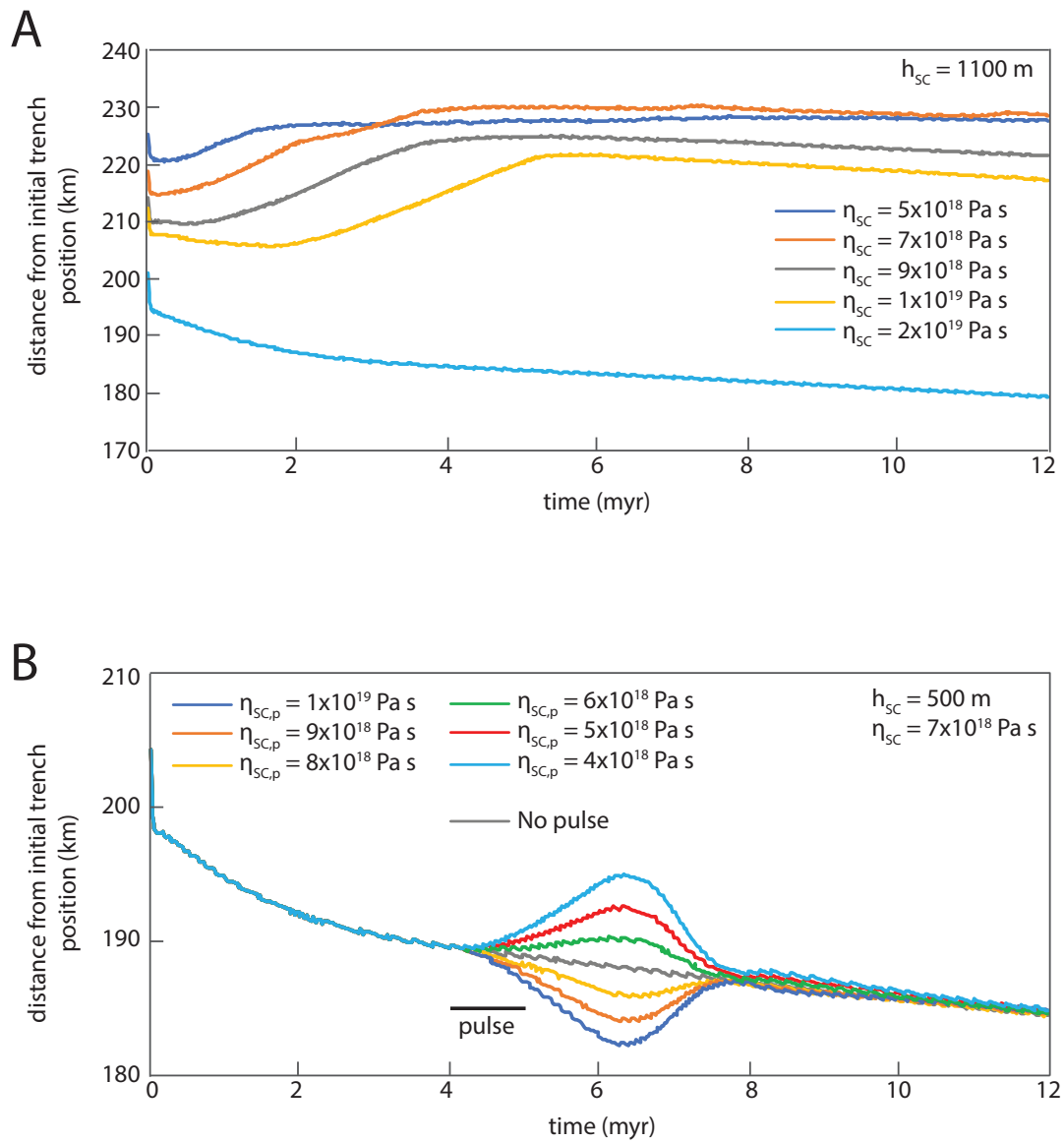
Figure 4-6. Migration of the coastline position for (a) a 1100-m-thick subduction channel, and (b) a 500-m-thick subduction channel with a viscosity of 7×10^{18} Pa s to which 1-myr-long pulses of different viscosities are applied. See Table 4-1 for simulation parameters.
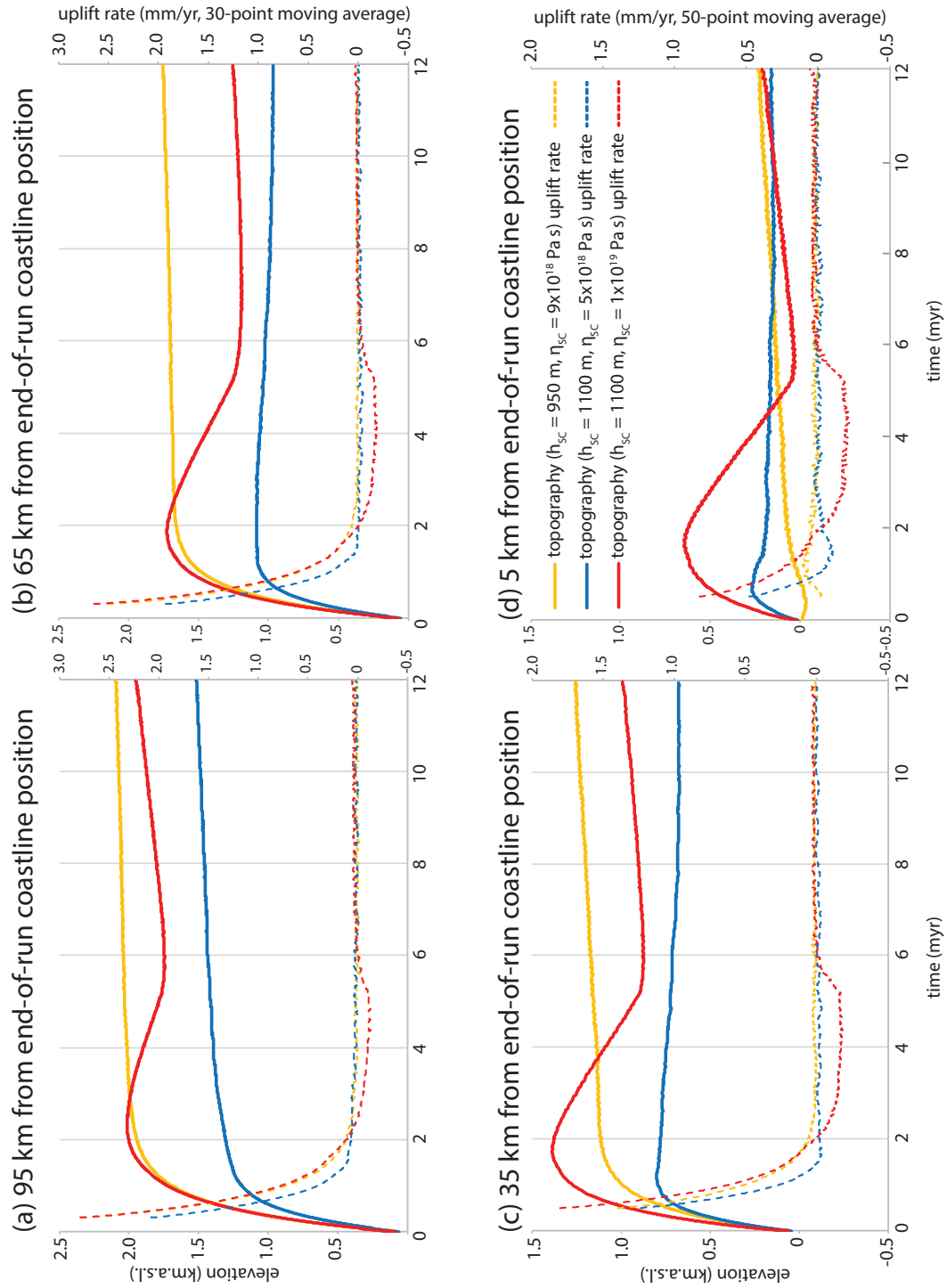
156

Figure 4-7. Evolution of surface elevation and uplift rate at (a) 95 km, (b) 65 km, (c) 35 km, and (d) 5 km from the final coastline position (see Fig. 4-3b), for three selected simulations varying the subduction channel thickness, h_{SC}, and subduction channel viscosity, η_{SC} (h_{SC} = 950 m and η_{SC} = 9x10^{18} Pa s; h_{SC} = 1100 m and η_{SC} = 5x10^{18} Pa s; h_{SC} = 1100 m and η_{SC} = 1x10^{19} Pa s). See Table 4-1 for simulation parameters.
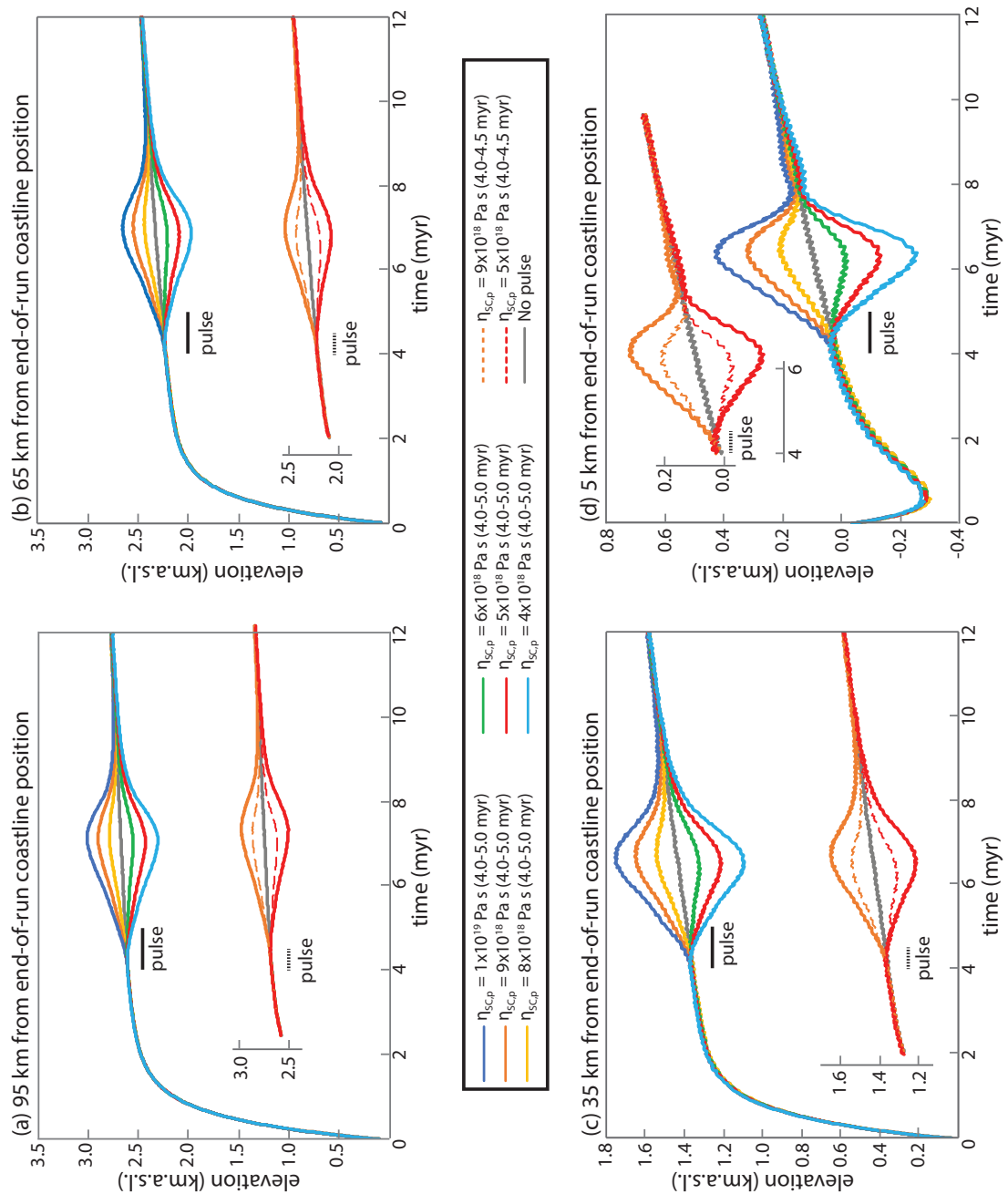
Figure 4-8. Evolution of surface elevation at (a) 95 km, (b) 65 km, (c) 35 km, and (d) 5 km from the final coastline position (see Fig. 4-3b), for simulations that include 1-myr and 0.5-myr pulses of differing viscosity that migrate downdip in the subduction channel with the velocity of subduction of the downgoing plate. Subduction channel thickness (h_{SC}) is 500 m, while subduction channel viscosity (η_{SC}) other than for the applied pulses is 7×10^{18} Pa s. See Table 4-1 for other simulation parameters.

REFERENCES

Arancibia, G., S. J. Matthews, and C. Pérez de Arce (2006), K-Ar and [40]Ar/[39]Ar geochronology of supergene processes in the Atacama Desert, northern Chile: tectonic and climatic relations. *Journal of the Geological Society* **163** (1), 107.

Bachmann, R., O. Oncken, J. Glodny, W. Seifert, V. Georgieva, and M. Sudo (2009), Exposed plate interface in the European Alps reveals fabric styles and gradients related to an ancient seismogenic coupling zone. *Journal of Geophysical Research* **114**, B05402, doi:10.1029/2008JB005927.

Bangs, N. L., T. H. Shipley, S. P. S. Gulick, G. F. Moore, S. Kuromoto, and Y. Nakamura (2004), Evolution of the Nankai Trough decollement from the trench into the seismogenic zone: Inferences from three-dimensional seismic reflection imaging. *Geology* **32**, 273–276.

Calahorrano, A. B., V. Sallares, J. Y. Collot, F. Sage, and C. R. Ranero (2008), Nonlinear variations of the physical properties along the southern Ecuador subduction channel: Results from depth-migrated seismic data. *Earth & Planetary Science Letters* **267 (3–4)**, 453–467.

Clift, P. D., and A. J. Hartley (2007a), Slow rates of subduction erosion and coastal underplating along the Andean margin of Chile and Peru. *Geology* **35**, 503-506.

Clift, P. D., and A. J. Hartley (2007b), Slow rates of subduction erosion and coastal underplating along the Andean margin of Chile and Peru: Reply to Comment. *Geology* **35**, 503-506.

Cosentino, N. J., T. E. Jordan, L. A. Derry, and J. P. Morgan (2015), ^{87}Sr/^{86}Sr in recent accumulations of calcium sulfate on landscapes of hyperarid settings: A bimodal altitudinal dependence for northern Chile (19.5°S–21.5°S). Geochem. Geophys. Geosyst. **16**, 4311-4328.

Cosentino, N. J., and T. E. Jordan (2017), ^{87}Sr/^{86}Sr of calcium sulfate in ancient soils of hyperarid settings as a paleoaltitude proxy: Pliocene to Quaternary constraints for northern Chile (19.5-21.7°S). Tectonics 35, doi:10.1002/2016TC004185.

Dabrowski, M., M. Krotkiewski, and D. W. Schmid (2008), MILAMIN: MATLAB-based finite element method solver for large problems. Geochemistry, Geophysics, Geosystems 9(4), Q04030.

David, C., D. Comte, J. Martinod, L. Dorbath, G. Hérail, C. Dorbath, and H. Haessler (2002), Intracontinental seismicity and Neogene deformation of the Andean forearc in the region of Arica, (18.5°S–19.5°S), paper presented at Fifth International Symposium on Andean Geodynamics, Dep. de Geofis., Univ. de Chile, Toulouse, France.

Dunai, T. J., G. A. González López and J. Juez-Larré (2005), Oligocene-Miocene age of aridity in the Atacama Desert revealed by exposure dating of erosion-sensitive landforms, Geology, 33(4), 321-324.

Encinas, A., and K. Finger (2007), Slow rates of subduction erosion and coastal underplating along the Andean margin of Chile and Peru: Comment. *Geology* **35**, doi: 10.1130/G24305C1.

Evenstar, L. A., F. M. Stuart, A. J. Hartley, and B. Tattich (2015), Slow Cenozoic uplift of the western Andean Cordillera indicated by cosmogenic ^{3}He in alluvial boulders from the Pacific Planation Surface. *Geophys. Res. Lett.* **42**, 8448-8455.

González, G., J. Cembrano, D. Carrizo, A. Macci, and H. Schneider (2003), The link between forearc tectonics and Pliocene-Quaternary deformation of the Coastal Cordillera, northern Chile. Journal of South American Earth Sciences 16, 321-342.

Hoke, G. D., B. L. Isacks, T. E. Jordan, N. Blanco, A. J. Tomlinson, and J. Ramezani (2007), Geomorphic evidence for post-10 Ma uplift of the western flank of the central Andes, 18º30' – 22ºS. Tectonics 26.

Isacks, B. L. (1988), Uplift of the central Andean plateau and bending of the Bolivian orocline. Journal of Geophysical *Research* **93**, 3211-3231.

Jordan, T. E., P. L. Nester, N. Blanco, G. D. Hoke, F. Dávila, and A. J. Tomlinson (2010), Uplift of the Altiplano-Puna plateau: A view from the west. *Tectonics* **29**, TC5007.

Jordan, T. E., N. E. Kirk-Lawlor, N. Blanco, J. A. Rech., and N. J. Cosentino (2014), Landscape modification in response to repeated onset of hyperarid paleoclimate states since 14 Ma, Atacama Desert, Chile. *Geological Society of America Bulletin* **126 (7-8)**, 1016-1046.

Lamb, S., and P. Davis (2003), Cenozoic climate change as a possible cause for the rise of the Andes. *Nature* **425**, 792-797.

Melnick, D. (2016), Rise of the central Andean coast by earthquakes straddling the Moho. *Nature Geoscience* **9**, 401-407.

Roy, M., and L. G. Royden (2000), Crustal rheology and faulting at strike-slip plate boundaries. 1. An Analytic model. Journal of Geophysical Research 105 (B3), 5583-5597.

Schweller, W. J., L. D. Kulm, and R. A. Prince (1981), Tectonics, structure, and sedimentary framework of the Peru-Chile Trench. *GSA Memoirs* **154**, 323-350.

Shewchuk, J. R. (1996), Triangle: engineering a 2D quality mesh generator and Delaunay triangulator. In Applied Computational Geometry: Towards Geometric Engineering (Ming C. Lin and Dinesh Manocha, editors), Lecture Notes in Computer Science 1148, 203-222, Springer-Verlag, Berlin (from the First ACM Workshop on Applied Computational Geometry).

Shreve, R. L., and M. Cloos (1986), Dynamics of sediment subduction, melange formation, and prism accretion. Journal of Geophysical Research 91 (B10), 10229-10245.

Sillitoe, R. H., and E. H. McKee (1996), Age of supergene oxidation and enrichment in the Chilean porphyry copper province, Economic Geology, 91, 164-179.

Tassara, A., H.-J. Götze, S. Schmidt, and R. Hackney (2006), Three-dimensional density model of the Nazca plate and the Andean continental margin. *J. Geophys. Res.* **111**, B09404, doi: 10.1029/2005JB003976.

van Dinther, Y., T. V. Gerya, L. A. Dalguer, P. M. Mai, G. Morra, and D. Giardini (2013), The seismic cycle at subduction thrusts: Insights from seismo-thermo-mechanical models. *J. Geophys. Res. Solid Earth* **118**, 6183–6202, doi:10.1002/2013JB010380.

Vannucchi, P., F. Remitti, and G. Bettelli (2008), Geological record of fluid flow and seismogenesis along an erosive subducting plate boundary. *Nature* **451**, 699–703.

Vannucchi, P., F. Sage, J. Phipps Morgan, F. Remitti, and J.-Y. Collot (2012), Toward a dynamic concept of the subduction channel at erosive convergent margins with implications for interplate material transfer. *Geochemistry Geophysics Geosystems* **13**, Q02003, doi:10.1029/2011GC003846.

von Huene, R., and C. R. Ranero (2003), Subduction erosion and basal friction along the sediment-starved convergent margin of Antofagasta, Chile. *Journal of Geophysical Research* **108**, 2079.

Wang, F., G. Michalski, J. Seo, D. E. Granger, N. Lifton, and M. Caffee (2015), Beryllium-10 concentrations in the hyper-arid soils in the Atacama Desert, Chile: Implications for arid soil formation rates and El Niño driven changes in Pliocene precipitation. *Geochimica et Cosmochimica Acta* **160**, 227-242.